Title: A Supercomplex Incorporating Both Electron Transport Chain and ATP Synthase

Authors: Yiqi Hu[1]†, Jonathan Wong[2,3]†, Erik Endres[4]†, Benz Corinna[2]†, Cristina Pecorilla[4]†, Kun Huang[5,6]†, Tomáš Bílý[2,3], Hongtao Tian[1], Menglu Teng[7], Fangzhu Han[1], Mengchen Wu[1], Naiwen Zhang[8,9], Qijun Chen[8,9], Jiancang Zhou[10], Dehua Lai[7], Alena Zíková[2,3], Martijn A. Huynen[11]*, Hassan Hashimi[2,3]*, Vivek Sharma[4,12]*, Ondřej Gahura[2]*, Alexey Amunts[5,6]*, Long Zhou[1]*

Affiliations:

[1]Department of Biophysics and Department of Critical Care Medicine of Sir Run Run Shaw Hospital, Zhejiang University School of Medicine, Hangzhou 310058, China
[2]Institute of Parasitology, Biology Centre, Czech Academy of Sciences, 37005 České Budějovice, Czech Republic
[3]Faculty of Science, University of South Bohemia, České Budějovice, Czech Republic
[4]Department of Physics, University of Helsinki, Helsinki 00014, Finland
[5]University of Münster, Schlossplatz 8, 48143, Münster, Germany
[6]Institute of Bio-Architecture and Bio-Interactions, Shenzhen Medical Academy of Research and Translation, Shenzhen, Guangdong 518107, China
[7]MOE Key Laboratory of Gene Function and Regulation, State Key Laboratory of Biocontrol and Guangdong Provincial Key Laboratory of Aquatic Economic Animals, School of Life Sciences, Sun Yat-Sen University, Guangzhou 510275, P. R. China
[8]Key Laboratory of Livestock Infectious Diseases, Ministry of Education, Key Laboratory of Zoonosis, College of Animal Science and Veterinary Medicine, Shenyang Agricultural University, Shenyang, China
[9]The Research Unit for Pathogenic Mechanisms of Zoonotic Parasites, Chinese Academy of Medical Sciences, Shenyang, China
[10]Department of Critical Care Medicine of Sir Run Run Shaw Hospital, Zhejiang University School of Medicine, Hangzhou, Zhejiang 310058, China
[11]Department of Medical BioSciences, Radboud University Medical Center, Nijmegen, The Netherlands
[12]HiLIFE Institute of Biotechnology, University of Helsinki, Helsinki 00014, Finland

*Corresponding author. Email: Martijn.Huijnen@radboudumc.nl, hassan@paru.cas.cz, vivek.sharma@helsinki.fi, gahura@paru.cas.cz, alexey.amunts@gmail.com, longzhou@zju.edu.cn
†These authors contributed equally to this work.

Abstract: The mitochondrial oxidative phosphorylation system powering most aerobic organisms is typically depicted as two spatially segregated machineries[1]: electron transport chain complexes I-IV (ETC CI-CIV) that generates proton motive force and adenosine triphosphate (ATP) synthase (complex V, CV) that consumes it[2,3]. Using the kinetoplastid parasite *Trypanosoma brucei* in its procyclic form, we characterize a *bona fide* ETC-ATP synthase supercomplex that directly incorporates CII, CIV dimer and ATP synthase ($CIICIV_2CV$) alongside conventional assemblies. Cryo-EM structure shows a clear organizing principle in which ATP synthase engages CIV_2 via a non-canonical hetero-dimerization module of two subunit *g* paralogs, *g'* and *g''*, replacing the canonical *g*/*g* dimerization interface required for ATP synthase dimerization[4]. The resulting ~2 MDa assembly forms an arc-shaped membrane region, which stabilizes shallow positive membrane curvature as indicated by atomistic simulations. Genetic disruption of *g'*/*g''* selectively destabilizes the supercomplex and triggers pronounced cristae remodeling from discoidal to elongated tubular form, accompanied by a reduced maximal polarization capacity and comparatively modest effects on steady-state ATP output. These findings establish a structurally defined ETC-ATP synthase supercomplex and suggest its primary role in architectural quality control, constraining ATP synthase supramolecular organization to safeguard mitochondrial integrity rather than simply enhancing chemiosmotic coupling.

Main: The oxidative phosphorylation (OXPHOS) system, localized to the mitochondrial cristae, powers most aerobic eukaryotes by coupling electron transport-driven proton motive force (PMF) generation and PMF-driven ATP synthesis. It consists of four ETC complexes CI-CIV[5] and a terminal F_1F_o ATP synthase, or CV[6]. ETC complexes assemble into respiratory/ETC supercomplexes in different stoichiometries and architectures[7–20]. Previous cryo-electron microscopic (cryo-EM) studies showed that the most complete assemblies can contain the entire ETC, such as the $(CICIII_2CII)_2CIV_2$ in ciliates[21,22] and the $CII_2CIII_2CIV_2$ in parasitic organisms lacking CI[23]. Recent advances in *in situ* structural biology further

revealed that the native organization might be even more complex and heterogeneous[24,25]. Despite all these efforts, the functional relevance of these supercomplexes remain extensively debated[7,26]. Apart from ETC, ATP synthases also join together to form higher order assemblies, for instance by dimerizing with different inter-protomer angles, thereby contributing to diverse cristae morphologies[4,27–40]. Canonical ATP synthase dimers mainly rely on subunits *e* and *g* to organise adjacent monomers across eukaryotic clades, which could be traced back to the last eukaryotic common ancestor[4]. Therefore, subunit *g* remains a central component for canonical ATP synthase dimerization and multimerization.

Bioenergetic coupling ultimately requires tight coordination between proton sources (ETC) and proton sinks (ATP synthase) inside cristae, raising a basic but unresolved question that whether the ETC complexes can form a stable, architecturally defined assembly with the ATP synthase. In the original chemiosmotic theory of Peter Mitchell, oxidative phosphorylation functions via the mechanism of vectorial coupling, in which electron transfer and ATP synthesis are linked through directional translocation of protons across a coupling membrane[2]. Such membrane-based coupling, analogized to a ‘proton circuit’, is further quantified by breaking down the PMF into the electrical and the osmotic components[3]. A central implication of this framework is that the bioenergetic function is inseparable from supramolecular organization[18,19]: the coupling membrane is not merely an insulated support, but also an active element that constrains where proton sources and sinks can be positioned, and how efficiently their fluxes can be coordinated.

Specifically speaking, ETC supercomplexes and ATP synthase multimers are usually viewed as spatially segregated entities within the inner mitochondrial membrane (IMM). For opisthokonts and archaeplastidans, CV_2 rows are confined to the cristae ridges, while ETC supercomplexes populate the flat regions of the IMM and exist as large but discrete, fluid macromolecules[1,24,25]. Since ATP synthase is a rotary machine embedded in a highly curved membrane environment, its direct association with the ETC components must be

compatible with its rotational motion and the membrane shaping constraints. Preliminary studies have described the proximity between respirasomes and ATP synthase rows[41,42], and biochemical evidence has suggested ETC-ATP synthase association in several lineages, including mammals and plants[43–45], but a structurally resolved supercomplex and its organizing principle have remained elusive.

Here we address this gap by using a kinetoplastid parasite *Trypanosoma brucei*, a member of the eukaryotic supergroup of Discoba[46]. As the causative agent of human African trypanosomiasis, it transitions from a glycolysis-dependent bloodstream form to a procyclic form featuring a fully developed, respiratory-active mitochondrion during its life cycle[47,48]. We characterise a supercomplex that physically links CII and a CIV dimer to ATP synthase, namely $CIICIV_2CV$. The assembly is enabled by a non-canonical, heterodimeric *g'/g''* module that repurposes the canonical ATP synthase dimerization interface. Genetic perturbation reveals that the primary consequence of disrupting this linkage is the remodeling of *T. brucei*'s discoidal cristae, which further induces a drop in the maximal efficiency of chemiosmotic coupling. Together, these findings establish a direct ETC-CV supercomplex and suggest that such OXPHOS organization is tuned to safeguard mitochondria both morphologically and functionally.

Structure determination and overall architecture of T. brucei $CIICIV_2CV$ and $CIII_2CIV_2$

To isolate the ETC-CV supercomplex from CV oligomers, ETC complexes and supercomplexes, digitonin-solubilized mitochondrial membranes from procyclic *T. brucei* TREU927 were purified sequentially by sucrose gradient ultracentrifugation and anion exchange chromatography (Supplementary Fig. 1). Cryo-EM datasets were collected for fractions corresponding to isolated complexes of $CIII_2$ and CIV_2, $CIII_2CIV_2$ supercomplex and the highest molecular weight (MW) $CIICIV_2CV$ supercomplex, respectively (Supplementary Tables 1-4). For the $CIICIV_2CV$ dataset, particles were classified into three rotational states of ATP synthase, and the most populated state is state 3, following the

nomenclature established for *T. brucei* CV_2[4] (Extended Data Fig. 1a). Within each state, local refinements of CII, CIV_2 and distinct regions of CV yielded maps at 2.9 Å to 3.9 Å resolution. These local refined densities were merged into a composite $CIICIV_2CV$ map (Extended Data Fig. 2a-c). To facilitate model building, we generated a consensus reconstruction of the shared, membrane embedded portion of the supercomplex $CIICIV_2CV$ ($CIICIV_2CV_{mem}$), refined across all rotational states to 2.8 Å (Extended Data Fig. 2d). For the $CIII_2CIV_2$ dataset, $CIII_2$ and CIV_2 regions were locally refined to 3.14 Å and 3.23 Å, respectively, and combined into a composite $CIII_2CIV_2$ map (Extended Data Figs. 1b,c and 2e-g).

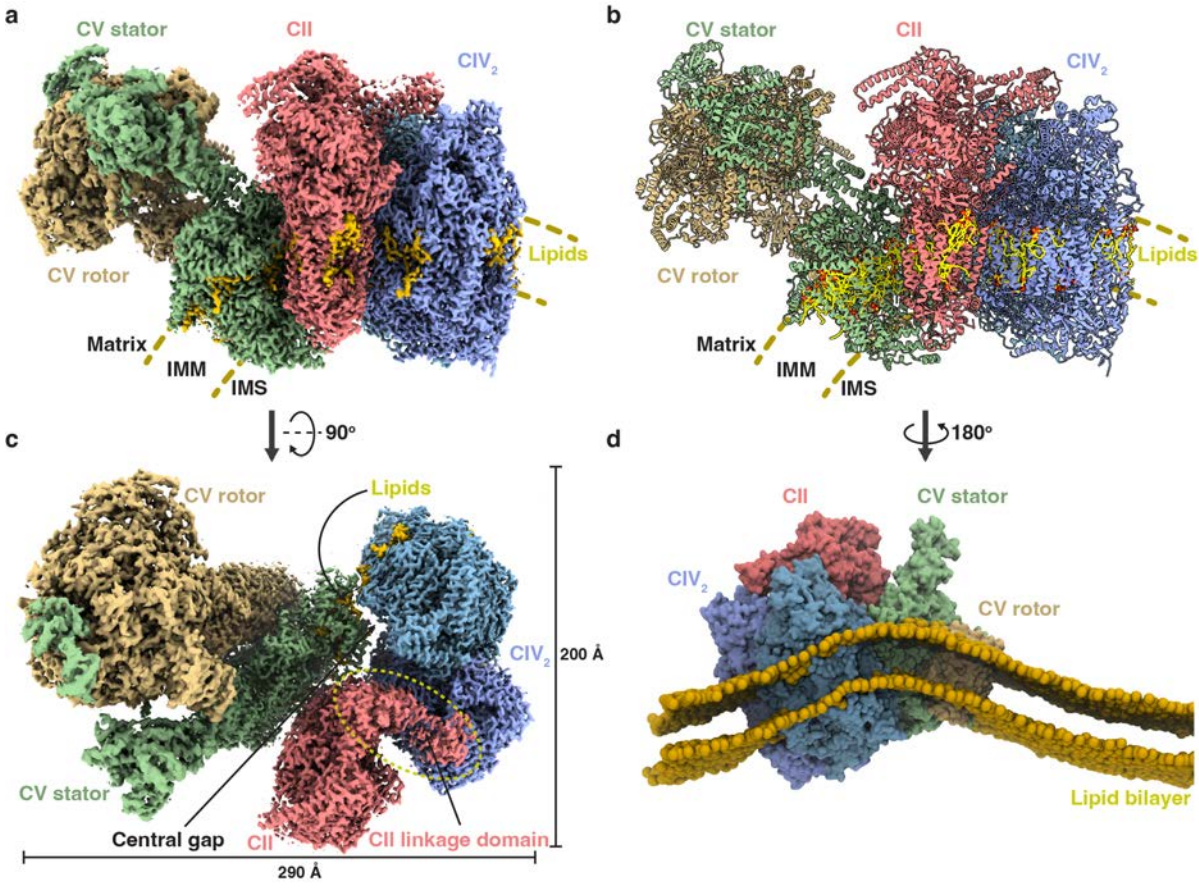

Fig. 1 | Overall architecture and mitochondrial membrane bending of the $CIICIV_2CV$ supercomplex. a,b, Cryo-EM density map (**a**) and model (**b**) of $CIICIV_2CV$ viewed parallel to the IMM plane. Constituent complexes and associated lipids are colored as labeled. **c,** View from the matrix side showing the counterclockwise arrangement of CII, CIV_2 and CV. The central gap is labeled and the lineage-specific CII linkage domain is highlighted by a dashed circle. **d,** Atomistic MD simulation snapshot of the membrane-embedded region of $CIICIV_2CV$ in lipid bilayer showing induction of a shallow positive membrane curvature (phosphorus atoms shown as yellow spheres).

CII, CIV_2 and CV are arranged in counterclockwise order when the ~2 MDa $CIICIV_2CV$ supercomplex is viewed from the matrix side perpendicular to the IMM (Fig. 1a-c and Supplementary Video 1). A visible gap at the center separates the three complexes and is likely occupied by lipids *in vivo* as densities for several cardiolipin molecules are resolved in this region. When viewed parallel to the IMM with CII in front, the membrane embedded regions of CV, CII and CIV_2 trace a continuous arc with an overall curvature of ~36° (Fig. 1a,b and Extended Data Fig. 3d). This bending is less pronounced than that is caused by the canonical ATP synthase dimer, which spans a comparable membrane footprint but enforces a ~48° curvature (Extended Data Fig. 3d). Therefore, whereas CV_2 decorates the highly curved rim of discoidal cristae, $CIICIV_2CV$ is expected to occupy a less curved zone between the peripheral region and the flatter central part of the membrane. In contrast, the ~1.4 MDa $CIII_2CIV_2$ supercomplex is essentially flat in terms of its inter complex angle, suggesting localization in an even more central, low curvature region than $CIICIV_2CV$ (Extended Data Fig. 4 and Supplementary Video 1, see also Extended Data Fig. 5).

To directly assess the contribution of $CIICIV_2CV$ supercomplex to membrane bending, we performed atomistic molecular dynamics (MD) simulations of the protein-lipid complex. The $CIICIV_2CV$ supercomplex maintained the membrane curvature throughout the simulations (Fig. 1d and Supplementary Video 2), while a corresponding $CIICIV_2$ lacking CV relaxed rapidly towards a flatter membrane conformation (Supplementary Video 3). A similar relaxation towards a flat bilayer was observed for a protein free lipid membrane (Supplementary Video 4), suggesting that stable curvature is specifically sustained by the assembly of $CIICIV_2$ with CV, i.e., the $CIICIV_2CV$ supercomplex.

A non-canonical ATP synthase dimerization module orchestrates $CIICIV_2CV$ assembly

The dimeric CIV_2 approaches CV from the stator side near subunit *a* where the canonical $(e/g)_2$ dimerization module is positioned in CV_2[4] (Fig. 2a). Importantly, when $CIICIV_2CV$

and CV_2 are superposed via a common CV protomer, the second CV protomer in CV_2 overlaps with the CIV protomer that is proximal to CV in $CIICIV_2CV$ (hereafter CIV_P) (Extended Data Fig. 3d). Instead of the expected homodimer of the canonical subunit *g*, a heterodimer formed by two non-canonical *g*-like subunits *g'* and *g''* (Supplementary Table 3) is found at the CIV_P-CV interface (Fig. 2b). These two subunits interlock via IMM-parallel helices H2 and H3, which are homologous to the helices forming the canonical *g*-*g* interface in CV_2[4]. Subunit *g''* lacks the N-terminal helix H1 present in *g* and *g'*, avoiding a steric clash with COX5B from the distal CIV protomer (CIV_D) (Fig. 2b). To avoid ambiguity, the three conserved helices shared among *g*/*g'*/*g''* are uniformly referred to as H2-H4$^{g/g'/g''}$ (Extended Data Fig. 3a,b). The N-termini of the two subunit *e* helices insert into 'sockets' formed by H3$^{g'/g''}$ and H4$^{g'/g''}$ (Fig. 2a,b). Interestingly, the subunit *e* within the *e*/*g'* module projects perpendicularly into the IMM near the center of this three-complex assembly (Fig. 2c). Together, these observations indicate that CIV-CV association is mediated by a signature *e*/*g'*/*e*/*g''* heterotetrameric module, suggesting that the emergence of *g'* and *g''* in Euglenozoa likely preceded or coincided with the evolution of an ETC-CV supercomplex.

The *T. brucei* CII structure further reveals that the core subunits SDHB and SDHD are each split into two polypeptides (SDHB/D1 and 2) (Extended Data Fig. 6d,e), consistent with prior biochemical observations, although SDHC and SDHD1 were previously misassigned[49]. CII wedges into the gap formed between CIV_D and the exterior of the CV's F_o stator (Fig. 1c). The *e*/*g'*/*e*/*g''* module also contributes to CII-CV association, as subunit *g'* extends across the central gap to contact the CII's accessory subunit SDHTB7, emphasizing the organizational role of this module in both CIV_2-CV and CII-CV assembly (Fig. 2c). Beyond this contact, interfaces between CII and CV are limited and are largely bridged by lipid molecules (Extended Data Fig. 3f). Interfacial lipids have been repeatedly observed in bioenergetic assemblies[21,22,25,50], including mammalian respiratory supercomplexes[19], emphasizing the importance of lipids, especially cardiolipin, in stabilizing higher order supercomplexes[51].

In contrast to the lipid-rich CII-CV interface, CII-CIV_2 association is mediated by a bracket-shaped CII linkage domain that contacts CIV_D from the matrix side (Fig. 1c). This lineage-specific feature comprises newly identified CII accessory subunits SDHTB5 and SDHTB6 (Fig. 2d). The splitting of SDHB contributes to this interaction: N- and C-terminal extensions respectively arising from the SDHB1-SDHB2 division point serve as attachment sites for SDHTB5 and SDHTB6. The C-terminal extension of SDHB1 even traverses SDHTB5 and directly participates in linkage domain's contacts with the CIV_D subunit COXEG7 (Fig. 2d and Extended Data Fig. 6d).

The linkage domain is further supported by SDHTB7, the *g'/g''* contacting subunit which forms a largely horizontal helix bundle stabilized by transmembrane helices near the two SDHD subunits (Fig. 2d and Extended Data Fig. 6g). SDHTB7 thereby provides a second anchor for the linkage domain in addition to its association with the CII's hydrophilic core. An orthologue identified based on structural similarity, SDHTB7, exists in *Tetrahymena thermophila* (SDHTT3), where it serves as an attachment site for the additional hydrophilic subunit SDHTT1 that contacts the enlarged CIV_2 in the $CIV_2(CICIII_2CII)_2$ supercomplex[21,22] (Fig. 2e and Extended Data Fig. 6f). These observations suggest that SDHTB7/SDHTT3 specifically provides a platform for different lineage-specific expansions of the CII hydrophilic domain, enabling versatile CII-CV interactions and incorporation of CII into ETC supercomplexes (Fig. 2d,e and Extended Data Fig. 6g). CII-containing supercomplexes are present in Alveolata[21–23] and Discoba (Fig. 1), but appear to be absent from opisthokonts[9,20,24], consistent with the subunit SDHTB7/SDHTT3 being a synapomorphy within Diphoda following divergence from Opimoda[52]. Moreover, SDHTB7/SDHTT3 orthologues are enriched in Diphoda[21–23] but excluded from Opimoda (Extended Data Fig. 6h). Notably, since CII-containing supercomplex has not been reported in free-living euglenids such as *Euglena gracilis*[53], a potential secondary loss of SDHTB7 or its ortholog will require further investigation.

In summary, assembly of the CIICIV$_2$CV supercomplex is enabled by lineage-specific innovations, including ATP synthase subunits *g'/g''*, paralogues of the canonical dimerization subunit *g*, and the CII linkage domain components SDHTB5-7. While the latter mediate CII docking onto CIV$_2$ in a manner reminiscent of the *T. thermophila* CIV$_2$(CICIII$_2$CII)$_2$ architecture, *g/g'/g''* provide an additional layer of control that partitions assembly towards ATP synthase oligomers versus an ETC-CV supercomplex.

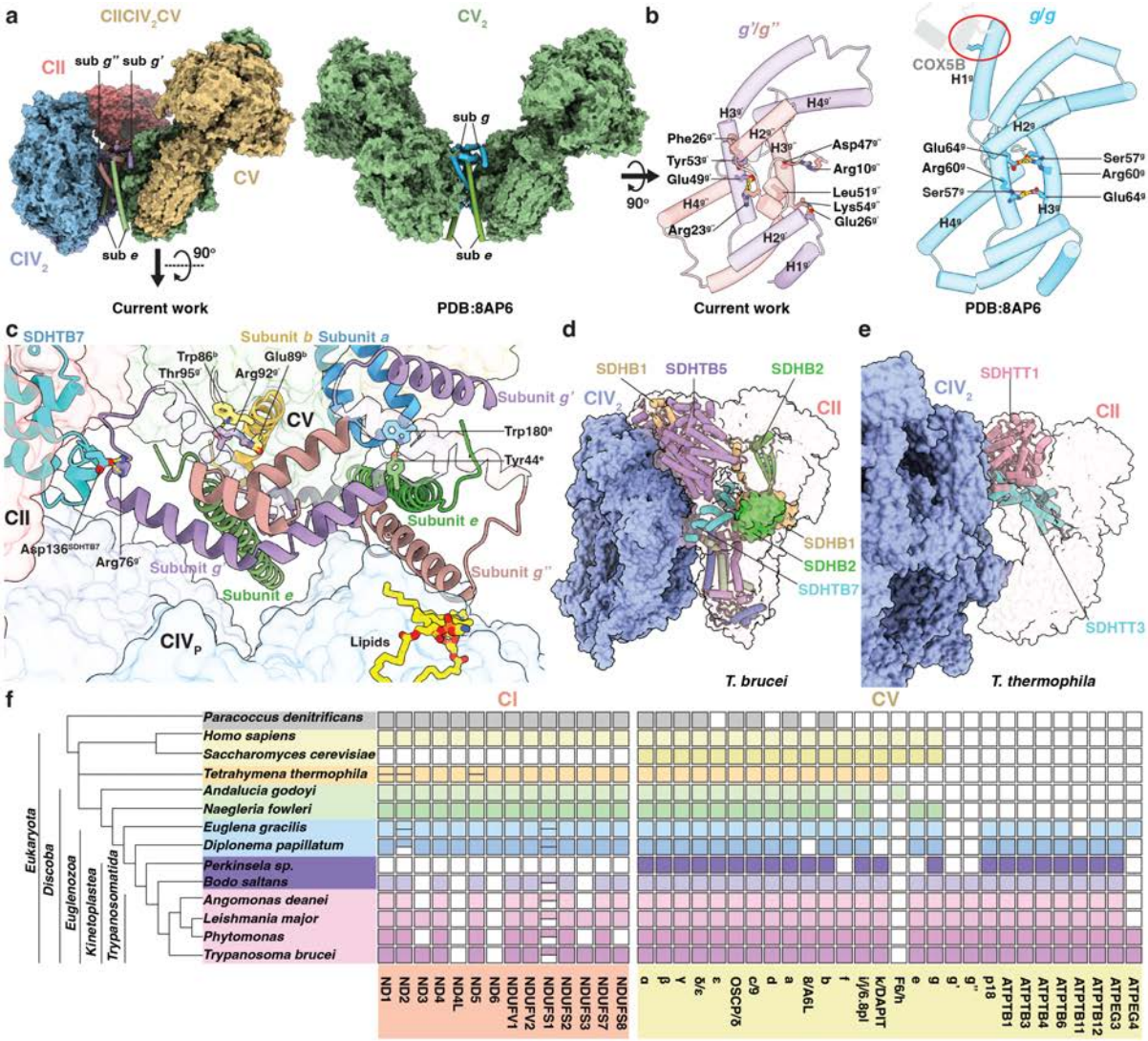

Fig. 2 | The kinetoplastid-specific *g'/g''* module and the CII linkage domain orchestrate CIICIV$_2$CV assembly. a, Side view of the CIICIV$_2$CV and CV$_2$ (PDB: 8AP6) shown as surfaces, with respective non-canonical *e/g'/e/g''* and canonical (*e/g*)$_2$ modules shown as cartoons. **b,** Matrix view of the interlocking *g'* (lavender) and *g''* (salmon) subunits (left) and the canonical *g/g* (blue) module (right), with helix numbering indicated. A potential steric clash between H1^g and COX5B (grey) is marked (red circle) if the canonical *g/g* module is

placed into CIICIV$_2$CV interface. **c,** Close-up of the *e*/*g'*/*e*/*g''* module bridging CV with CII and the proximal CIV$_P$. **d,e,** Interfaces between CII (transparent) and CIV$_2$ (solid) in *T. brucei* (**d**) and *T. thermophila* (**e**), highlighting the SDHTB7/SDHTT3 orthologue supporting additional hydrophilic elements that contact CIV$_2$. In *T. brucei*, lineage-specific extensions of SDHB1 (yellow) and SDHB2 (green) help to stabilize SDHTB5 (cartoons). For panels **b-e**, key residues/lipids and interactions are shown as sticks and dashed lines, respectively. **f**, Phylogenetic distribution of selected CI and CV subunits across representative taxa, with filled squares indicating presence of an orthologue, whereas empty squares indicating absence.

The appearance of CIICIV$_2$CV coincides evolutionarily with loss of Complex I

To pinpoint when ETC-CV supercomplexes, such as CIICIV$_2$CV emerged during evolution, we performed sequence- and structure-based homology searches for subunits of CII, CIV, CV and the core subunits of CI across a panel of model species with an emphasis on Discoba (Fig. 2f, Extended Data Figs. 3g, 4g, 6h and Supplementary Table 5). These analyses demonstrate that within Kinetoplastea, *Perkinsela sp.* occupying a phylogenetic position most distant from trypanosomatids, already encodes two *g*-like subunits, and the free-living *Bodo saltans* is the first kinetoplastid in our sampling to encode three *g*-like subunits (Fig. 2f and Extended Data Fig. 3g). Therefore, the initial split of subunit *g* likely occurred in the common ancestor of Kinetoplastea, as only the canonical *g* subunit can be found in other major euglenozoan classes such as Euglenida and Diplonemea.

In parallel, the 14 core CI subunits are conserved in Euglenida [53] and Diplonemea[54,55], whereas in Kinetoplastea two core CI subunits, ND4L and ND6, could not be detected in the mitochondrial genome[56] (Fig. 2f). This pattern suggests that a canonical transmembrane CI, and therefore a respirasome, is likely restricted to Euglenida and Diplonemea. Among kinetoplastids, non-trypanosomatid species such as *Perkinsela sp.* and *B. saltans* show no clear evidence of CI, although the *B. saltans* genome remains incomplete[57,58]. Within trypanosomatids, the mitochondrial transcripts CR3 and CR4 have been suggested as homologues of ND4L and ND6[59], however, we detect neither structural nor sequence similarity between CR3/CR4 and ND4L/ND6 from mammals or other discobans

(Supplementary Fig. 2g-i). Electrophoretic analyses have nevertheless reported NADH dehydrogenase activity in the mitochondrial complexes from several trypanosomatids, including a *Phytomonas serpens* complex containing hydrophilic CI subunits NDUFA6 and NDUFA9[60–63]. However, this does not necessitate the presence of CI's membrane arm. Consistently, we did not identify full CI-like particles in 2D classes from cryo-EM data collected on crude *T. brucei* mitochondrial factions exhibiting NADH dehydrogenase activity (Supplementary Fig. 2a-f). Given the fundamental roles of ND4L and ND6 in coupling electron transfer to proton pumping[64], these observations support the conclusion that, at least in the procyclic stage, trypanosomatids likely lack a PMF-generating CI.

The coincidence of ND4L and ND6 loss with subunit *g* duplication in *Perkinsela sp.* indicates that the appearance of ETC-CV supercomplex may have accompanied, and potentially compensated for the loss of transmembrane CI at the root of kinetoplastid evolution. Exceptions do exist, for example *Perkinsela sp.* have only two *g*-like subunits rather than three found in most kinetoplastids, yet already lacks CI, and whether it assembles an alternative *g*/*g'*-based CIICIV$_2$CV organization remains unknown. Conversely, *P. serpens* has three *g*-like subunits but has lost CIII$_2$ and CIV[65], making formation of CIICIV$_2$CV supercomplex unlikely. In this lineage, *g*-like subunits may represent evolutionary remnants. For most other kinetoplastids, the specific loss of the CI membrane arm is consistent with CIICIV$_2$CV contributing to the compensation for diminished mitochondrial membrane potential maintenance or cristae shaping functions normally associated with CI and respirasome.

Knockout of subunit g' or g'' destabilizes and disassembles the CIICIV$_2$CV supercomplex

To investigate the physiological role of the ETC-CV supercomplex in mitochondrial metabolism, we generated single homozygous knockout (KO) strains of subunits *g'*, *g''* and the CIV subunit NDUFA4, as well as tetracycline-inducible conditional KO strains of kinetoplastid-specific CIV subunits COXTB2 and COXTB3 (hereafter *g'*$^{-/-}$, *g''*$^{-/-}$, NDUFA4$^{-/-}$

297 and COXTB2/3$^{-/-/tet}$, respectively, Extended Data Fig. 7a). In addition to the non-canonical *g*-
298 like subunits, NDUFA4, COXTB2 and COXTB3 contributed to formation of the CIV$_P$-CV
299 interface. All KO strains showed near-complete loss of the targeted gene products while
300 maintaining normal expression of representative subunits from each OXPHOS complex
301 (Extended Data Fig. 7b,c). Western blot analysis of digitonin-extracted mitochondrial lysates
302 resolved by BN-PAGE demonstrated that constitutive NDUFA4$^{-/-}$ and conditional
303 COXTB2/3$^{-/-/tet}$ four days post induction (COXTB2/3$^{-/-/tet}$ day 4) result in near-complete loss
304 of CIV-containing bands (Fig. 3a). By contrast, *g'*$^{-/-}$ and more strongly *g''*$^{-/-}$ specifically
305 reduced the CIICIV$_2$CV band while retaining 60%-80% of the wild type (WT) levels of
306 lower-MW CIV$_2$-containing bands. Surprisingly, strong decreases in monomeric ATP
307 synthase levels are also observed for the *g'*$^{-/-}$ and *g''*$^{-/-}$ strains, consistent with a shift of CV
308 into dimers and potentially higher order assemblies (Fig. 3a).
309
310 To further probe the destabilization of CIICIV$_2$CV upon removal of subunit *g'* or *g''*, we
311 performed atomistic MD simulations in which *g'* and *g''* were knocked out *in silico* (see
312 Methods). In both simulations, the CIV$_P$-CV interface was perturbed, as quantified by
313 changes in the buried solvent accessible surface area (SASA) between the two complexes
314 (Fig. 3b). Subunit *g'* KO simulation showed a larger spread of buried SASA values,
315 indicating an interface that frequently samples tighter and looser states. In contrast, subunit
316 *g''* KO displayed a reduced median buried SASA, consistent with a persistently weakened
317 CIV$_P$-CV association, in agreement with the BN-PAGE characterization (Fig. 3a,b).
318 Inspection of the trajectories revealed additional local rearrangements (Extended Data Fig. 8
319 and Supplementary Videos 5-7). In the subunit *g''* KO simulation, helices H1$^{g'}$ and H3$^{g'}$
320 became distorted, with bending angles increasing from 10°±2 and 29°±1 in WT to 34°±19
321 and 45°±2, respectively (Extended Data Fig. 8a-f and Supplementary Videos 5 and 7).
322 Conversely, in the subunit *g'* KO simulation, H3$^{g''}$ adopted a straighter conformation, with its
323 internal helical angle changing from 22°±1 in WT to 17°±1 (Extended Data Fig. 8a-c, g-i and
324 Supplementary Videos 5 and 6). Together, the BN-PAGE and MD results demonstrate that

the loss of subunit *g''* or *g'* destabilizes the CIICIV$_2$CV supercomplex or prevent its assembly, and is accompanied by enhanced formation of dimeric ATP synthase.

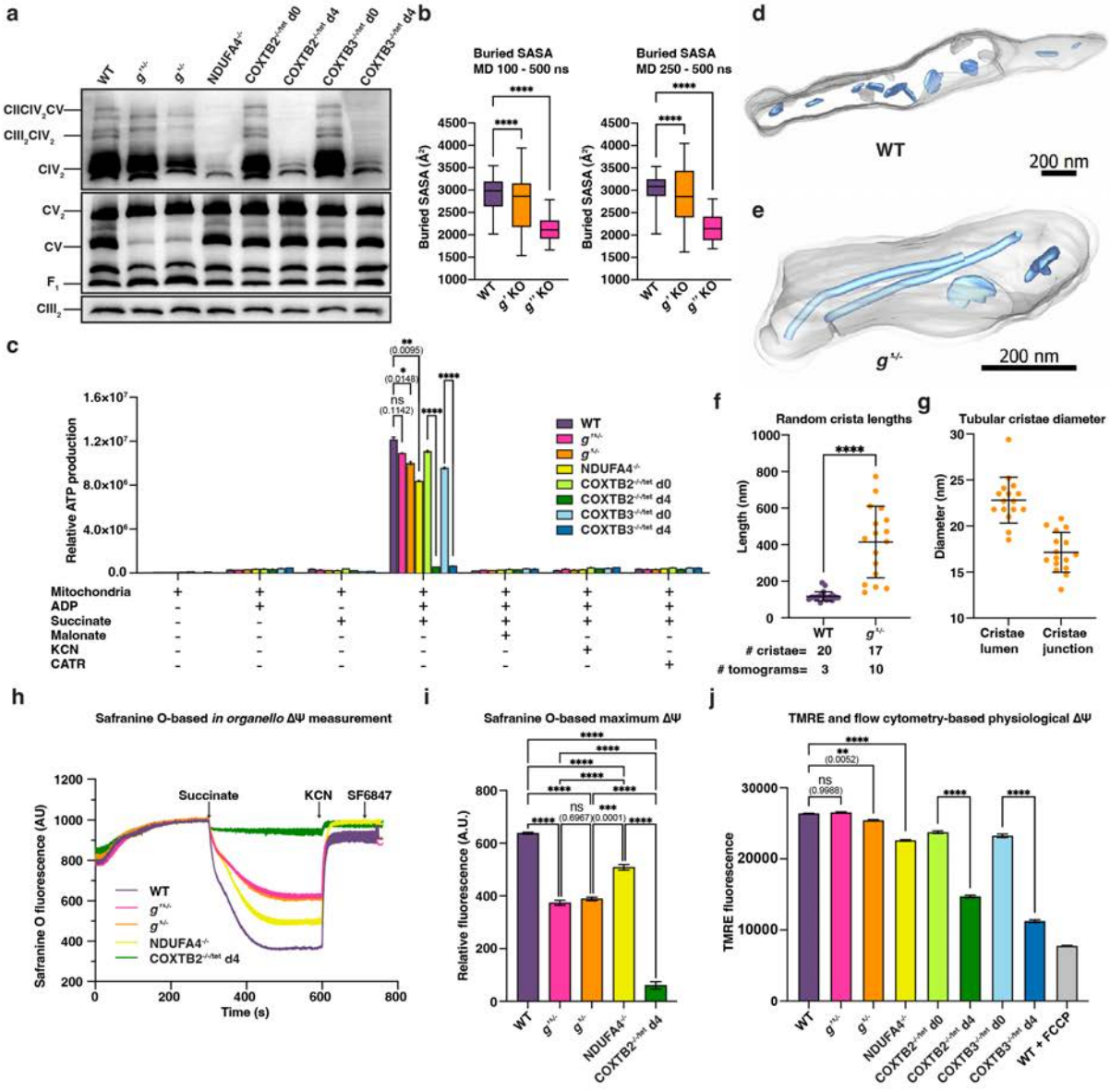

Fig. 3 | Bioenergetic and morphological consequences of disrupting CIICIV$_2$CV assembly. a, Immunoblotting of digitonin-extracted mitochondrial lysates from WT and KO strains, resolved by BN-PAGE. Antibodies detect COXEG7 (CIV), subunit β (CV) and UQCRFS1 (CIII$_2$). CIII$_2$, which is not part of CIICIV$_2$CV or CV$_2$, is used as a loading control. **b,** Box plots of buried SASA at the CIV$_P$-CV interface during the last 400 ns (left) or 250 ns (right) of 500 ns MD simulations of WT and *in silico g'/g''* KO supercomplexes. **c,** ATP production in permeabilized WT and KO cells in the presence or absence of the indicated substrates and inhibitors. **d,e,** Representative electron tomographs of WT (**d**) and *g'*$^{-/-}$ (**e**) mitochondria; segmented cristae in blue. **f,** Length measurements of all visible cristae from WT and *g'*$^{-/-}$ tomographs. **g,** Diameter measurements of tubular cristae lumen and

junction from *g'*$^{-/-}$ tomographs. **h,i,** Safranine O-based *in organello* measurements of membrane polarization capacity: representative traces (**h**) and maximal $\Delta\Psi_m$ values (**i**) after energization with succinate and subsequent addition of KCN and the uncoupler SF6847. **j,** TMRE and flow cytometry-based measurements of physiological $\Delta\Psi_m$ in living cells. FCCP-treated WT cells serve as a depolarized control. Numerical data are represented as mean ± SEM (n = 3 biologically independent replicates).

CIICIV$_2$CV impacts cristae morphology more than bioenergetic output in kinetoplastids

Since the physiological significance of CIICIV$_2$CV is best assessed through the consequences of its loss, we measured mitochondrial membrane potential ($\Delta\Psi_m$), ATP production rates, and growth of WT and KO strains. *In organello*, cyanide-sensitive $\Delta\Psi_m$ driven by saturating succinate decreased ~40% in *g'*$^{-/-}$ and *g''*$^{-/-}$ and was nearly abolished in COXTB2 $^{-/-/tet}$ four days post induction, consistent with near-complete loss of CIV expression in this strain (Fig. 3a,h,i). By contrast, flow cytometry-based measurement in living cells did not detect a meaningful difference in physiological $\Delta\Psi_m$ between WT and *g'*/*g''* KOs (Fig. 3j). Together, these results suggest that loss of CIICIV$_2$CV reduces the maximal polarization capacity, but not the physiological ability of OXPHOS to maintain $\Delta\Psi_m$ under steady-state conditions. Consistent with this interpretation, succinate-driven ATP synthesis, powered by CII-CIV electron transfer, decreased by only 10-20% for *g'*$^{-/-}$ and *g''*$^{-/-}$, in line with their mild growth defects under both respiratory and glycolytic conditions (Fig. 3c and Extended Data Fig. 7e-g). Thus, despite a reduced upper limit of PMF generation, disassembly of CIICIV$_2$CV does not markedly compromise apparent chemiosmotic coupling under the conditions tested.

To investigate whether the reduced polarization capacity is linked to structural remodeling, we assess mitochondrial ultrastructures in WT, *g'*$^{-/-}$ and *g''*$^{-/-}$ by transmission electron microscopy (TEM) of resin embedded thin sections. Elongated, tubular cristae were observed in *g''*$^{-/-}$ and, more prominently in *g'*$^{-/-}$, in contrast to the canonical discoidal cristae typical of kinetoplastids (Extended Data Fig. 9). To visualize and quantify these changes, we reconstructed tilt series-based electron tomograms from defined numbers of WT and *g'*$^{-/-}$ mitochondrial thin sections (Supplementary Videos 8 and 9). Tomography confirmed, both morphologically and statistically, that a substantial fraction of *g'*$^{-/-}$ cristae become elongated

and adopt a tubular morphology with a median lumen diameter of ~23 nm, whereas WT cristae remain discoidal (Fig. 3d-g and Extended Data Fig. 9). Accordingly, the distribution of cristae lengths in *g'*$^{-/-}$ shows a larger spread and higher median than in WT (Fig. 3f and Extended Data Fig. 9c).

CIICIV$_2$CV may preserve discoidal cristae by limiting CV$_2$ row extension

Tubular cristae are typically observed in ciliates, where long, helical rows of ATP synthase dimers coil around the cristae tube and impose a uniform cylindrical curvature[29,30]. In kinetoplastids, we propose that CIICIV$_2$CV contributes to maintaining short CV$_2$ rows by preventing further row extension (Fig. 4, see also the accompanying manuscript). In this model, the F$_1$ head of CV within CIICIV$_2$CV can dock into the inter-F$_1$ space of a CV$_2$, analogous to the interaction between adjacent CV$_2$ units within multimeric row[31] (Fig. 4a). Structurally, the membrane portion of *e*/*g'*/*e*/*g''*-linked CIV$_P$-CV is not bulkier than an F$_o$ dimer and is geometrically compatible with CV$_2$ association. This is also consistent with the shallower curvature of CIICIV$_2$CV relative to CV$_2$ and its likely more central localization compared to CV$_2$ rows at the rim of discoidal cristae (Extended Data Fig. 3d). However, unlike CV$_2$, CIICIV$_2$CV is intrinsically asymmetric, and the opposite CII-CIV$_D$ end does not provide a compatible interface for continued addition of CV$_2$ unit (Fig. 4b). Thus, CIICIV$_2$CV could act as a cap that constrains CV$_2$ assemblies and without it, uncontrolled elongation of CV$_2$ spirals drive the transition from discoidal to tubular cristae (Fig. 4c). This model is line with the sharp decrease in CV monomer in *g'*$^{-/-}$, indicating redistribution of CV into dimer rows (Fig. 3a). A related constraining effect of ETC components on ATP synthase rows has been implicated in *E. gracilis*, where negative curvature in the respirasome membrane domain positions it adjacent to the CV$_2$-decorated cristae rim, potentially imposing a steric limit on uncontrolled CV$_2$ elongation[31,53]. By analogy, emergence of CIICIV$_2$CV in Kinetoplastea may partially compensate for the evolutionary loss of CI by providing a structural mechanism to keep CV$_2$ oligomers finite and the cristae discoidal.

398 The reduced maximal $\Delta\Psi_m$ in *g*$^{-/-}$ is also consistent with cristae remodeling. In contrast to
399 CV_2, CIV_2 assemblies such as $CIII_2CIV_2$ are comparatively flat and may be poorly
400 accommodated by the highly curved tubular cristae with 20 to 25 nm diameters (Fig. 3g,
401 Extended Data Fig. 4a,b and Extended Data Fig. 9d-f). A shift towards tubular morphology
402 would therefore reduce the membrane area available for CIV_2-containing supercomplexes, in
403 line with the observed decreases in $CIII_2CIV_2$ and overall CIV_2 abundance in *g*$^{-/-}$ (Fig. 3a).
404 Since CIV contributes to PMF generation, reduced capacity is expected to lower the upper
405 limit of mitochondrial polarization (Fig. 3h,i). ATP production and growth, however, are only
406 mildly affected, because physiological $\Delta\Psi_m$ does not need full capacity OXPHOS operation
407 to be maintained, thus does not decrease below the threshold that would compromise fitness[66]
408 (Fig. 3c,j and Extended Data Fig. 7e-g).
409

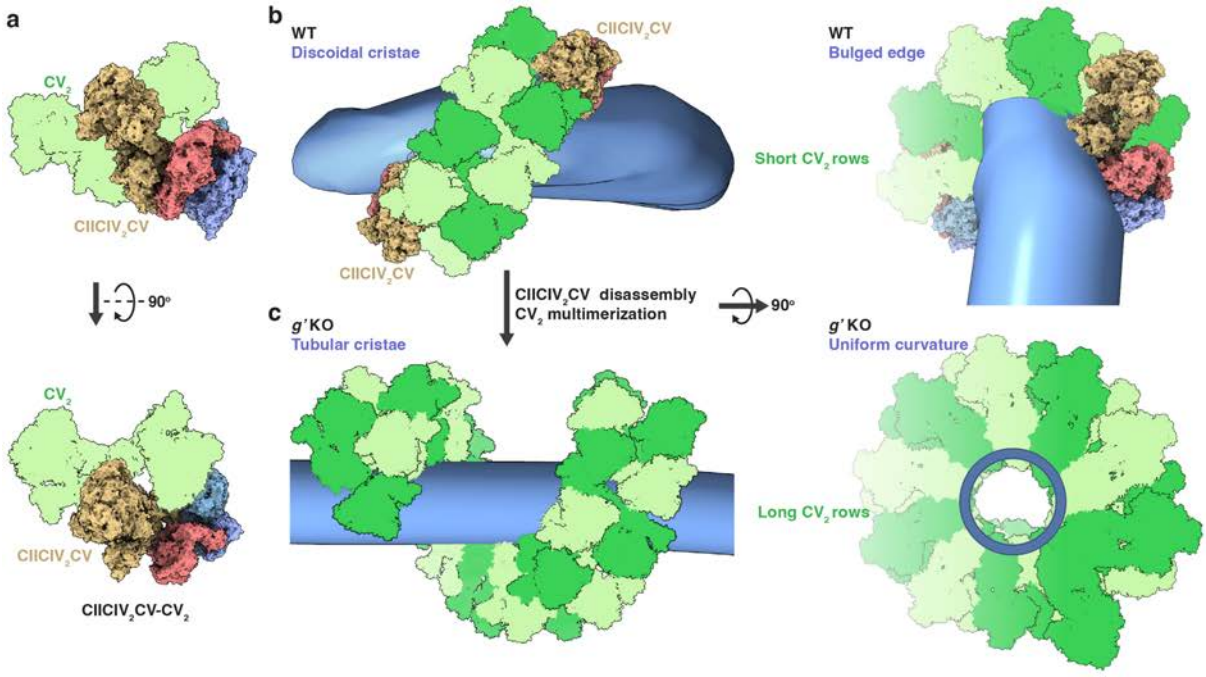

410

411 **Fig. 4 | Proposed mechanism of cristae morphogenesis quality control by $CIICIV_2CV$. a,**
412 Hypothetical model of $CIICIV_2CV$ (solid surfaces) associating with an ATP synthase dimer
413 (green silhouettes). **b,** In WT discoidal cristae, short CV_2 rows (schematized as four CV_2
414 units) are proposed to be capped at both ends by $CIICIV_2CV$, limiting row extension. **c,** In *g*$^{-/-}$
415 mitochondria, loss of $CIICIV_2CV$ removes this constraint, allowing CV_2 to assemble into
416 extended rows that impose cylindrical curvature and promote tubular cristae.
417

418 ***Discussion***

Mitochondrial OXPHOS is commonly depicted as two coordinated yet spatially segregated modules: an ETC that generates PMF and an ATP synthase that consumes it to produce ATP. Here we show that, in kinetoplastids, these functions can be integrated within a structurally defined supercomplex in which CII and CIV_2 associate directly with ATP synthase (Fig. 1). This supercomplex is a coordinated, multi-interface assembly rather than a fortuitous juxtaposition of stable modules. Cryo-EM reveals a clear organizing principle. The CV_2 homodimeric *g*/*g* module linking two CVs[4] is repurposed into a non-canonical, heterodimeric module built from two *g* paralogues, *g'* and *g''*, to resolve *g*/*g*'s geometrical incompatibility for CIV or other ETC complexes to associate. The new *g'*/*g''* module preserves the interlocking helical scaffold of the canonical interface while removes the steric features that would clash with CIV (Fig. 2a,b). Together with lineage-specific CII features and integral structural lipids, a rotary ATP synthase is integrated into ETC supercomplex without sterically obstructing catalysis, as proven by the presence of three rotational states in our cryo-EM dataset (Extended Data Fig. 3e).

A central implication of this organization is functional: disruption of the *g'*/*g''* module selectively destabilizes $CIICIV_2CV$, accompanied by pronounced remodeling of cristae from discoidal to elongated tubular morphologies (Fig. 3d-g, Extended Data Fig. 9 and Supplementary Videos 8 and 9). In contrast, steady-state bioenergetic outputs are only modestly affected, and physiological $\Delta\Psi_m$ measured in living cells remains largely unchanged, even though maximal polarization capacity under saturating substrate supply is reduced (Fig. 3c,h-j). This pattern supports a model that although the primary role of $CIICIV_2CV$ is architectural, it nonetheless maintains a reserve capacity for polarization by safeguarding cristae organization. Phylogenetic analysis places this mechanistic finding into evolutionary context[67] (Fig. 2f). The molecular innovations of subunit *g* enabling ETC-ATP synthase integration arose around the time canonical, PMF-generating CI[68–71] was lost or became highly divergent. This suggests temporal coincidence and plausible functional

446 linkage that in a CI-reduced context, the above architectural and functional duties, probably
447 originally attributed to CI or the respirasome, are taken over by the ETC-CV supercomplex.
448
449 The structure raises the possibility that physical proximity between the proton source and
450 sink could facilitate lateral proton transfer along the membrane surface[72–74] (Extended Data
451 Fig. 10a). Consistent with this, the supercomplex provides a plausible negatively charged
452 corridor on the IMS surface linking the putative proton exit of CIV_P[75,76] to the ATP
453 synthase lumenal half channel[6,28] (Extended Data Fig. 10b-d). However, two observations
454 argue against lateral proton transfer being the dominant physiological role of $CIICIV_2CV$.
455 First, the supercomplex lacks $CIII_2$, and thus cannot by itself represent a complete ETC
456 conduit from typical electron donors to oxygen. It must operate within a broader membrane
457 context that includes additional respiratory assemblies. It's nonetheless worth noting that the
458 limited interface in our $CIII_2CIV_2$ structure, observed elsewhere as well[77,78], imply
459 vulnerability to detergent conditions, suggesting that the native ETC-CV network may be
460 partially underrepresented in digitonin preparations (Extended Data Fig. 4a-d). More
461 importantly, genetic disruption of $CIICIV_2CV$ does not produce a major bioenergetic loss
462 under the conditions tested (Fig. 3c and Extended Data Fig. 7d). Together, these findings
463 return to Mitchell's point that oxidative phosphorylation is ultimately a systems problem,
464 defined by circuits, boundary conditions, and the physical constraints of the coupling
465 membrane[3]. In this context, the $CIICIV_2CV$ supercomplex exemplifies an emerging picture
466 that chemiosmosis anticipates but structural biology has rarely made explicit: supercomplexes
467 do not simply optimize bioenergetics kinetically[15,18,19,79], but can also stabilize the membrane
468 environment in which bioenergetics is possible, tuning curvature, available surface area, and
469 the spatial compatibility of OXPHOS components.
470
471 ***Conclusion***
472 Together, our structural, genetic, and computational analyses establish a *bona fide* ETC-ATP
473 synthase supercomplex. We identify a specific module of subunits *g'/g''* that rewires ATP

474 synthase assembly to couple the respiratory chain to cristae morphogenesis. It replaces the
475 canonical ATP synthase *g*/*g* dimerization interface and accommodates CIV_2 without
476 obstructing rotary catalysis. The resulting conversion of discoidal cristae into elongated
477 tubules, coupled with a reduced maximal polarization but modest steady-state bioenergetic
478 decline, argues that $CIICIV_2CV$ primarily functions as an architectural constraint preserving
479 cristae organization and bioenergetic reserve.
480
481 Our discovery provides a structural instantiation of the logic that transformed oxidative
482 phosphorylation from a search for chemical intermediates into a membrane-based systems
483 problem. In this sense, it extends Mitchell's chemiosmotic concept: beyond establishing a
484 proton motive force, oxidative phosphorylation depends on the hosting membrane geometry
485 and supramolecular organization that reliably generate that shape. Related architecture-
486 energetics couplings have been proposed in other lineages as well. For instances, steric
487 constraints imposed by respirasomes in euglenids[31,53] and the parallel organization of ETC
488 and ATP synthase spirals in ciliates[22,80] suggest that different eukaryotic groups may employ
489 different supramolecular solutions but converge on the same purpose to sculpt and stabilize a
490 specific type of cristae morphology.
491
492 **Methods**
493 *T. brucei culture and mitochondria isolation* - The Trypanosomiasis Research Edinburgh
494 University (TREU) 927 strain of *T. brucei* in its procyclic form were cultured at 27 °C, in
495 SDM-79 medium supplemented with 10% (v/v) fetal bovine serum (FBS)[4,81,82]. For
496 mitochondria isolation[22,50,53], ~2.5×10^{10} cells were harvested by centrifugation at 4 °C and
497 11,000 × g for 10 minutes, washed in Wash buffer (20 mM sodium phosphate pH 8.0, 150
498 mM NaCl and 20 mM glucose), resuspended in Hypotonic buffer (1 mM Tris-HCl pH 8.0
499 and 1 mM EDTA), and disrupted by 100 strokes in a 40 ml Dounce homogenizer. The lysis
500 was stopped by immediate addition of 1 M sucrose to a final sucrose concentration of 0.25 M.
501 Crude mitochondria were pelleted by centrifugation at 4 °C and 16,000 × g for 15 minutes

and resuspended in Isotonic buffer (20 mM Tris-HCl pH 8.0, 250 mM sucrose, 5 mM $MgCl_2$ and 0.3 mM $CaCl_2$). DNase I treatment was performed by addition of 13 mg/ml stock to a final DNase I concentration of 5 µg/ml and incubation on ice for 60 minutes. One volume of the STE buffer (20 mM Tris-HCl pH 8.0, 250 mM sucrose, 2 mM EDTA) was added and mitochondria were pelleted by centrifugation at 4 °C and 16,000 × g for 15 minutes. The pellet was again resuspended in minimal volume of STE buffer and loaded on a discontinuous sucrose gradient with 30%, 45%, and 60% sucrose (w/v) in STE buffer. Loaded gradients were centrifuged at 4 °C and 29,000 rpm for 2 hours in an Optima XPN Ultracentrifuge using a SW32 Ti rotor (Beckman Coulter). Fine mitochondria vesicles were harvested from the 45-60% sucrose interface, further diluted by STE buffer to 50 ml and pelleted again by centrifugation at 4 °C and 16,000 × g for 15 minutes. The fine mitochondria pellet was labeled by its measured mass and stored at -80 °C until use.

Sodium dodecyl sulphate, blue native polyacrylamide electrophoresis and immunoblotting - Small scale mitochondria isolation for electrophoretic purpose was done as following[4,83]. 2.5 × 10^8 cells were harvested by centrifugation at 4 °C and 1,300 × g for 10 minutes and resuspended in 10 ml Wash Buffer as a washing step. The cells were pelleted again, resuspended in 3 ml of Hypotonic buffer and then homogenized for 8 strokes in a 7 ml Dounce homogenizer. The isotonicity was restored by adding 600 µl of 60% sucrose in Hypotonic buffer followed by 3 additional strokes. The homogenate was centrifuged at 4 °C and 15,000 × g for 10 minutes and resuspended in 700 µl of STM buffer (20 mM Tris pH 8.0, 2 mM $MgCl_2$ and 250 mM sucrose). 3 µl each of 1 M $MgCl_2$, 0.1 M $CaCl_2$ and 4 U/µl DNase I was added to the resuspension, followed by incubation on ice for 1 hour with gentle agitation. 760 µl STE buffer was added to the resuspension, which was then aliquoted in equal volumes into two 1.5 ml microcentrifuge tubes and centrifuged at 4 °C and 15,000 × g for 10 minutes. The crude mitochondrial pellet was flash-frozen in liquid nitrogen and stored at −80 °C.

For denaturing sodium dodecyl sulfate-polyacrylamide gel electrophoresis (SDS-PAGE), whole cell lysates were prepared from cells resuspended in PBS buffer (10 mM phosphate buffer, 130 mM NaCl, pH 7.3). The suspension was mixed with an equal volume of 2 × SDS loading buffer (150 mM Tris-HCl, pH 6.8, 300 mM 1,4-dithiothreitol, 6% (w/v) SDS, 30% (w/v) glycerol, and 0.02% (w/v) bromophenol blue) to a final concentration of 1×10^7 cells in 30 µl. The lysates were boiled at 100 °C for 10 min and separated on 5-12% gradient Tris-glycine polyacrylamide gels.

For blue native polyacrylamide electrophoresis (BN-PAGE), crude mitochondria of each strain were solubilized in 80 µl MX buffer (30 mM HEPES pH 7.7, 150 mM potassium acetate, 0.002% PMSF and 10% (v/v) glycerol) with 10% digitonin with gentle agitation at 4 °C for 1 hour. Lysate was cleared by centrifugation at 4 °C and 16,000 × g for 30 minutes and the total protein concentration was estimated by BCA assay. Mitochondrial lysate with 10 µg total protein was mixed with 1.5 µl loading dye (500 mM ε-aminocaproic acid (ACA), 5% (w/v) Coomassie Brilliant Blue G-250), added by 50% (v/v) glycerol to a final glycerol concentration of 5%. Total volume of each sample was replenished to 20 µl by MX buffer. BN-PAGE was performed with 3-12% Bis-Tris gel (Invitrogen) using a program of 80 V for 15 minutes, 100 V for 3.5 hours and 130 V for 0.5 hour at 4 °C.

For immunoblotting of both SDS-PAGE and BN-PAGE, bands on the gel were transferred onto a PVDF membrane by electroblotting at 100 V for 1.5 hours at 4 °C. The PVDF membrane was blocked by incubation with 5% skimmed milk in 1 × PBST (8.5 mM Na_2HPO_4 and 1.5 mM KH_2PO_4 pH 7.4 ± 0.1, 137 mM NaCl, 2.7 mM KCl and 0.05% Tween-20), followed by incubation with primary antibody against CII subunit SDHA, $CIII_2$ subunit UQCRFS1 Rieske domain, CIV subunit COXEG7 or CV subunit β, and secondary anti-rabbit antibody, all diluted in 1 × PBST with 5% skimmed milk. The PVDF membrane was then incubated in the Super ECL Detection Reagent ECL (YEASEN) and chemiluminescence was detected on a Fully Automated Chemiluminescence Image Analysis System (Tanon). The

levels of $CIII_2$ and mitochondrial 70kDa heat shock protein (mtHsp70) were used as the internal loading controls of the immunoblots of BN-PAGE and SDS-PAGE, respectively.

Electron transport chain and ATP synthase supercomplex purification - All the following biochemical steps were performed at 4 °C unless otherwise stated. To isolate the membrane fraction of *T. brucei* mitochondria, the fine mitochondria pellet was thawed and homogenized in milli-Q H_2O at 10 ml per gram of mitochondria mass using a KIMBLE Dounce tissue grinder. The homogenate was added by 3 M KCl to a final KCl concentration of 150 mM and homogenized again to dissociate the peripheral membrane proteins. The homogenate was pelleted by centrifugation at 32,000 × g for 45 minutes, resuspended by homogenization in M10 buffer (20 mM Tris pH 7.4, 50 mM NaCl, 1 mM EDTA, 2 mM DTT, 0.002% PMSF (w/v) and 10% glycerol (v/v)) at 18 ml per gram of mitochondria mass as a washing step and pelleted again by centrifugation again at 32,000 × g for 45 minutes. The resulting mitochondrial membrane pellet was weighed and resuspended in buffer M10 at 1.5 ml per gram of membrane mass by homogenization. Total protein concentration was determined using a bicinchoninic acid (BCA) assay kit (Beijing LABLEAD Trading Co., Ltd.) following the manufacturer's instructions. The mitochondrial membrane was then added by M90 buffer (20 mM Tris pH 7.4, 50 mM NaCl, 1 mM EDTA, 2 mM DTT, 0.002% PMSF (w/v) and 90% glycerol (v/v)) to a final glycerol concentration of 30% (v/v) and stored at -80 °C until use.

For electron transport chain complexes and ATP synthase supercomplexes purification, mitochondrial membrane containing ~200 mg total protein was thawed and solubilized in MX buffer added by 2% digitonin at a detergent-to-protein ratio of 2:1 (w/w) for 2 hours with gentle agitation. After removal of insoluble materials by centrifugation at 16,000 × g for 45 minutes, the supernatant was loaded onto a continuous 10-45% (w/v) sucrose gradient in SGB buffer (15 mM HEPES pH 7.7, 20 mM KCl and 5 mM $MgCl_2$) added by 0.015% glyco-diosgenin (GDN (w/v)) and centrifuged at 29,000 rpm for 20 hours in an Optima XPN Ultracentrifuge using a SW32 Ti rotor (Beckman Coulter). The gradients were then manually

fractionated into 1 ml fractions, which were then subjected to BN-PAGE. To stain with CIV activity, the gel was incubated in CIV buffer of 50 mM sodium phosphate pH 7.2, 0.05% 3,3-diaminobenzidine tetrahydrochloride and 50 μM commercial porcine heart cytochrome *c* (Macklin). To stain with ATP synthase/CV activity, the gel was incubated in CV buffer of 50 mM glycine pH 8.5, 5 mM $MgCl_2$, 5 mM ATP and 2 mM $Pb(CH_3COO)_2$. Both staining was carried out at room temperature (RT) by slow agitation overnight. Fractions displaying CIV or CV activity were pooled and loaded onto a 5 ml Q-Sepharose HP column (Cytiva) equilibrated in Q-A buffer (30 mM Tris pH 7.4, 50 mM NaCl, 2 mM $MgCl_2$, 0.002% PMSF (w/v), 10% glycerol (v/v) and 0.015% GDN) for anion exchange chromatography (ANX). The column was first washed with 25 ml of Q-A buffer and then eluted with a 100 ml linear gradient from 0% to 100% Q-B buffer (Q-A buffer with 1 M NaCl) mixed in Q-A buffer. ANX fractions were again subjected to BN-PAGE and staining of CIV and CV activities. Fractions containing supercomplex $CIICIV_2CV$ were judged by presence of both CIV and CV activities at its highest electrophoretic position. Fractions containing supercomplex $CIII_2CIV_2$ were judged by presence of CIV activity at the electrophoretic positions lower than $CIICIV_2CV$ but higher than individual $CIII_2$ or CIV_2. The rest fractions with CIV activity contain mostly individual $CIII_2$ and CIV_2. These three groups of fractions were respectively pooled, concentrated and loaded onto the Superose 6 Increase 10/300 GL column (Cytiva) for size-exclusion chromatography (SEC) equilibrated in SEC Buffer (20 mM Tris pH 7.4, 50 mM NaCl, 5 mM $MgCl_2$, 0.002% PMSF and 0.015% GDN (w/v)). SEC fractions were again subjected to BN-PAGE and staining of CIV and CV activities. The fractions corresponding to relatively pure supercomplex $CIICIV_2CV$, supercomplex $CIII_2CIV_2$ and individual $CIII_2$/CIV_2 were directly used for cryo-EM grid preparation before snap freezing and storage in liquid N_2.

Cryo-EM grid preparation and data collection - The cryo-EM grid preparation and data collection were carried out at the Center of Cryo-Electron Microscopy at Zhejiang University. For each of the three fractions representing $CIICIV_2CV$, $CIII_2CIV_2$ and

$CIII_2/CIV_2$, 3 µl sample was applied to a pre-glow discharged Quantifoil R1.2/1.3 300 mesh copper grid coated with 2 nm continuous carbon layer, before blotting for 1.5 s under 100% humidity at 4 °C and vitrification in liquid ethane by Vitrobot Mark IV (Thermo Fisher). Grids were stored in liquid N_2 until use. Cryo-EM micrographs were collected on a Titan Krios G2 microscope (Thermo Fisher) operating at 300 kV, equipped with a Selectris energy filter and a Falcon4i detector operating at 244 frames/s. EPU software was used for automated data collection following standard procedures. For all three datasets, the grids were imaged at a calibrated magnification of × 105,000 with a physical pixel size of 1.2 Å and a defocus range from -0.8 to -2.0 µm. A total dose of 52.00 $e^-/Å^2$ with 7.10 s exposure time was fractionated into 1,733 frames. A total of 13,347, 12,510 and 1,511 raw micrographs were collected for $CIICIV_2CV$, $CIII_2CIV_2$ and $CIII_2/CIV_2$ datasets respectively.

Cryo-EM image processing - Raw micrographs of all three datasets were imported into cryoSPARC (v4.4.1)[84] for patch motion correction and contrast transfer function (CTF) estimation.

For the $CIICIV_2CV$ dataset, 5,950,660 particles were initially picked and extracted using boxsize 448. Subsequent 2D classification and multi-class 3D *ab-initio* reconstruction yielded 579,050 particles corresponding to supercomplex $CIICIV_2CV$ that were used for initial overall homogeneous refinement and non-uniform refinement[85] with global and local CTF corrections[86] under C1 symmetry, giving a final overall resolution of 2.83 Å. However, the *c*-ring and F_1 regions of CV were barely visible in the refined overall map. Local refinements focused on CII, CIV_2, the membrane region of the CV stator (CV_F_o_stator) and the $\alpha_3\beta_3$ region + the part of γ subunit that's embedded inside $\alpha_3\beta_3$ (CV_$\alpha_3\beta_3\gamma_{top}$) gave resolutions of 2.83 Å, 2.71 Å, 2.80 Å and 3.47 Å, respectively. A composite map ($CIICIV_2CV_{mem}$) combining local refinements of CII, CIV_2 and CV_F_o_stator was generated using the Combine Focused Maps program in Phenix-1.20.1[87]. 3D classification without alignment was performed using particles from the above CV_$\alpha_3\beta_3\gamma_{top}$ local refinement and the CV_$\alpha_3\beta_3\gamma_{top}$

mask as both solvent and focus masks. This classification gave three sensible classes, with 33,147, 43,117 and 47,450 particles respectively, corresponding to the rotational states 1-3 of CV. These three classes refined to overall resolutions of 3.11 Å, 3.06 Å and 3.03 Å respectively. For each class, local refinements were performed on CII, CIV_2, CV_F_o_stator, CV_$\alpha_3\beta_3\gamma_{top}$, CV_*c*-ring+$\gamma_{bottom}$ and CV_peripheral_stalk regions, giving resolutions ranging from 2.86 Å to 3.94 Å. Composite maps of the entire $CIICIV_2CV$ were generated as above for each CV rotational state using these local refinement maps[87].

For the $CIII_2CIV_2$ dataset, 6,343,816 particles were initially picked and extracted using boxsize 448. Following 2D classification, 111,499 particles that shows possible supercomplex assembly of $CIII_2$ and CIV_2 were manually selected and subjected to 3D *ab-initio* reconstruction with only one class to generate the initial reference volume[84]. Overall homogeneous refinement and non-uniform refinement[85] with both global and local CTF corrections[86] under C1 symmetry gave a reconstruction at 2.84 Å, but the CIV_2 region was much less visible than the $CIII_2$ region in this overall map. To separate supercomplex $CIII_2CIV_2$ from individual $CIII_2$, local refinement was first performed on these 111,499 particles focusing on the CIV_2 region, which gave a resolution of 3.54 Å. Particles from this CIV_2 local refinement were then exported to Relion-4.0[88] for subsequent 3D classification without alignment masking the same CIV_2 region. This approach identified a class of 21,346 particles with well-defined CIV_2 density, which refined to an overall resolution of 3.31 Å. Local refinements of this class focusing on the $CIII_2$ and CIV_2 regions gave resolutions of 3.14 Å and 3.23 Å, respectively. Composite map of supercomplex $CIII_2CIV_2$ were generated as above using these two local refinements[87].

For the $CIII_2/CIV_2$ dataset, 762,590 particles were initially picked and extracted using boxsize 256. Following 2D classification and multi-class 3D *ab-initio* reconstruction, 293,996 $CIII_2$ and 82,850 CIV_2 particles were selected[84]. Overall homogeneous refinements

and non-uniform refinements[85] with global and local CTF corrections under C1 symmetry gave maps with overall resolutions of 2.65 Å for $CIII_2$ and 2.75 Å for CIV_2[86].

Model building and refinement - All manual model building was performed in Coot-0.9.6[89]. Mainchain backbones for conserved subunits were built by first rigid-body fitting published structures into respective local refinement maps in ChimeraX[90–92], then manually adjust in Coot according to densities[89]. Reference models used to facilitate model building included porcine CII (PDB 1ZOY)[93], *T. thermophila* CII, $CIII_2$ and CIV_2 (PDB 8B6G, 8B6J and 8B6H)[21], *E. gracilis* $CIII_2$ and CIV (PDB 8IUF)[53] and *T. brucei* CV (PDB 8APA)[4]. Mainchain backbones of non-CV Tb-specific subunits were built *de novo* according to density. Sequences of each subunit were identified according to published methods[94]. Briefly, for each subunit side chains were first 'guessed' *de novo* according to a segment of density with high resolution, then this segment of sequence were used as a query for BLAST search against *T. brucei* proteome either from UniProt (UP000008524)[95,96] or from the TriTrypDB website[97,98]. The manually built CII, $CIII_2$, CIV_2 and CV subunits were rigid-body fitted into the $CIII_2$, CIV_2 and composite $CIICIV_2CV$ and $CIII_2CIV_2$ maps with chain ID adjusted as in Supplementary Tables 3 and 4[90–92]. Automatic model refinements were performed using the phenix.refine[99] and phenix.real_space_refine[100] programs, initially using automatically generated secondary structure restraints, custom bond linkage and custom ligand description file in Phenix-1.20.1. The output models were then manually edited according to refinement outcomes in Coot[89], with assistance from secondary structure information predicted by AlphaFold[101]. The next round of automatic refinements were then performed and this iterative process continues until the refined model reported high model-map correlation and good geometric statistics[102].

Sequence analysis - Homology detection of the OXPHOS complexes subunits (Supplementary Table 5) was done running (PSI-)Blast[103] against the Discoba proteomes with default cutoffs, and with HHPred[104] for proteins available in the HHpred database (PDB

proteins, and proteins from *N. fowleri, T. brucei* and *T. thermophila*). *Leishmania* proteins were detected at the genus level, the ID of the *Leishmania major* protein was recorded when available, otherwise the ID of other *Leishmania* species was recorded. When no homologs could be detected at the level of predicted proteins, tblastn was used to search for potential proteins that were missed in the automated protein prediction for that species, e.g., subunit *g'* in *B. saltans*. For the proteins for which structures were available, e.g., from *E. gracilis*, homology detection was also done by comparing 3D structures, leading e.g., to assignment of *T. brucei* protein Q583E7 to subunit COX7A. For the CV subunits the results were compared with the analysis of Sinha et al[105]. Most of the results were consistent, except for subunit *k* in *Andalucia godoyi* (ANDGO_05913.mRNA.1) that we could not confirm and subunit *g* in *T. thermophila* (XP_001032300.2) that was structurally not homologous to canonical subunit *g*, based on the *T. thermophila* CV_2 structure (PDB: 6YNY)[30]. The *g* subunit phylogeny was created with neighbor joining, using the identity matrix and correcting for multiple substitutions and using MrBayes 3.2.6 at www.phylogeny.fr with default settings[106]. The alignment was created with clustalX[107]. The final tree was visualized and annotated using the Interactive Tree of Life (iTOL) tool[108–110] to generate a circular layout figure.

Atomistic molecular dynamics simulations of CIICIV$_2$CV supercomplex - The 3.03 Å cryo-EM structure of the CIICIV$_2$CV supercomplex was used to construct the fully atomistic simulation model system. The F_1 part of the CV complex was truncated to keep the system size tractable with the α_3, β_3, γ, δ, ε, OSCP, ATPTB3, ATPTB4 and three p18 subunits and the F_1 regions of subunits *d* and 8 excluded. All protein subunits from other complexes were included in the model. Missing loops in subunits SDHTB6 (residue 102-115), SDHTB10 (residue 46-55), SDHB1 (residue 169-183) and SDHTB5 (residue 192-202 and 337-348) were filled using Modeller software[111]. All structurally resolved lipids were included in the model system. Protonation states of titratable amino acid residues were defined using PropKa[112]. Force field parameters of redox-active cofactors were taken from the literature or the CHARMM-GUI small molecule library; copper and heme centers of CIV, and FeS

clusters, FAD and quinone of CII[113–117]. All redox-active cofactors were modelled in their oxidized states except the Cu_B center of CIV, which was in cuprous form. The FAD molecule of CII was modelled without covalent linkage to the protein. The protein, lipids, ions and water solvent (see more below) were described using the CHARMM36 forcefield[118].

To construct the lipid membrane around the supercomplex, we applied the following procedure. The OPM-aligned[119] models of CIV_2 (PDB 1V55)[120] and CV_2 (PDB 6B2Z)[34] were superposed to the supercomplex. Individual, pre-equilibrated membrane patches, comprising 75% POPE, 20% POPC and 5% TLCL, were obtained from CHARMM-GUI[115] and were then aligned to each of the OPM-based orientations. The CIV_2- and CV_2-aligned membrane patches were found to be in good agreement with the structural lipids within the supercomplex structure. A third membrane patch was constructed to achieve periodic boundary conditions (PBCs) and to allow sufficient space for protein-lipid equilibration and relaxation. The *c*-ring of CV was filled with four POPC-molecules with two lipids each facing one of the two sides of the membrane. The membrane-protein system was then solvated in a TIP3P water box, neutralized and ionized with 0.15 mol/l NaCl. The final simulation box size was 290 Å × 500 Å × 255 Å, comprising ca. 3.3 million atoms.

A stepwise equilibration protocol was employed to relax the protein-membrane-solvent system by gradually releasing restraints from different parts of the system (Supplementary Table 6). First, an energy minimization of the entire system was performed for 50,000 steps without any restraints. Following this, the system was equilibrated in an NVT-ensemble, using the v-rescale thermostat[121]. Next, four NPT-steps followed, using different restraints (Supplementary Table 6), the v-rescale thermostat[121] and the Berendsen barostat[122]. The force constant of the harmonic restraints was 2000 kJ/mol/nm^2. For production runs, the Nosé-Hoover thermostat[123] and the Parrinello-Rahman barostat[124] were employed to maintain a pressure of 1 atm and 310 K temperature, respectively. Long-range electrostatics were calculated using particle mesh-Ewald summation[125], and the LINCS-algorithm[126] was used to

753 enable a time step of 2 fs. The cutoff for non-bonded interactions was 12 Å. Simulations were
754 performed with Gromacs-2022.4[127]. Three production runs of 500 ns length were performed
755 for each of the setup. Four different protein-membrane simulation setups were constructed a)
756 a wild-type system containing CIICIV$_2$CV supercomplex excluding the F_1 part of CV (see
757 above) b) CII-CIV$_2$ subcomplex in membrane, c) a CIICIV$_2$CV supercomplex without the *g'*
758 and d) *g''* subunit. An additional simulation setup containing only the lipid membrane was
759 also simulated for 100 ns with restraints 2000 kJ/mol/nm^2 on the CV-equivalent patch and for
760 100 ns without restraints.
761
762 The simulation data was analysed using VMD[128], MDAnalysis[129,130], Bendix[131] and the
763 Gromacs toolbox. Solvent-accessible surface area (SASA) was computed using the
764 GROMACS SASA module, which implements the Shake-Rupley algorithm with a probe
765 radius of 0.14 nm[132]. For each trajectory frame, SASA was calculated for selected CIV$_P$
766 complex, CV without *c*-ring, and the same selection treated as a single combined group.
767 Buried SASA corresponds to the solvent-exposed surface lost upon interaction between the
768 selected complexes, and was computed according as; Buried SASA = SASA(CIV$_P$) +
769 SASA(CV) – SASA(CIV$_P$CV). Figures and movies were produced using VMD[128] and
770 ffmpeg[133].
771
772 *Generation and verification of knock-out T. brucei cell lines* - All knock-out cell lines were
773 generated in procyclic *T. brucei* cells constitutively expressing T7 RNA polymerase, Tet
774 repressor and Cas9 nuclease from a single construct[134]. For the conditional expression of
775 COXTB2 and COXTB3, en ectopic tetracycline regulatable copy of the respective gene was
776 introduced to the parental strain by transfection of a *Not*I-linearized pLEW79-based construct
777 carrying the respective coding sequence (CDS) inserted between the *Bam*HI and *Hind*III sites
778 and the phleomycin resistance marker (Supplementary Table 7). Positive clones were selected
779 using phleomycin (2.5 μg/ml). To knockout both alleles of individual genes of interests, two
780 linear DNA molecules for expression of single guide RNAs (sgRNAs) and two repair

templates containing selection marker genes with UTRs flanked by homology arms targeting their recombination to the locus of interest were generated by polymerase chain reaction (PCR) with oligonucleotides designed using the LeishGEdit tool[135] (Supplementary Table 7). The repair templates were amplified from donor plasmids pPOTv5 (hygromycin) and pHD2164 (neomycin). The cells were electroporated with a mixture of both sgRNAs and both repair templates (4 µg each) using Amaxa Nucleofactor II. Clonal populations of knockout cells were selected in SDM79 medium supplemented with hygromycin (5 µg/ml) and G418 (2.5 µg/ml). In the selected clones, the absence of CDS of gene of interest and presence of the two selection markers was verified by PCR with specific primers (Supplementary Table 7). The sequences of all oligonucleotides are provided in Supplementary Table 7.

Mitochondrial ATP synthesis, membrane potential and reactive oxygen species generation measurements - ATP production measurements were performed as described previously with following modifications[4,136]. A total of 10^8 cells were harvested, washed with PBS (pH 7.4), and resuspended in 600 mM sorbitol, 20 mM Tris-HCl, 2 mM EDTA, pH 7.75, with 0.015% (w/v) digitonin for 5 minutes on ice. The organellar pellet was collected by centrifugation (4,000 × g, 3 minutes, 4 °C) and was resuspended in 75 µl of ATP production assay buffer (600 mM sorbitol, 10 mM $MgSO_4$, 15 mM potassium phosphate buffer pH 7.4, 20 mM Tris-HCl pH 7.4, 2.5 mg/ml fatty acid-free BSA). Samples were treated with 5 mM succinate (sodium salt) and 67 µM ADP to induce ATP production. Control samples were preincubated with the inhibitors malonate (6.7 mM), potassium cyanide (1 mM), or carboxyatractyloside (6.5 µM) for 10 minutes at room temperature. After 30 minutes at room temperature, 1.5 µl of 70% perchloric acid was added and the samples were incubated for 10 minutes on ice and centrifuged (maximum speed, 5 minutes, 4 °C). The supernatant (60 µl) was collected and neutralized by the addition of 11.5 µl of 1M KOH. After centrifugation, ATP concentration in the resulting supernatant was measured using the Roche ATP Bioluminescence Assay Kit HS

II in a Tecan Spark plate reader. The luminescence values obtained with the knockout strains were normalized against those from the wildtype samples.

To measure *in situ* mitochondrial membrane potential ($\Delta\Psi m$) in intact cells[137], a total of 10^6 cells were harvested by centrifugation, resuspended in SDM79 with 60 nM tetramethylrhodamine ethyl ester (TMRE), and incubated for 30 minutes at 27 °C in the dark. After incubation, cells were pelleted, resuspended in 1 ml of PBS (pH 7.4), and analyzed by flow cytometry (FACSymphony A1 Cell Analyzer, BD Biosciences, San Jose, CA). A total of 10,000 events were collected from each sample. The protonophore carbonyl cyanide 4-(trifluoromethoxy)phenylhydrazone (FCCP; 20 µM) was used to depolarize the membrane in control samples.

Spectrofluorometric assessment of mitochondrial membrane polarization in digitonin-permeabilized cells using safranin O dye (Sigma S2255) was performed as described previously with some modifications[4]. Briefly, 2×10^7 cells were pelleted (1,300 *g*, 10 minutes, RT) and washed with 1 ml of ANT buffer (8 mM KCl, 110 nM K-gluconate, 10 mM NaCl, 10 mM free-acid HEPES, 10 mM K_2HPO_4, 0.015 mM EGTA potassium salt, 10 mM mannitol, 0.5 mg/ml fatty acid-free BSA, 1.5 mM $MgCl_2$, pH 7.25). The cells were permeabilized by 8 µM digitonin (Sigma D141) in 2 ml of ANT buffer with 5 µM safranin O. Fluorescence was recorded for 750 s in Hitachi F-7000 spectrofluorimeter (Hitachi High Technologies) with the following parameters: 2 Hertz acquisition rate and 495 nm and 585 nm excitation and emission wavelengths, respectively. 5 mM succinate (Sigma S2378) and 1 mM potassium cyanide were added after 300 s and 600 s, respectively. The uncoupler SF 6847 (250 nM; Enzo Life Sciences BML-EI215-0050) was added to serve as a control for maximal depolarization.

For reactive oxygen species (ROS) production measurement[137], 5×10^6 *T. brucei* cells in the exponential growth phase were pelleted (1,300 g, 10 minutes, RT), resuspended in SDM79

with 5 µM MitoSOX Red Mitochondrial Superoxide dye (Thermo Fisher Scientific Waltham, MA), and incubated for 30 minutes at 27 °C. After incubation, cells were washed with phosphate buffered saline (PBS; pH 7.4), resuspended in 1 ml of PBS, and immediately analyzed by flow cytometry (FACSymphony A1 Cell Analyzer, BD Biosciences, San Jose, CA). For all samples, 10,000 events were collected.

Conventional transmission electron microscopy - *T. brucei* pellets were prepared for transmission electron microscopy (TEM) using a modified protocol based on Knott et al[138,139]. Dehydration was performed using a graded acetone series (30, 50, 70, 80, 90, 95, and 100%, 15 min each), followed by infiltration with SPI-Pon resin (SPI) using acetone–resin mixtures at ratios of 1:2, 1:1, and 2:1 (1 h each), and overnight incubation in pure embedding medium under vacuum in a desiccator. Polymerization was carried out at 62 °C for 48 h.

Ultrathin sections (70 nm) for conventional TEM and semithin sections (200 nm) for electron tomography were prepared using an EM UC7 ultramicrotome (Leica), collected on 300-mesh copper grids (SPI), and carbon coated. TEM images were acquired using a JEM-1400Flash transmission electron microscope (JEOL) equipped with a Xarosa CMOS camera (EMSYS). Electron tomography tilt series were collected over an angular range of ±60° with 1° increments using a 200 kV JEM-2100F microscope (JEOL) equipped with a K2 Summit direct electron detector (Gatan) and controlled by SerialEM[140]. The pixel size was set to 0.67 or 0.84 nm. Tomogram reconstruction, filtering, 3D model visualization, and quantitative measurements were performed using the IMOD software package[141].

Quantification of crista length, lumen diameter, and crista junction diameter - For initial screening to quantify elongated crista in *g'* and *g''* knockouts versus parental WT *T. brucei* strains, 109 cristae were measured from 35 (WT), 46 ($g'^{-/-}$) and 41 ($g''^{-/-}$) TEM images using Fiji[142] as previously described[139]. Briefly, the Line Selection Tool was used to draw a straight line connecting each crista rim in WT crista or each visible end of the elongated tubular

crista. The Measure tool was used to record the length of each line. The same approach was used to measure crista lumen diameter and crista junction diameter in the indicated number of virtual sections of reconstructed tomogram in Fig. 3f,g. Cristae length of elongated cristae was quantified in 3D using IMOD by measuring the length of a three-dimensional line tracing the central axis of each crista. These measurements were depicted schematically in Extended Data Fig. 9a. GraphPad Prism version 10.6.1 was used to plot data and calculate statistical significance was calculated using Welch's t test.

Statistics and reproducibility - All bioenergetic and MD measurements were performed with three biologically independent replicates and represented as the mean ± standard error of the mean (SEM), following generally accepted rules. All statistical tests and regressions were performed in GraphPad Prism (version 10.2.0). For ATP production assay (Fig. 3c), two-way analysis of variance (ANOVA) with Tukey's multiple-comparisons test was performed to compare between pairs of individual means. For $\Delta\Psi_m$ measurements (Fig. 3i,j), ROS production assay (Extended Data Fig. 7d) and buried SASA calculations (Fig. 3b), ordinary one-way ANOVA with Tukey's multiple-comparisons test was performed to compare between pairs of individual means. For random crista length measurements from reconstructed tomographs (Fig. 3f), unpaired two-tailed *t*-test was performed to compare between WT and $g^{-/-}$ means. For random crista length measurements from TEM images (Extended Data Fig. 9c), ordinary one-way ANOVA with Holm-Šídák's multiple-comparisons test was performed to compare between pairs of individual means. A significance in difference was defined as follows: ****, $P < 0.0001$; ***, $P < 0.001$; **, $P < 0.01$; *, $P < 0.05$ and not statistically significant (NS), $P > 0.05$.

Data availability: The composite maps and structural models and for *T. brucei* mitochondrial supercomplexes are available from the Electron Microscopy Database (EMDB) and the Protein Data Bank (PDB) and with the following accession codes. $CIICIV_2CV_{state1}$: EMD-67252 and PDB-9XTV; $CIICIV_2CV_{state2}$: EMD-67253 and PDB-

892 9XTW; CIICIV$_2$CV$_{state3}$: EMD-67254 and PDB-9XTX; CIICIV$_2$CV$_{mem}$: EMD-67255 and
893 PDB-9XTY; CIII$_2$CIV$_2$: EMD-67256 and PDB-9XTZ; CIII$_2$: EMD-67189 and PDB-9XT1;
894 CIV$_2$: EMD-67192 and PDB-9XT9. Maps for consensus and local refinements are available
895 from the EMDB with the following accession codes. CIICIV$_2$CV$_{state1}$: consensus map EMD-
896 67205, CII region EMD-67206, CIV$_2$ region EMD-67207, CV_F$_o$_stator region EMD-67208,
897 CV_$\alpha_3\beta_3\gamma_{top}$ region EMD-67209, CV_*c*-ring+γ_{bottom} region EMD-67210, CV_peripheral_stalk
898 region EMD-67211; CIICIV$_2$CV$_{state2}$: consensus map EMD-67212, CII region EMD-67213,
899 CIV$_2$ region EMD-67214, CV_F$_o$_stator region EMD-67215, CV_$\alpha_3\beta_3\gamma_{top}$ region EMD-
900 67216, CV_*c*-ring+γ_{bottom} region EMD-67217, CV_peripheral_stalk region EMD-67218;
901 CIICIV$_2$CV$_{state3}$: consensus map EMD-67219, CII region EMD-67220, CIV$_2$ region EMD-
902 67221, CV_F$_o$_stator region EMD-67222, CV_$\alpha_3\beta_3\gamma_{top}$ region EMD-67223, CV_*c*-
903 ring+γ_{bottom} region EMD-67224, CV_peripheral_stalk region EMD-67225; CIICIV$_2$CV$_{mem}$:
904 consensus map EMD-67226, CII region EMD-67227, CIV$_2$ region EMD-67228,
905 CV_F$_o$_stator region EMD-67229; CIII$_2$CIV$_2$: consensus map EMD-67230, CIII$_2$ region
906 EMD-67231, CIV$_2$ region EMD-67232.
907

References

1. Davies, K. M. *et al.* Macromolecular organization of ATP synthase and complex I in whole mitochondria. *Proceedings of the National Academy of Sciences of the United States of America* **108**, 14121–6 (2011).
2. MITCHELL, P. Coupling of phosphorylation to electron and hydrogen transfer by a chemi-osmotic type of mechanism. *Nature* **191**, 144–8 (1961).
3. Mitchell, P. Chemiosmotic coupling in oxidative and photosynthetic phosphorylation. *Biological reviews of the Cambridge Philosophical Society* **41**, 445–502 (1966).
4. Gahura, O. *et al.* An ancestral interaction module promotes oligomerization in divergent mitochondrial ATP synthases. *Nature communications* **13**, 5989 (2022).
5. Wikström, M., Sharma, V., Kaila, V. R. I., Hosler, J. P. & Hummer, G. New perspectives on proton pumping in cellular respiration. *Chemical reviews* **115**, 2196–221 (2015).
6. Walker, J. E. The ATP synthase: the understood, the uncertain and the unknown. *Biochemical Society transactions* **41**, 1–16 (2013).
7. Vercellino, I. & Sazanov, L. A. The assembly, regulation and function of the mitochondrial respiratory chain. *Nature reviews. Molecular cell biology* **23**, 141–161 (2022).
8. Fernández-Vizarra, E. & Ugalde, C. Cooperative assembly of the mitochondrial respiratory chain. *Trends in biochemical sciences* **47**, 999–1008 (2022).
9. Zhang, L. *et al.* Structural basis for the regulatory mechanism of mammalian mitochondrial respiratory chain megacomplex-I2III2IV2. *hLife* **2**, 189–200 (2024).
10. Vercellino, I. & Sazanov, L. A. Structure and assembly of the mammalian mitochondrial supercomplex CIII2CIV. *Nature* **598**, 364–367 (2021).
11. Rathore, S. *et al.* Cryo-EM structure of the yeast respiratory supercomplex. *Nature structural & molecular biology* **26**, 50–57 (2019).

12. Moe, A., Dimogkioka, A.-R., Rapaport, D., Öjemyr, L. N. & Brzezinski, P. Structure and function of the S. pombe III-IV-cyt c supercomplex. *Proceedings of the National Academy of Sciences of the United States of America* **120**, e2307697120 (2023).

13. Letts, J. A., Fiedorczuk, K. & Sazanov, L. A. The architecture of respiratory supercomplexes. *Nature* **537**, 644–648 (2016).

14. Wu, M., Gu, J., Guo, R., Huang, Y. & Yang, M. Structure of Mammalian Respiratory Supercomplex I1III2IV1. *Cell* **167**, 1598-1609.e10 (2016).

15. Letts, J. A., Fiedorczuk, K., Degliesposti, G., Skehel, M. & Sazanov, L. A. Structures of Respiratory Supercomplex I+III2 Reveal Functional and Conformational Crosstalk. *Molecular cell* **75**, 1131-1146.e6 (2019).

16. Davies, K. M., Blum, T. B. & Kühlbrandt, W. Conserved in situ arrangement of complex I and III2 in mitochondrial respiratory chain supercomplexes of mammals, yeast, and plants. *Proceedings of the National Academy of Sciences of the United States of America* **115**, 3024–3029 (2018).

17. Vercellino, I. & Sazanov, L. A. SCAF1 drives the compositional diversity of mammalian respirasomes. *Nature structural & molecular biology* **1**, (2024).

18. Liang, C. *et al.* Formation of I2+III2 supercomplex rescues respiratory chain defects. *Cell metabolism* **37**, 441-459.e11 (2025).

19. Shin, Y.-C. *et al.* Structural basis of respiratory complex adaptation to cold temperatures. *Cell* **187**, 6584-6598.e17 (2024).

20. Guo, R., Zong, S., Wu, M., Gu, J. & Yang, M. Architecture of Human Mitochondrial Respiratory Megacomplex I2III2IV2. *Cell* **170**, 1247-1257.e12 (2017).

21. Mühleip, A. *et al.* Structural basis of mitochondrial membrane bending by the I-II-III2-IV2 supercomplex. *Nature* **615**, 934–938 (2023).

22. Han, F. *et al.* Structures of Tetrahymena thermophila respiratory megacomplexes on the tubular mitochondrial cristae. *Nature communications* **14**, 2542 (2023).

23. Wú, F. *et al.* Structure of the II2-III2-IV2 mitochondrial supercomplex from the parasite Perkinsus marinus. (2024). doi:10.1101/2024.05.25.595893

24. Zheng, W., Chai, P., Zhu, J. & Zhang, K. High-resolution in situ structures of mammalian respiratory supercomplexes. *Nature* **631**, 232–239 (2024).

25. Waltz, F. *et al.* In-cell architecture of the mitochondrial respiratory chain. *Science (New York, N.Y.)* **387**, 1296–1301 (2025).

26. Kohler, A., Barrientos, A., Fontanesi, F. & Ott, M. The functional significance of mitochondrial respiratory chain supercomplexes. *EMBO reports* **24**, e57092 (2023).

27. Pánek, T., Eliáš, M., Vancová, M., Lukeš, J. & Hashimi, H. Returning to the Fold for Lessons in Mitochondrial Crista Diversity and Evolution. *Current biology : CB* **30**, R575–R588 (2020).

28. Kühlbrandt, W. Structure and Mechanisms of F-Type ATP Synthases. *Annual review of biochemistry* **88**, 515–549 (2019).

29. Mühleip, A. W. *et al.* Helical arrays of U-shaped ATP synthase dimers form tubular cristae in ciliate mitochondria. *Proceedings of the National Academy of Sciences of the United States of America* **113**, 8442–7 (2016).

30. Flygaard, R. K., Mühleip, A., Tobiasson, V. & Amunts, A. Type III ATP synthase is a symmetry-deviated dimer that induces membrane curvature through tetramerization. *Nature communications* **11**, 5342 (2020).

31. Mühleip, A. W., Dewar, C. E., Schnaufer, A., Kühlbrandt, W. & Davies, K. M. In situ structure of trypanosomal ATP synthase dimer reveals a unique arrangement of catalytic subunits. *Proceedings of the National Academy of Sciences of the United States of America* **114**, 992–997 (2017).

32. Mühleip, A., McComas, S. E. & Amunts, A. Structure of a mitochondrial ATP synthase with bound native cardiolipin. *eLife* **8**, 1–23 (2019).

33. Davies, K. M., Anselmi, C., Wittig, I., Faraldo-Gómez, J. D. & Kühlbrandt, W. Structure of the yeast F1Fo-ATP synthase dimer and its role in shaping the mitochondrial cristae. *Proceedings of the National Academy of Sciences of the United States of America* **109**, 13602–7 (2012).

34. Guo, H., Bueler, S. A. & Rubinstein, J. L. Atomic model for the dimeric FO region of mitochondrial ATP synthase. *Science* **358**, 936–940 (2017).

35. Gu, J. *et al.* Cryo-EM structure of the mammalian ATP synthase tetramer bound with inhibitory protein IF1. *Science (New York, N.Y.)* **364**, 1068–1075 (2019).

36. Spikes, T. E., Montgomery, M. G. & Walker, J. E. Structure of the dimeric ATP synthase from bovine mitochondria. *Proceedings of the National Academy of Sciences of the United States of America* **117**, 23519–23526 (2020).

37. Spikes, T. E., Montgomery, M. G. & Walker, J. E. Interface mobility between monomers in dimeric bovine ATP synthase participates in the ultrastructure of inner mitochondrial membranes. *Proceedings of the National Academy of Sciences of the United States of America* **118**, 1–9 (2021).

38. Blum, T. B., Hahn, A., Meier, T., Davies, K. M. & Kühlbrandt, W. Dimers of mitochondrial ATP synthase induce membrane curvature and self-assemble into rows. *Proceedings of the National Academy of Sciences of the United States of America* **116**, 4250–4255 (2019).

39. Murphy, B. J. *et al.* Rotary substates of mitochondrial ATP synthase reveal the basis of flexible F1-Fo coupling. *Science (New York, N.Y.)* **364**, 543108 (2019).

40. Dietrich, L., Agip, A.-N. A., Kunz, C., Schwarz, A. & Kühlbrandt, W. In situ structure and rotary states of mitochondrial ATP synthase in whole Polytomella cells. *Science (New York, N.Y.)* **385**, 1086–1090 (2024).

41. Nesterov, S. *et al.* Ordered Clusters of the Complete Oxidative Phosphorylation System in Cardiac Mitochondria. *International journal of molecular sciences* **22**, 1–10 (2021).

42. Nakano, A. *et al.* Structures of respiratory supercomplexes and ATP synthase oligomers in mammalian mitochondrial inner membrane. *Nature communications* (2026). doi:10.1038/s41467-026-70578-x

1015 43. Acín-Pérez, R., Fernández-Silva, P., Peleato, M. L., Pérez-Martos, A. & Enriquez, J.
1016 A. Respiratory active mitochondrial supercomplexes. *Molecular cell* **32**, 529–39
1017 (2008).
1018 44. Ukolova, I. V. *et al.* New insights into the organisation of the oxidative
1019 phosphorylation system in the example of pea shoot mitochondria. *Biochimica et*
1020 *biophysica acta. Bioenergetics* **1861**, 148264 (2020).
1021 45. Miranda-Astudillo, H. V., Yadav, K. N. S., Boekema, E. J. & Cardol, P.
1022 Supramolecular associations between atypical oxidative phosphorylation complexes of
1023 Euglena gracilis. *Journal of bioenergetics and biomembranes* (2021).
1024 doi:10.1007/s10863-021-09882-8
1025 46. Burki, F., Roger, A. J., Brown, M. W. & Simpson, A. G. B. The New Tree of
1026 Eukaryotes. *Trends in ecology & evolution* **35**, 43–55 (2020).
1027 47. Zíková, A. Mitochondrial adaptations throughout the Trypanosoma brucei life cycle.
1028 *The Journal of eukaryotic microbiology* **69**, e12911 (2022).
1029 48. Bílý, T. *et al.* Ultrastructural Changes of the Mitochondrion During the Life Cycle of
1030 Trypanosoma brucei. *The Journal of eukaryotic microbiology* **68**, e12846 (2021).
1031 49. Morales, J. *et al.* Novel mitochondrial complex II isolated from Trypanosoma cruzi is
1032 composed of 12 peptides including a heterodimeric Ip subunit. *The Journal of*
1033 *biological chemistry* **284**, 7255–63 (2009).
1034 50. Zhou, L., Maldonado, M., Padavannil, A., Guo, F. & Letts, J. A. Structures of
1035 Tetrahymena's respiratory chain reveal the diversity of eukaryotic core metabolism.
1036 *Science (New York, N.Y.)* **376**, 831–839 (2022).
1037 51. Senoo, N. & Claypool, S. M. Emerging Roles of Phospholipids in the Structure and
1038 Function of the Oxidative Phosphorylation Complexes. in *The Dynamic Nature of*
1039 *Mitochondria* 63–86 (CRC Press, 2024). doi:10.1201/9781003221180-6
1040 52. Williamson, K. *et al.* A robustly rooted tree of eukaryotes reveals their excavate
1041 ancestry. *Nature* **640**, 974–981 (2025).

53. He, Z. *et al.* Euglena's atypical respiratory chain adapts to the discoidal cristae and flexible metabolism. *Nature communications* **15**, 1628 (2024).

54. Valach, M., Léveillé-Kunst, A., Gray, M. W. & Burger, G. Respiratory chain Complex I of unparalleled divergence in diplonemids. *The Journal of biological chemistry* **293**, 16043–16056 (2018).

55. Kaur, B. *et al.* Gene fragmentation and RNA editing without borders: eccentric mitochondrial genomes of diplonemids. *Nucleic acids research* **48**, 2694–2708 (2020).

56. Surve, S., Heestand, M., Panicucci, B., Schnaufer, A. & Parsons, M. Enigmatic presence of mitochondrial complex I in Trypanosoma brucei bloodstream forms. *Eukaryotic cell* **11**, 183–93 (2012).

57. David, V. *et al.* Gene Loss and Error-Prone RNA Editing in the Mitochondrion of Perkinsela, an Endosymbiotic Kinetoplastid. *mBio* **6**, e01498-15 (2015).

58. Gastineau, R. *et al.* Mitogenome sequence of a Black Sea isolate of the kinetoplastid Bodo saltans. *Mitochondrial DNA. Part B, Resources* **3**, 968–969 (2018).

59. Duarte, M. & Tomás, A. M. The mitochondrial complex I of trypanosomatids--an overview of current knowledge. *Journal of bioenergetics and biomembranes* **46**, 299–311 (2014).

60. Cermáková, P., Verner, Z., Man, P., Lukes, J. & Horváth, A. Characterization of the NADH:ubiquinone oxidoreductase (complex I) in the trypanosomatid Phytomonas serpens (Kinetoplastida). *The FEBS journal* **274**, 3150–8 (2007).

61. Verner, Z. *et al.* Comparative analysis of respiratory chain and oxidative phosphorylation in Leishmania tarentolae, Crithidia fasciculata, Phytomonas serpens and procyclic stage of Trypanosoma brucei. *Molecular and biochemical parasitology* **193**, 55–65 (2014).

62. Gerasimov, E. S. *et al.* Evolutionary divergent kinetoplast genome structure and RNA editing patterns in the trypanosomatid Vickermania. *Proceedings of the National Academy of Sciences of the United States of America* **122**, e2426887122 (2025).

63. Čermáková, P. *et al.* Differences in mitochondrial NADH dehydrogenase activities in trypanosomatids. *Parasitology* **148**, 1161–1170 (2021).

64. Kampjut, D. & Sazanov, L. A. The coupling mechanism of mammalian respiratory complex I. *Science (New York, N.Y.)* **370**, e0227226 (2020).

65. Nawathean, P. & Maslov, D. A. The absence of genes for cytochrome c oxidase and reductase subunits in maxicircle kinetoplast DNA of the respiration-deficient plant trypanosomatid Phytomonas serpens. *Current genetics* **38**, 95–103 (2000).

66. Hierro-Yap, C. *et al.* Bioenergetic consequences of FoF1-ATP synthase/ATPase deficiency in two life cycle stages of Trypanosoma brucei. *The Journal of biological chemistry* **296**, 100357 (2021).

67. Cabrera-Alarcón, J. L. *et al.* Structural diversity and evolutionary constraints of oxidative phosphorylation. *Cell genomics* 100945 (2025). doi:10.1016/j.xgen.2025.100945

68. Kravchuk, V. *et al.* A universal coupling mechanism of respiratory complex I. *Nature* **609**, 808–814 (2022).

69. Parey, K. *et al.* High-resolution structure and dynamics of mitochondrial complex I-Insights into the proton pumping mechanism. *Science advances* **7**, eabj3221 (2021).

70. Hernansanz-Agustín, P. *et al.* A transmitochondrial sodium gradient controls membrane potential in mammalian mitochondria. *Cell* 1–15 (2024). doi:10.1016/j.cell.2024.08.045

71. Kaila, V. R. I. Resolving Chemical Dynamics in Biological Energy Conversion: Long-Range Proton-Coupled Electron Transfer in Respiratory Complex I. *Accounts of chemical research* **54**, 4462–4473 (2021).

72. Heberle, J., Riesle, J., Thiedemann, G., Oesterhelt, D. & Dencher, N. A. Proton migration along the membrane surface and retarded surface to bulk transfer. *Nature* **370**, 379–82 (1994).

73. Nilsson, T. *et al.* Lipid-mediated Protein-protein Interactions Modulate Respiration-driven ATP Synthesis. *Scientific reports* **6**, 24113 (2016).

74. Sjöholm, J. *et al.* The lateral distance between a proton pump and ATP synthase determines the ATP-synthesis rate. *Scientific reports* **7**, 2926 (2017).

75. Kaila, V. R. I., Sharma, V. & Wikström, M. The identity of the transient proton loading site of the proton-pumping mechanism of cytochrome c oxidase. *Biochimica et biophysica acta* **1807**, 80–4 (2011).

76. Yano, N. *et al.* The Mg2+-containing Water Cluster of Mammalian Cytochrome c Oxidase Collects Four Pumping Proton Equivalents in Each Catalytic Cycle. *The Journal of biological chemistry* **291**, 23882–23894 (2016).

77. Maldonado, M., Guo, F. & Letts, J. A. Atomic structures of respiratory complex III2, complex IV, and supercomplex III2-IV from vascular plants. *eLife* **10**, 1–34 (2021).

78. MacLean, A. E. *et al.* Structure, assembly and inhibition of the Toxoplasma gondii respiratory chain supercomplex. *Nature structural & molecular biology* **32**, 1424–1433 (2025).

79. Calvo, E. *et al.* Functional role of respiratory supercomplexes in mice: SCAF1 relevance and segmentation of the Qpool. *Science advances* **6**, eaba7509 (2020).

80. Allen, R. D., Schroeder, C. C. & Fok, A. K. An investigation of mitochondrial inner membranes by rapid-freeze deep-etch techniques. *The Journal of cell biology* **108**, 2233–40 (1989).

81. Niemann, M. & Schneider, A. A Scalable Purification Method for Mitochondria from Trypanosoma brucei. *Methods in molecular biology (Clifton, N.J.)* **2116**, 611–626 (2020).

82. Schneider, A., Charrière, F., Pusnik, M. & Horn, E. K. Isolation of mitochondria from procyclic Trypanosoma brucei. *Methods in molecular biology (Clifton, N.J.)* **372**, 67–80 (2007).

83. Gahura, O. *et al.* The F1 -ATPase from Trypanosoma brucei is elaborated by three copies of an additional p18-subunit. *The FEBS journal* **285**, 614–628 (2018).

84. Punjani, A., Rubinstein, J. L., Fleet, D. J. & Brubaker, M. A. cryoSPARC: algorithms for rapid unsupervised cryo-EM structure determination. *Nature methods* **14**, 290–296 (2017).

85. Punjani, A., Zhang, H. & Fleet, D. J. Non-uniform refinement: adaptive regularization improves single-particle cryo-EM reconstruction. *Nature methods* **17**, 1214–1221 (2020).

86. Zivanov, J., Nakane, T. & Scheres, S. H. W. Estimation of high-order aberrations and anisotropic magnification from cryo-EM data sets in RELION-3.1. *IUCrJ* **7**, 253–267 (2020).

87. Liebschner, D. *et al.* Macromolecular structure determination using X-rays, neutrons and electrons: recent developments in Phenix. *Acta crystallographica. Section D, Structural biology* **75**, 861–877 (2019).

88. Kimanius, D., Dong, L., Sharov, G., Nakane, T. & Scheres, S. H. W. New tools for automated cryo-EM single-particle analysis in RELION-4.0. *The Biochemical journal* **478**, 4169–4185 (2021).

89. Emsley, P., Lohkamp, B., Scott, W. G. & Cowtan, K. Features and development of Coot. *Acta crystallographica. Section D, Biological crystallography* **66**, 486–501 (2010).

90. Pettersen, E. F. *et al.* UCSF ChimeraX: Structure visualization for researchers, educators, and developers. *Protein science : a publication of the Protein Society* **30**, 70–82 (2021).

91. Goddard, T. D. *et al.* UCSF ChimeraX: Meeting modern challenges in visualization and analysis. *Protein science : a publication of the Protein Society* **27**, 14–25 (2018).

92. Meng, E. C. *et al.* UCSF ChimeraX: Tools for structure building and analysis. *Protein science : a publication of the Protein Society* **32**, e4792 (2023).

93. Sun, F. *et al.* Crystal structure of mitochondrial respiratory membrane protein complex II. *Cell* **121**, 1043–57 (2005).

94. Ho, C.-M. *et al.* Bottom-up structural proteomics: cryoEM of protein complexes enriched from the cellular milieu. *Nature methods* **17**, 79–85 (2020).

95. Hall, N. *et al.* The DNA sequence of chromosome I of an African trypanosome: gene content, chromosome organisation, recombination and polymorphism. *Nucleic acids research* **31**, 4864–73 (2003).

96. Berriman, M. *et al.* The genome of the African trypanosome Trypanosoma brucei. *Science (New York, N.Y.)* **309**, 416–22 (2005).

97. Shanmugasundram, A. *et al.* TriTrypDB: An integrated functional genomics resource for kinetoplastida. *PLoS neglected tropical diseases* **17**, e0011058 (2023).

98. Aslett, M. *et al.* TriTrypDB: a functional genomic resource for the Trypanosomatidae. *Nucleic acids research* **38**, D457-62 (2010).

99. Afonine, P. V. *et al.* Towards automated crystallographic structure refinement with phenix.refine. *Acta crystallographica. Section D, Biological crystallography* **68**, 352–67 (2012).

100. Afonine, P. V. *et al.* Real-space refinement in PHENIX for cryo-EM and crystallography. *Acta crystallographica. Section D, Structural biology* **74**, 531–544 (2018).

101. Abramson, J. *et al.* Accurate structure prediction of biomolecular interactions with AlphaFold 3. *Nature* **630**, 493–500 (2024).

102. Williams, C. J. *et al.* MolProbity: More and better reference data for improved all-atom structure validation. *Protein science : a publication of the Protein Society* **27**, 293–315 (2018).

103. Altschul, S. F. *et al.* Gapped BLAST and PSI-BLAST: a new generation of protein database search programs. *Nucleic acids research* **25**, 3389–402 (1997).

104. Zimmermann, L. *et al.* A Completely Reimplemented MPI Bioinformatics Toolkit with a New HHpred Server at its Core. *Journal of molecular biology* **430**, 2237–2243 (2018).

105. Sinha, S. D. & Wideman, J. G. The persistent homology of mitochondrial ATP synthases. *iScience* **26**, 106700 (2023).

106. Ronquist, F. *et al.* MrBayes 3.2: efficient Bayesian phylogenetic inference and model choice across a large model space. *Systematic biology* **61**, 539–42 (2012).

107. Larkin, M. A. *et al.* Clustal W and Clustal X version 2.0. *Bioinformatics (Oxford, England)* **23**, 2947–8 (2007).

108. Letunic, I. & Bork, P. Interactive Tree Of Life (iTOL): an online tool for phylogenetic tree display and annotation. *Bioinformatics (Oxford, England)* **23**, 127–8 (2007).

109. Letunic, I. & Bork, P. Interactive Tree Of Life (iTOL) v5: an online tool for phylogenetic tree display and annotation. *Nucleic acids research* **49**, W293–W296 (2021).

110. Letunic, I. & Bork, P. Interactive Tree of Life (iTOL) v6: recent updates to the phylogenetic tree display and annotation tool. *Nucleic acids research* **52**, W78–W82 (2024).

111. Sali, A. & Blundell, T. L. Comparative protein modelling by satisfaction of spatial restraints. *Journal of molecular biology* **234**, 779–815 (1993).

112. Søndergaard, C. R., Olsson, M. H. M., Rostkowski, M. & Jensen, J. H. Improved Treatment of Ligands and Coupling Effects in Empirical Calculation and Rationalization of pKa Values. *Journal of chemical theory and computation* **7**, 2284–95 (2011).

113. Chang, C. H. & Kim, K. Density Functional Theory Calculation of Bonding and Charge Parameters for Molecular Dynamics Studies on [FeFe] Hydrogenases. *Journal of chemical theory and computation* **5**, 1137–45 (2009).

114. Johansson, M. P., Kaila, V. R. I. & Laakkonen, L. Charge parameterization of the metal centers in cytochrome c oxidase. *Journal of computational chemistry* **29**, 753–67 (2008).

115. Jo, S., Kim, T., Iyer, V. G. & Im, W. CHARMM-GUI: a web-based graphical user interface for CHARMM. *Journal of computational chemistry* **29**, 1859–65 (2008).

116. Smith, D. M. A., Xiong, Y., Straatsma, T. P., Rosso, K. M. & Squier, T. C. Force-Field Development and Molecular Dynamics of [NiFe] Hydrogenase. *Journal of chemical theory and computation* **8**, 2103–14 (2012).

117. Teixeira, V. H., Baptista, A. M. & Soares, C. M. Pathways of H2 toward the active site of [NiFe]-hydrogenase. *Biophysical journal* **91**, 2035–45 (2006).

118. Huang, J. & MacKerell, A. D. CHARMM36 all-atom additive protein force field: validation based on comparison to NMR data. *Journal of computational chemistry* **34**, 2135–45 (2013).

119. Lomize, M. A., Pogozheva, I. D., Joo, H., Mosberg, H. I. & Lomize, A. L. OPM database and PPM web server: Resources for positioning of proteins in membranes. *Nucleic Acids Research* **40**, 370–376 (2012).

120. Tsukihara, T. *et al.* The low-spin heme of cytochrome c oxidase as the driving element of the proton-pumping process. *Proceedings of the National Academy of Sciences of the United States of America* **100**, 15304–9 (2003).

121. Bussi, G., Donadio, D. & Parrinello, M. Canonical sampling through velocity rescaling. *The Journal of chemical physics* **126**, 014101 (2007).

122. Berendsen, H. J. C., Postma, J. P. M., van Gunsteren, W. F., DiNola, A. & Haak, J. R. Molecular dynamics with coupling to an external bath. *The Journal of Chemical Physics* **81**, 3684–3690 (1984).

123. Evans, D. J. & Holian, B. L. The Nose–Hoover thermostat. *The Journal of Chemical Physics* **83**, 4069–4074 (1985).

124. Parrinello, M. & Rahman, A. Polymorphic transitions in single crystals: A new molecular dynamics method. *Journal of Applied Physics* **52**, 7182–7190 (1981).

125. Darden, T., York, D. & Pedersen, L. Particle mesh Ewald: An N ·log(N) method for Ewald sums in large systems. *The Journal of Chemical Physics* **98**, 10089–10092 (1993).

126. Hess, B., Bekker, H., Berendsen, H. J. C. & Fraaije, J. G. E. M. LINCS: A linear constraint solver for molecular simulations. *Journal of Computational Chemistry* **18**, 1463–1472 (1997).

127. Abraham, M. J. *et al.* GROMACS: High performance molecular simulations through multi-level parallelism from laptops to supercomputers. *SoftwareX* **1**–**2**, 19–25 (2015).

128. Humphrey, W., Dalke, A. & Schulten, K. VMD: visual molecular dynamics. *Journal of molecular graphics* **14**, 33–8, 27–8 (1996).

129. Michaud-Agrawal, N., Denning, E. J., Woolf, T. B. & Beckstein, O. MDAnalysis: a toolkit for the analysis of molecular dynamics simulations. *Journal of computational chemistry* **32**, 2319–27 (2011).

130. Gowers, R. *et al.* MDAnalysis: A Python Package for the Rapid Analysis of Molecular Dynamics Simulations. in *Proceedings of the 15th Python in Science Conference* 98–105 (2016). doi:10.25080/Majora-629e541a-00e

131. Dahl, A. C. E., Chavent, M. & Sansom, M. S. P. Bendix: intuitive helix geometry analysis and abstraction. *Bioinformatics (Oxford, England)* **28**, 2193–4 (2012).

132. Eisenhaber, F., Lijnzaad, P., Argos, P., Sander, C. & Scharf, M. The double cubic lattice method: Efficient approaches to numerical integration of surface area and volume and to dot surface contouring of molecular assemblies. *Journal of Computational Chemistry* **16**, 273–284 (1995).

133. Tomar, S. Converting video formats with FFmpeg. *Linux Journal* **2006**, (2006).

134. Alves, A. A. *et al.* Control of assembly of extra-axonemal structures: the paraflagellar rod of trypanosomes. *Journal of cell science* **133**, (2020).

135. Beneke, T. & Gluenz, E. LeishGEdit: A Method for Rapid Gene Knockout and Tagging Using CRISPR-Cas9. *Methods in molecular biology (Clifton, N.J.)* **1971**, 189–210 (2019).

136. Schneider, A., Bouzaidi-Tiali, N., Chanez, A.-L. & Bulliard, L. ATP production in isolated mitochondria of procyclic Trypanosoma brucei. *Methods in molecular biology (Clifton, N.J.)* **372**, 379–87 (2007).

137. Doleželová, E. *et al.* Cell-based and multi-omics profiling reveals dynamic metabolic repurposing of mitochondria to drive developmental progression of Trypanosoma brucei. *PLoS biology* **18**, e3000741 (2020).

138. Knott, G., Rosset, S. & Cantoni, M. Focussed ion beam milling and scanning electron microscopy of brain tissue. *Journal of visualized experiments : JoVE* e2588 (2011). doi:10.3791/2588

139. Kaurov, I. *et al.* The Diverged Trypanosome MICOS Complex as a Hub for Mitochondrial Cristae Shaping and Protein Import. *Current biology : CB* **28**, 3393-3407.e5 (2018).

140. Mastronarde, D. N. Automated electron microscope tomography using robust prediction of specimen movements. *Journal of structural biology* **152**, 36–51 (2005).

141. Mastronarde, D. N. & Held, S. R. Automated tilt series alignment and tomographic reconstruction in IMOD. *Journal of structural biology* **197**, 102–113 (2017).

142. Schindelin, J. *et al.* Fiji: an open-source platform for biological-image analysis. *Nature methods* **9**, 676–82 (2012).

Acknowledgements: We thank Shenghai Chang, Lingyun Wu and Tingyu Liu from the Center of Cryo-Electron Microscopy (CCEM), Zhejiang University for technical assistance with cryo-EM grid vitrification, screening and data collection. We thank Cheng Ma and Liyan Wang from the Core Facilities, Zhejiang University School of Medicine for technical support with protein purification. We acknowledge the high-performance computing resources from the Center for Scientific Computing (CSC), Finland. We also thank the Faculty of Science, University of Helsinki for IT support. V.S. is thankful to Luka Simsive, Oleksii Zdorevskyi and Maria Andrea Mroginski for help with the force field parameters. This work was supported by the BC CAS core facility LEM funded by MEYS CR (LM2023050 Czech-BioImaging and OP VVV CZ.02.1.01/0.0/0.0/18_046/0016045).

Funding: This work was supported by the National Natural Science Foundation of China (32371253 to L.Z.), the National Special Support Program for High-Level Talents of China, Young Top-Notch Talents Program (to L.Z.), the Zhejiang Province Special Support Program for High-Level Talents, Young Talents Program (to L.Z.), the European Research Council grant (ERC805230 to A.A.), the project P JAC CZ.02.01.01/00/22_008/0004575 RNA for therapy, co-Funded by the European Union (to O.G.), the Czech Science Foundation grant 26-20429S (to O.G.), the Czech Science Foundation grant 23-07674S (to H.H.), the Research Council of Finland grant (to V.S.), the Jane and Aatos Erkko Foundation grant (to V.S), the Sigrid Jusélius Foundation grant (to V.S.), the University of Helsinki grant (to V.S.), the Cancer Foundation grant (to V.S), and the Finnish Society of Sciences and Letters grant (to V.S.). Work at the BC CAS LEM core facility was supported by MEYS CR (LM2023050 Czech-BioImaging and OP VVV CZ.02.1.01/0.0/0.0/18_046/0016045).

Author contributions: Conceptualization: L.Z., A.A.; Methodology: L.Z., A.A., O.G., V.S., H.H., M.A.H.; Investigation: Y.H., J.W., E.E., B.C., K.H., C.P., T.B., H.T., M.T., F.H., M.W., N.Z., Q.C., J.Z., D.L., A.Z., M.A.H., H.H., V.S., O.G., A.A., L.Z.; Writing-original draft: L.Z.; Writing-review and editing: L.Z., A.A., O.G., V.S., H.H., M.A.H.; Visualization:

Y.H., J.W., E.E., C.P., B.C., T.B., M.W., M.A.H., H.H., V.S., O.G., A.A., L.Z.; Funding acquisition: L.Z., A.A., O.G., V.S., H.H., M.A.H.; Resources: Q.C., J.Z., D.L., A.Z., M.A.H., H.H., V.S., O.G., A.A., L.Z.; Supervision: L.Z., A.A., O.G., V.S., H.H., M.A.H.; Project administration: L.Z.

Competing interests: The authors declare that they have no competing interests.

Correspondence and requests for materials should be addressed to Long Zhou.

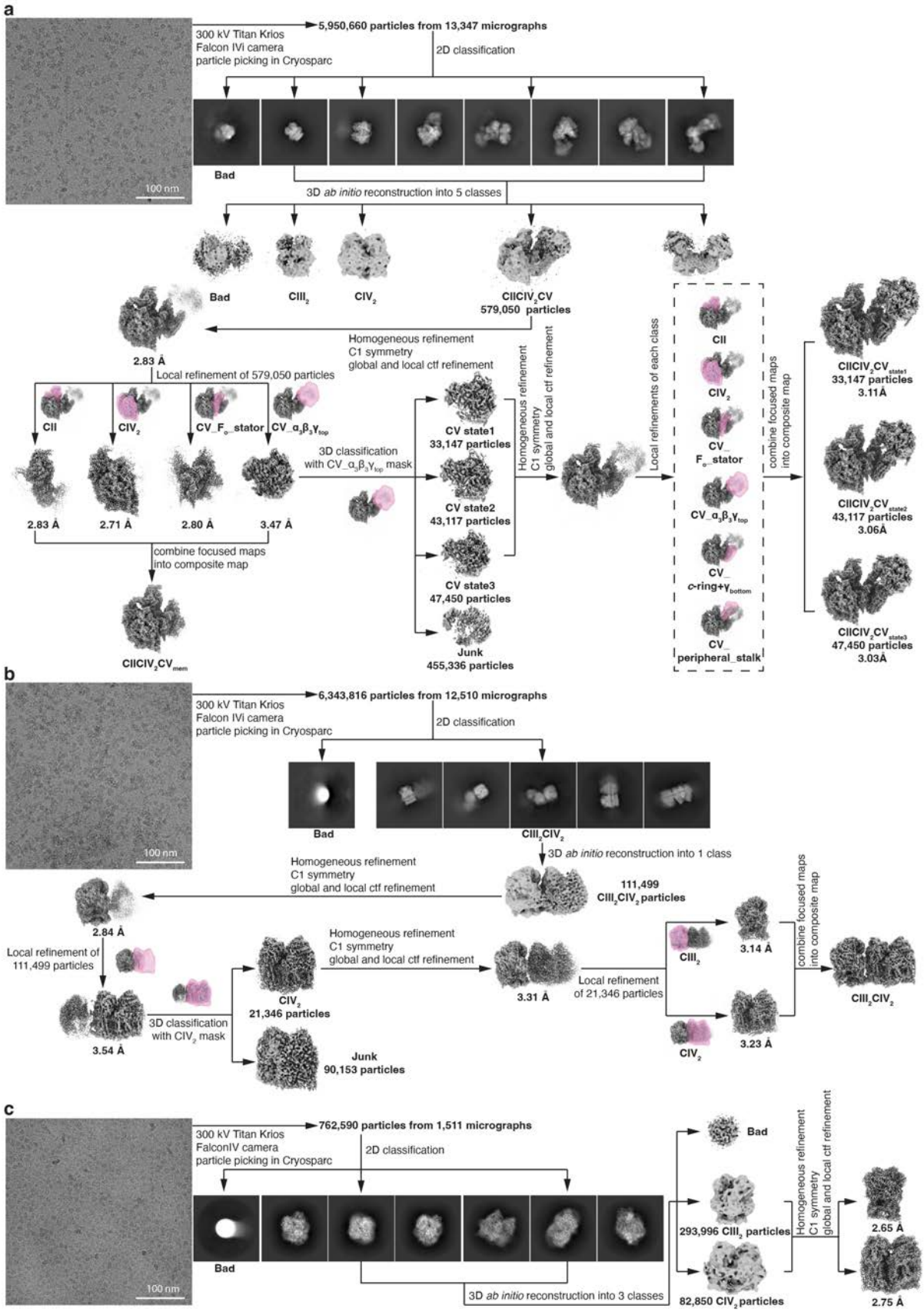

Extended Data Fig. 1 | Cryo-EM image processing of supercomplex CIICIV$_2$CV, CIII$_2$CIV$_2$, CIII$_2$ and CIV$_2$. a, A total of 13,347 micrographs were collected from a 300 kV Titan Krios microscope equipped with Falcon IVi camera, from which 5,950,660 particles

were initially picked and extracted using boxsize 448. A total of 579,050 supercomplex CIICIV$_2$CV particles were selected after 2D classification and multi-class 3D *ab-initio* reconstruction. Overall homogeneous and non-uniform refinements gave a final overall resolution of 2.83 Å, but *c*-ring and F$_1$ region of CV were barely visible. Local refinements of CII, CIV$_2$ and the membrane-embedded region of the CV stator (CV_F$_o$_stator) gave resolutions of 2.83 Å, 2.71 Å and 2.80 Å, respectively. A composite map (CIICIV$_2$CV$_{mem}$) combining local refinements of CII, CIV$_2$ and CV_F$_o$_stator represented the best resolution that could be achieved for the consensus region of CIICIV$_2$CV in different CV rotational states. Local refinement of the $\alpha_3\beta_3$ and the part of γ subunit that's embedded inside $\alpha_3\beta_3$ (CV_$\alpha_3\beta_3\gamma_{top}$) was also performed for further rotational state classification, giving a resolution of 3.47 Å. 3D classification using these locally refined particles gave three sensible classes corresponding to the rotational states 1-3 of CV. Overall homogeneous refinement, non-uniform refinement and local refinements of CII, CIV$_2$, CV_F$_o$_stator, CV_$\alpha_3\beta_3\gamma_{top}$, CV_*c*-ring+$\gamma_{bottom}$ and CV_peripheral_stalk regions were sequentially performed on particles of these three classes, giving resolutions ranging from 2.86 Å to 3.94 Å, followed by composite map generation. Masks used for individual local refinements are indicated as pink transparent surfaces. **b,** A total of 12,510 micrographs were collected in the CIII$_2$CIV$_2$ dataset and 6,343,816 particles were initially picked and extracted using boxsize 448. A total of 111,499 possible CIII$_2$CIV$_2$ particles were selected after 2D classification. 3D *ab-initio* reconstruction with only one class, overall homogeneous refinement and non-uniform refinement gave an overall resolution of 2.84 Å, but the CIV$_2$ region was barely visible. To separate supercomplex CIII$_2$CIV$_2$ from individual CIII$_2$, local refinement of the CIV$_2$ region was performed, giving a resolution of 3.54 Å. 3D classification masking CIV$_2$ separated 21,346 particles with well-defined CIV$_2$ density. These particles, representing supercomplex CIII$_2$CIV$_2$, refined to an overall resolution of 3.31 Å. Local refinements of the CIII$_2$ and CIV$_2$ regions gave resolutions of 3.14 Å and 3.23 Å, respectively, followed by composite map generation. **c,** A total of 1,511 micrographs were collected in the CIII$_2$/CIV$_2$ dataset and 762,590 particles were initially picked and extracted using boxsize 256. A total of 293,996 CIII$_2$ and 82,850 CIV$_2$ particles were selected after 2D classification and multi-class 3D *ab-initio* reconstruction. Overall homogeneous and non-uniform refinements gave final resolutions of 2.65 Å for CIII$_2$ and 3.01 Å for CIV$_2$.

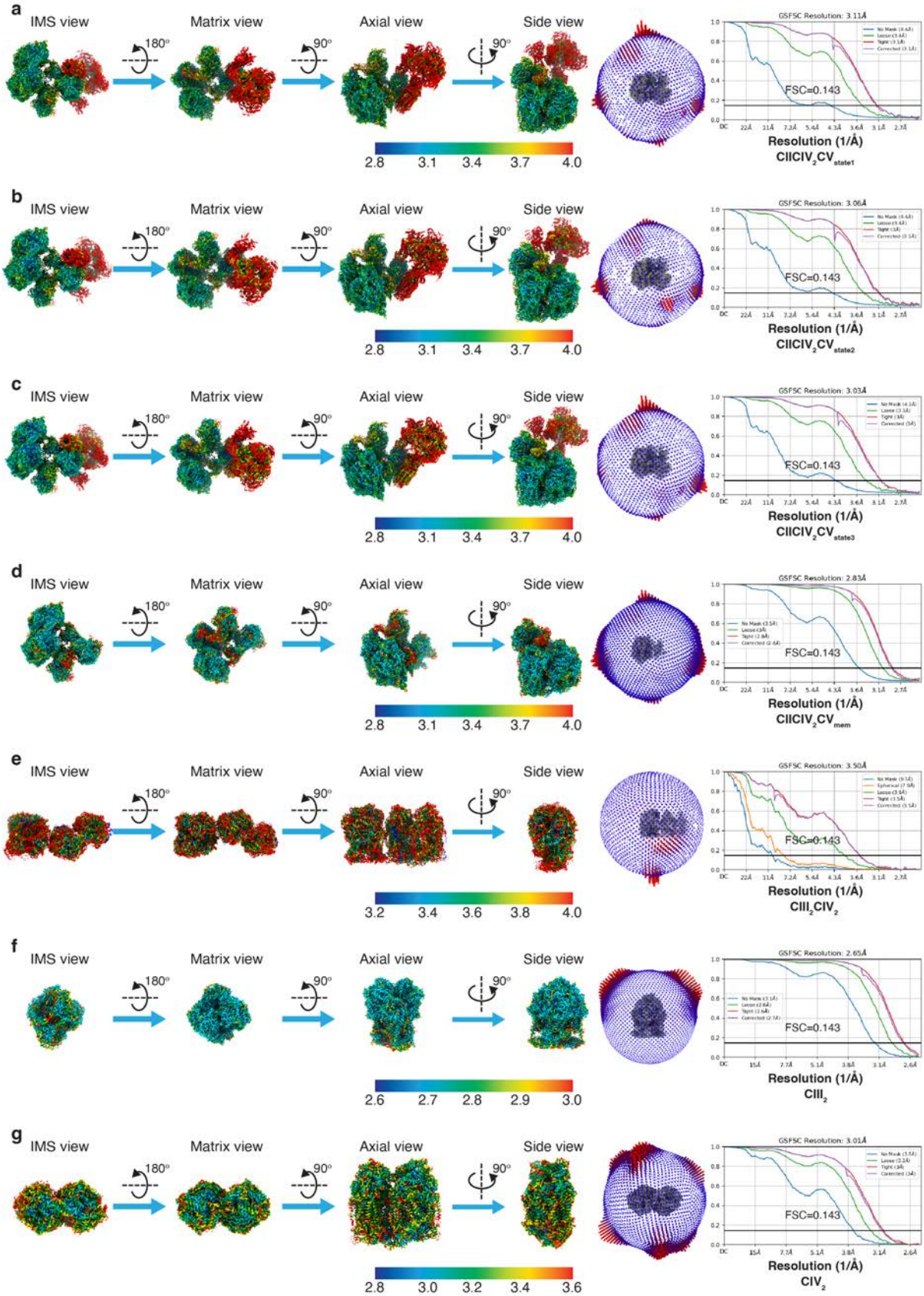

Extended Data Fig. 2 | Local resolution maps, projection orientation distributions and Fourier shell correlation (FSC) curves of $CIICIV_2CV$, $CIII_2CIV_2$, $CIII_2$ and CIV_2. a-d, Local resolutions are plotted on the cryo-EM maps or composite maps of $CIICIV_2CV_{state1}$ (**a**),

1352 $CIICIV_2CV_{state2}$ (**b**), $CIICIV_2CV_{state3}$ (**c**), $CIICIV_2CV_{mem}$ (**d**), $CIII_2CIV_2$ (**e**), $CIII_2$ (**f**) and
1353 CIV_2 (**g**) in different viewing directions. Orientational distributions of particle projections are
1354 individually plotted. FSC curves (gold standard FSC=0.143 for resolution estimation) of the
1355 corresponding consensus refinements are shown.

1356

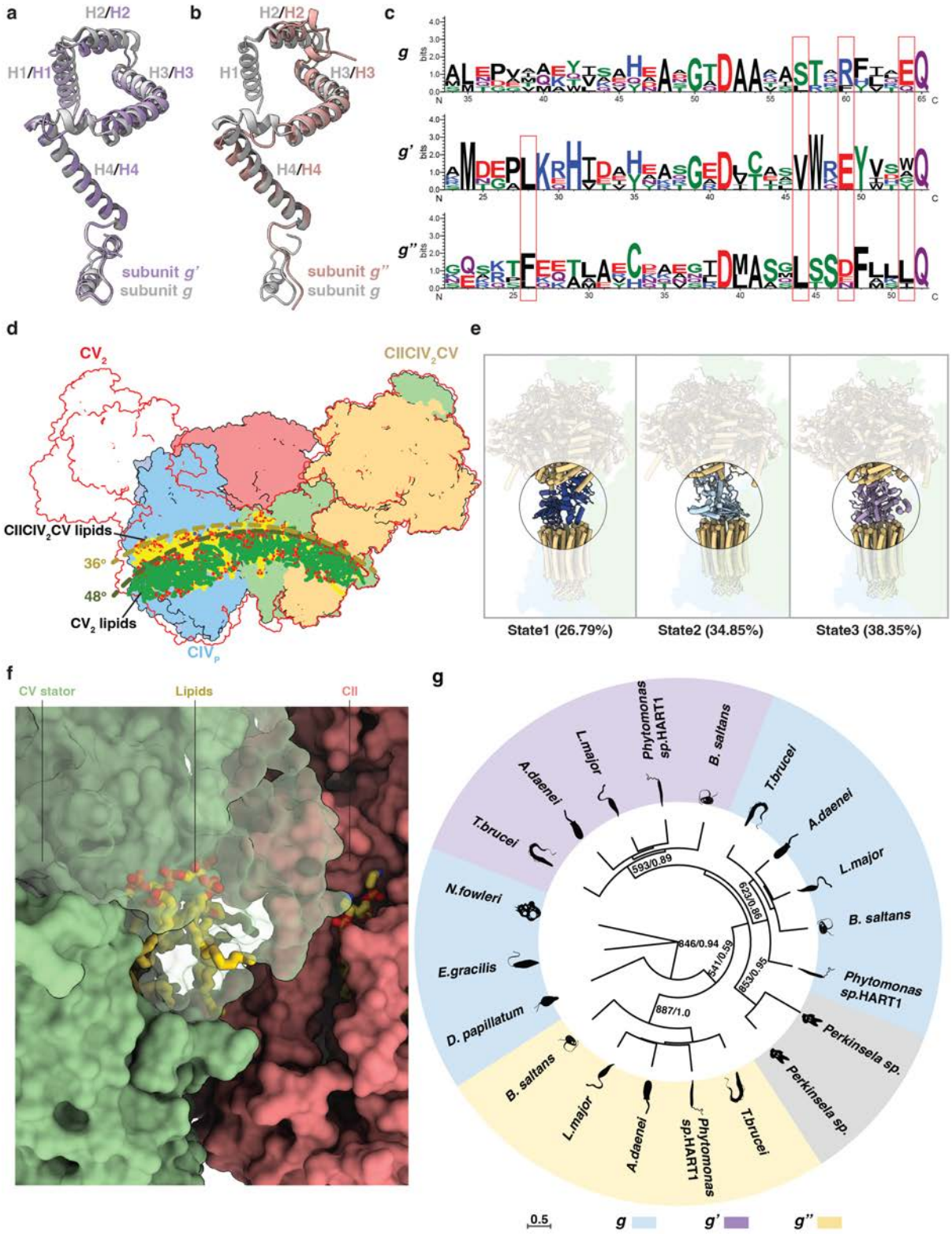

Extended Data Fig. 3 | Additional structural and evolutionary characteristics of *T. brucei* supercomplex CIICIV$_2$CV. a,b, Structural superpositions of subunit *g'* (purple, **a**) or *g''* (brown, **b**) with subunit *g* (grey). Numbering of helices are labeled. Note that subunit *g''* lacks the H1 as found in subunit *g* and *g'*. **c,** Sequence alignments of the *g*, *g'* and *g''* subunits respectively, using species *T. brucei*, *L. major*, *Angomonas deanei*, *Phytomonas sp.* HART1 and *B. saltans*, with residues numbered according to the *T. brucei* sequence. Residues that are conserved in at least one of these subunits but are considerably altered

across different subunits, such as reversed charge or polarity, are marked by red boxes. **d,** Side view of the structural superposition of the supercomplex CIICIV$_2$CV (colored silhouettes) and a CV$_2$ (PDB: 8AP6, empty silhouette), aligned by a common monomeric copy of CV. The steric clash is obvious between the other monomeric CV copy of CV$_2$ and the CIV$_P$ of CIICIV$_2$CV. **e,** The three rotational states of CV inside supercomplex CIICIV$_2$CV, highlighting the conformations of the rotationally asymmetric part of CV rotor, including the bottom part of subunit γ and subunits δ and ε. Morphing through the three rotational states is shown in Supplementary Video 1. Note that rotational State 3, as named after the nomenclature of *T. brucei* CV$_2$, is the most populated. **f,** Surface representation of the CII-CV interface within CIICIV$_2$CV supercomplex, displaying the bridging lipids (yellow sticks) in between. **g,** Circular presentation of the subunit *g* phylogeny within Discoba (see Methods), indicating two gene duplication events at the base of the kinetoplastids that have led to the *g*, *g'* and *g''* subunits. While the separation into three paralogous groups across kinetoplastids is strongly supported, the branching order of the subunits is unresolved. Note that *Perkinsela* appears to have undergone a parallel and independent duplication of the *g* subunit to the kinetoplastids and the two resultant *g* paralogues are colored in grey. The accession numbers of the sequences, from the innermost to the outermost clade in the circular tree: XP_011775304, CAD2222471, XP_001687526, CCW69062, CYKH01002228 (position 4653-5084 in the DNA sequence), XP_011771764, EPY39046, XP_001686043, CCW69339, CUG92605, KNH06072, KNH08985, XP_829068, CCW69283, EPY38894, XP_001686918, CUG89822, KAJ9452804, comp12813_c0_seq1, XP_002677150.

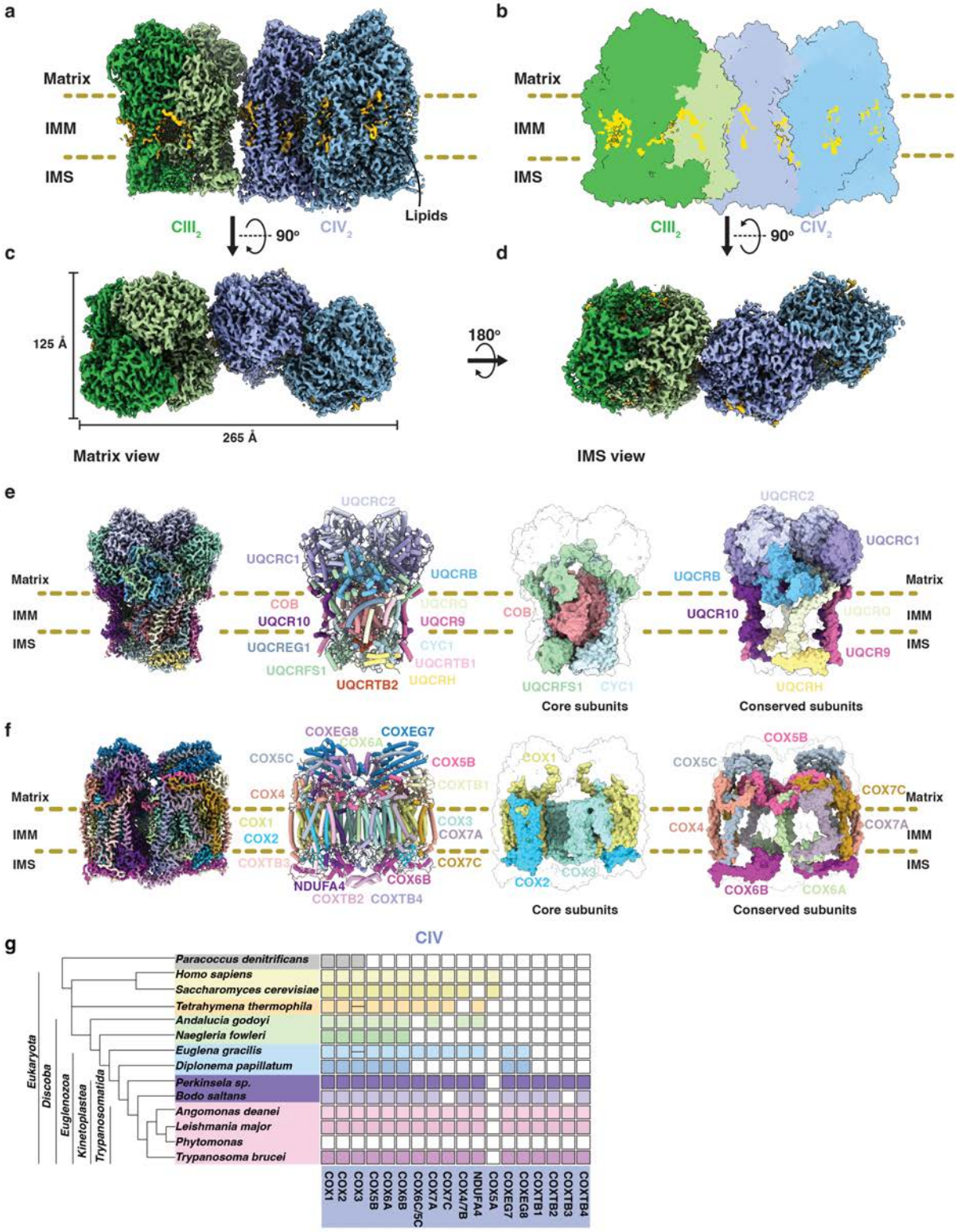

Extended Data Fig. 4 | Overall architecture, subunit organization and evolution of supercomplex $CIII_2CIV_2$. a,c,d, Side (**a**), matrix (**c**) and IMS (**d**) views of the cryo-EM map of the $CIII_2CIV_2$ supercomplex, colored by individual complexes. Key lipids are highlighted in yellow and labeled. **b,** Surface representation of the structural model of the $CIII_2CIV_2$ supercomplex in the same view as in (**a**). **e,f,** From left to right: cryo-EM maps, structures (cartoons) colored by individual subunits, core and conserved subunits (solid surfaces) colored individually, on top of the silhouette of complete $CIII_2$ (**e**) and CIV_2 (**f**). **g,**

Evolutionary distribution showing the presence (filled squares) or absence (empty squares) of CIV subunits across the same set of species as in Fig. 2f.

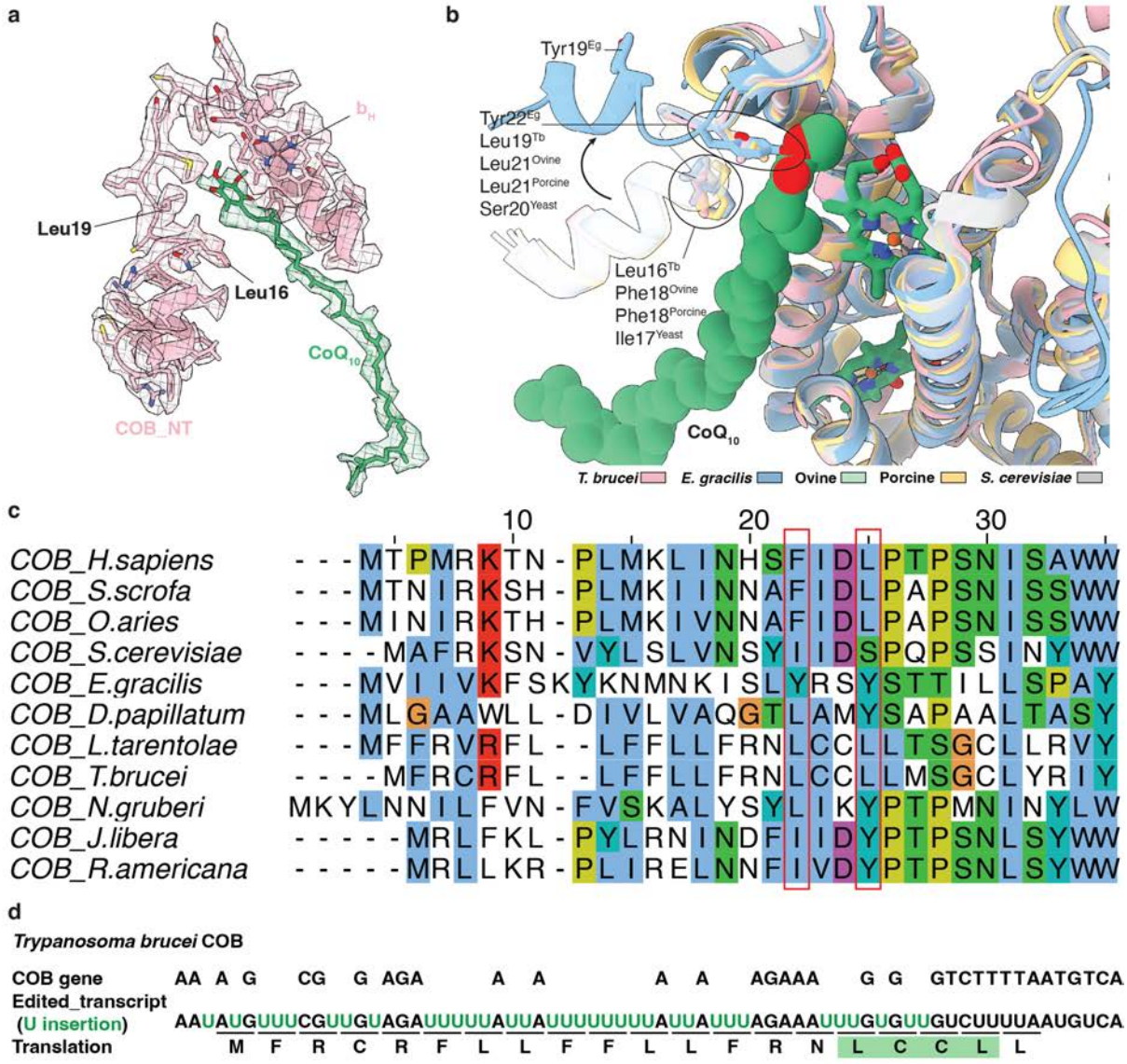

Extended Data Fig. 5 | Structural variations of the Q_N site in *T. brucei* $CIII_2$ due to COB transcript editing. a, The structural model (pink cartoon) and density (pink mesh) of the N-terminal region in *T. brucei* COB. Structure (green stick) and density (green mesh) of the nearby CoQ_{10} bound at the Q_N site is also shown. Key residues corresponding to the *E. gracilis* double tyrosine motif are shown as sticks and labeled. **b,** Structural superposition of COB subunits from *T. brucei* (pink), *E. gracilis* (PDB: 8IUF, blue), Ovine (PDB: 6Q9E, green), Porcine (PDB: 8UGD, yellow) and *Saccharomyces cerevisiae* (PDB: 9ETZ, grey). Residues corresponding to the *E. gracilis* double tyrosine motif are shown as sticks and labeled. The Q_N site CoQ_{10} is shown as green spheres. **c,** Sequence alignment of the COB from eleven eukaryotic species, displaying the N-terminal regions only. Residues corresponding to the *E. gracilis* double tyrosine motif are indicated by red boxes. **d,** Mitochondrial transcript editing of *T. brucei* COB with uridine insertions (green). The protein translation, in line with the structure, is listed below.

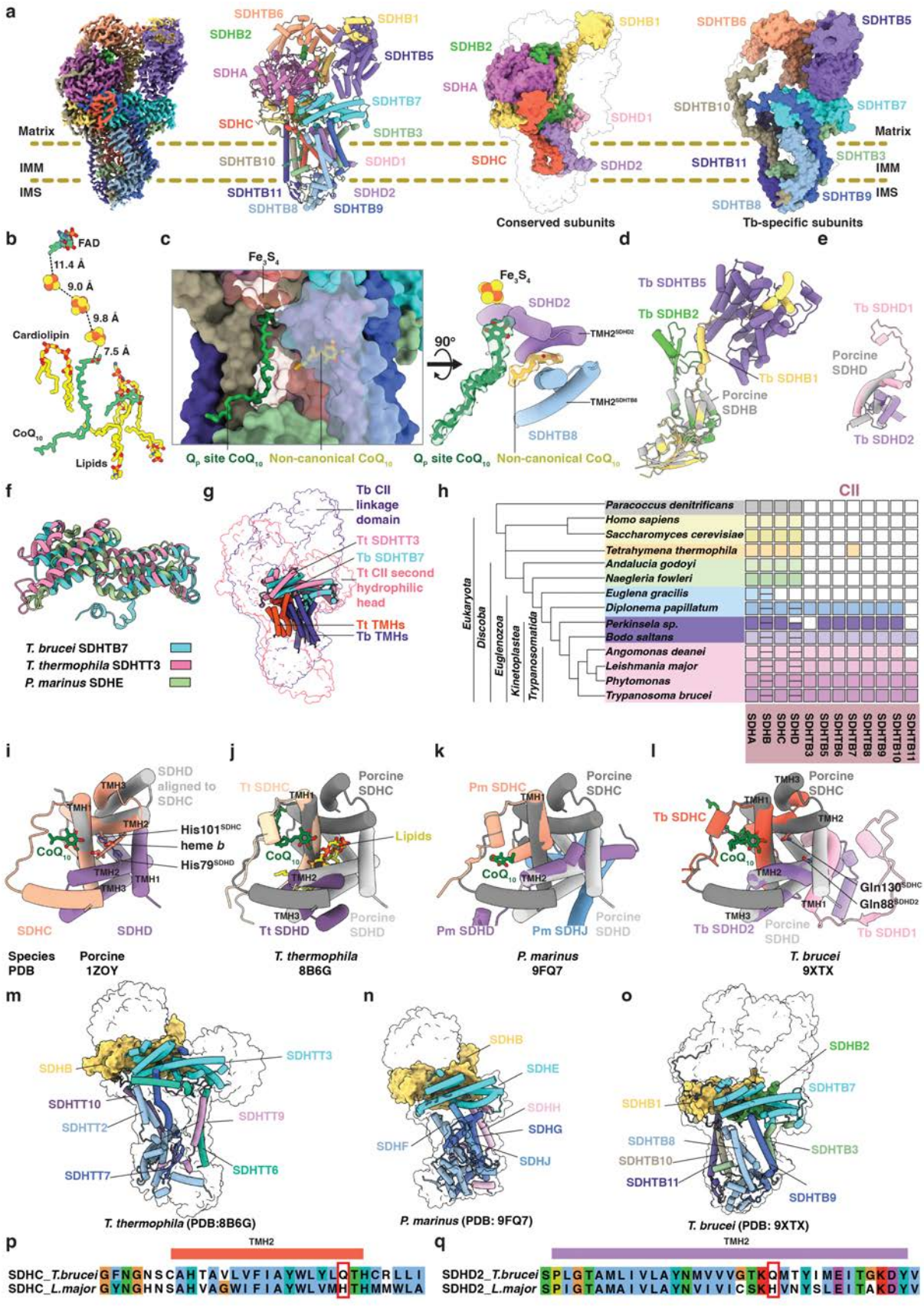

Extended Data Fig. 6 | Structural and evolutionary characterizations of *T. brucei* CII. a, From left to right: cryo-EM map, structure (cartoons) colored by individual subunits, core and conserved subunits (solid surfaces) colored individually, on top of the silhouette of complete CII. **b,** Co-factors, key lipids and CoQ_{10} in CII. FeS clusters are shown as spheres;

FAD, CoQ_{10}, and bound lipids are shown as sticks. Distances between key electron transfer co-factors are labeled. **c,** The two CoQ_{10} molecules bound in CII. Trans-membrane subunits are shown as surfaces (left) or cartoons (right) and colored individually. Some surfaces are shown in transparency to allow visualization of elements behind. The canonical site CoQ_{10} (green stick and transparent surface) is located just below the Fe_3S_4 cluster. The additional, non-canonical CoQ_{10} (yellow stick and transparent surface) bound between $TMH2^{SDHD2}$ and $TMH2^{SDHTB8}$. **d**, Structural superposition of *T. brucei* SDHB1 (yellow) and SDHB2 (green) with porcine SDHB (PDB: 1ZOY, grey), illustrating the C-terminal extension of *T. brucei* SDHB1 spanning across SDHTB5 (purple). **e**, Structural superposition of *T. brucei* SDHD1 (pink) and SDHD2 (light purple) with porcine SDHD (PDB: 1ZOY, grey). **f,** Structural superposition of *T. brucei* SDHTB7 (cyan), *T. thermophila* SDHTT3 (PDB: 8B6G, pink) and *P. marinus* SDHE (PDB: 9FQ7, green). **g,** Structural superposition of CII structures from *T. thermophila* (red silhouette) and *T. brucei* (black silhouette). The homologous SDHTT3/SDHTB7 subunits and their supporting TMHs are shown in cartoons. **h,** Evolutionary distribution showing the presence (filled squares) or absence (empty squares) of CII subunits across the same set of species as in Fig. 2f. Note that the lack of core subunits SDHC and SDHD in *E. gracilis* and the lack of accessory subunits in *A. godoyi* and *N. fowleri* are probably due to high sequence divergences rather than real absence of these subunits. **i-l,** Structures of hydrophobic core subunits, SDHC and SDHD, from *S. scrofa* (**i**, PDB: 1ZOY), *T. thermophila* (**j**, PDB: 8B6G), *P. marinus* (**k**, PDB: 9FQ7) and *T. brucei* (**l**, PDB: 9XTX), shown in cartoons. Key co-factors and residues, such as the canonical position CoQ_{10} (green), membrane-embedded heme *b* (soft orange) or lipids (yellow) occupying the same position and the heme-coordinating histidines or glutamines occupying the same position are shown as sticks. In (**i**), an additional copy of SDHD (grey) is structurally aligned to SDHC to demonstrate the pseudo C2 symmetry. In (**j-l**), classic structure of porcine SDHC and SDHD (grey) are always superposed. **m-o,** Additional hydrophobic accessory subunits with TMHs (cartoons) supporting the conserved SDHTT3/SDHE/SDHTB7 (cyan cartoons) and SDHBs (solid yellow and green surfaces), on top of silhouettes of complete CII structures from *T. thermophila* (**m**, PDB: 8B6G), *P. marinus* (**n**, PDB: 9FQ7) and *T. brucei* (**o**, PDB: 9XTX). **p,q,** Sequence alignments of the $TMH2^{SDHC}$ and $TMH2^{SDHD}$ regions from *T. brucei* and *L. major*, highlighting the positions of potential heme-coordinating histidines (red boxes).

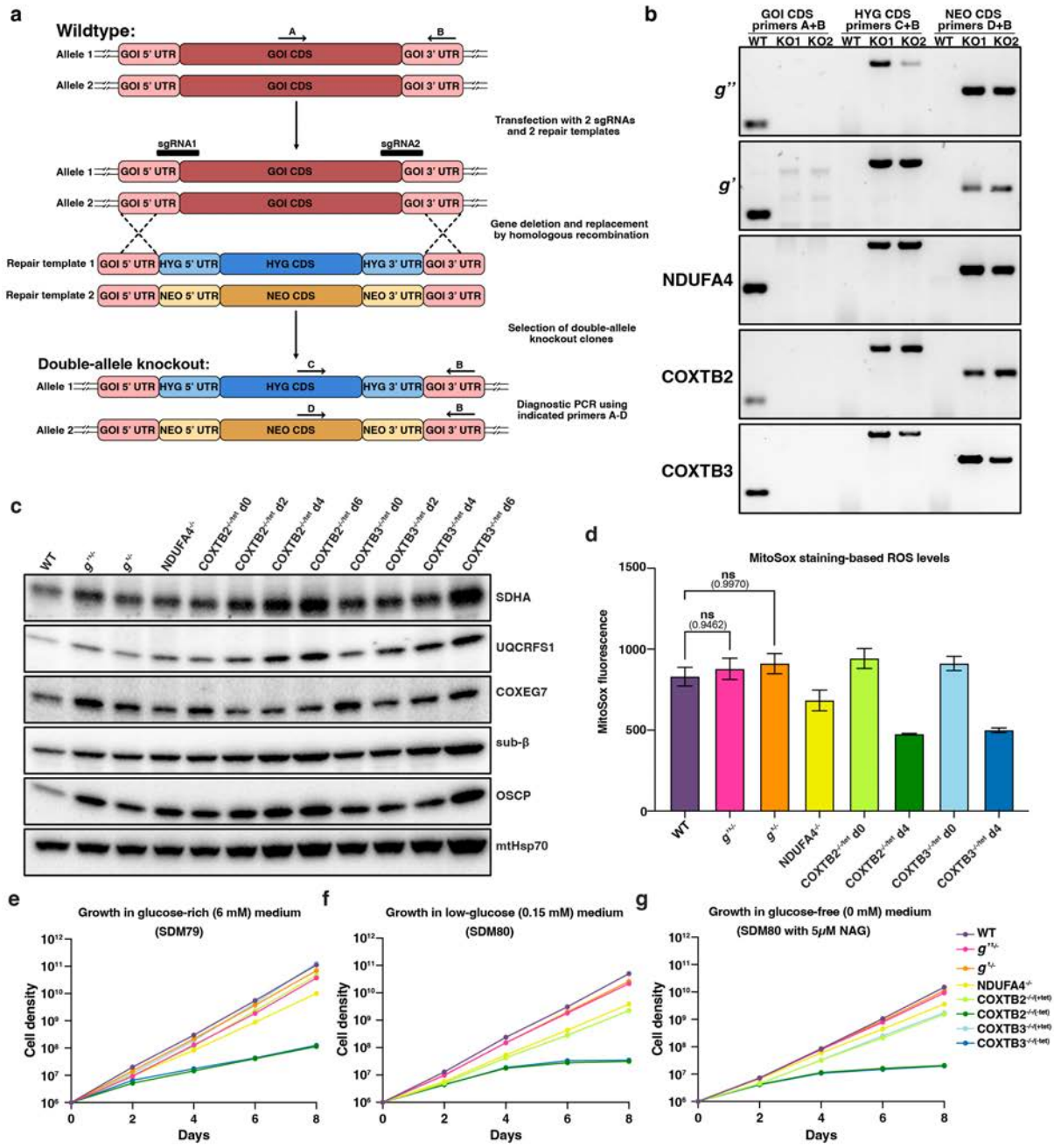

Extended Data Fig. 7 | Generation and characterization of double-knockout *T. brucei* strains. a, Schematics of the double-knockout generation strategy. **b**, Diagnostic PCRs for parallel verification of knockout clones using specific primers, with genomic DNA sourced from cells employed in growth assays and from cryopreserved stabilates. **c,** Western blot analysis of representative OXPHOS subunits resolved by SDS-PAGE from knockout strains. Antibodies used detect SDHA(CII), COXEG7 (CIV), subunit β (CV) and subunit OSCP (CV). mtHsp70 is used as an internal loading control. **d,** Measurement of ROS productions by the WT and knockout strains. **e-g,** Growth curves of WT and knockout strains in glucose-rich (**e**), low-glucose (**f**) and glucose-free media (**g**). The ROS levels in (**d**) are represented as mean ± SEM (n = 3 biologically independent replicates).

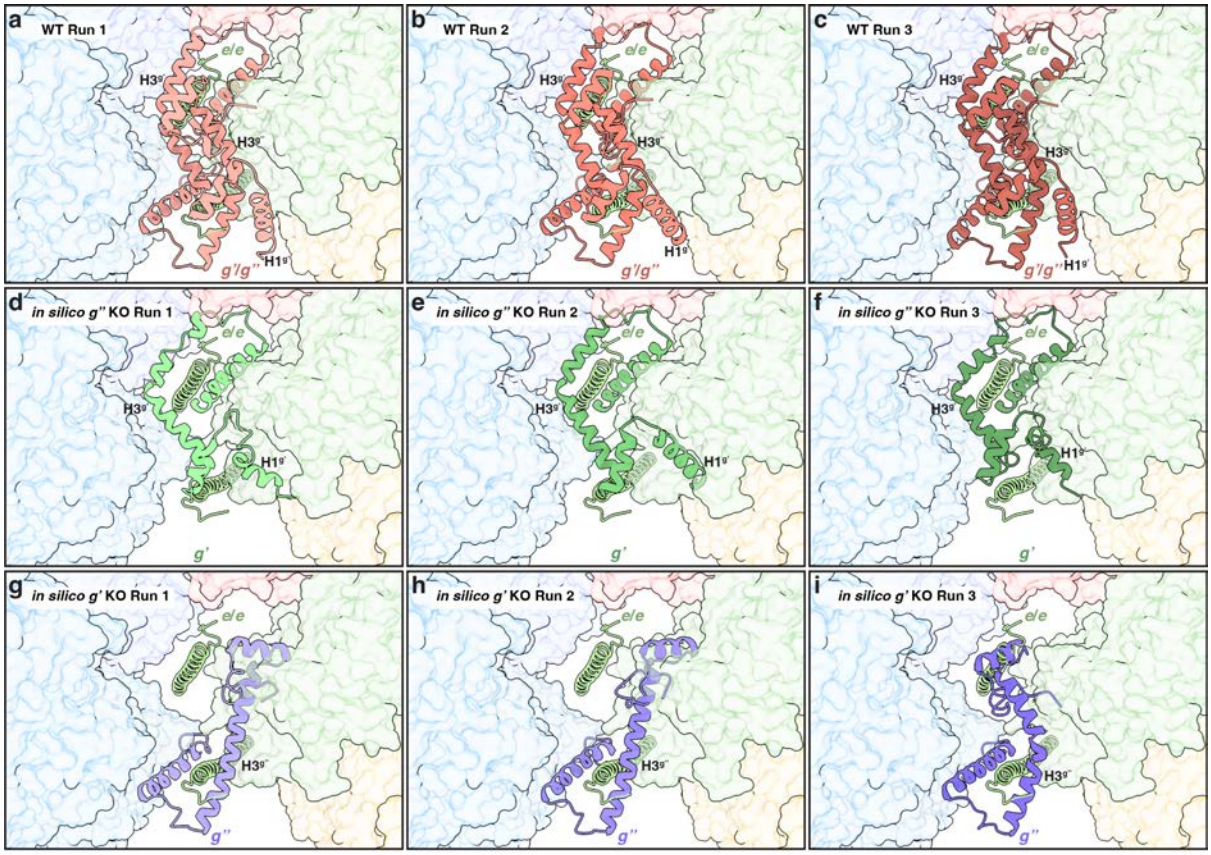

Extended Data Fig. 8 | End-of-run structures of the MD simulations of WT and *in silico g'/g'' KO*. a-i, End-of-run structures in the MD simulations of WT CIICIV$_2$CV (**a-c**), *in silico g''* KO (**d-f**) and *in silico g'* KO (**g-i**). Three replicates are shown for each of the starting conditions. Note that while the WT *g'/g''* module stay more or less the same as the starting cryo-EM structure of CIICIV$_2$CV, H1$^{g'}$ displays different levels of distortion in the three replicates of *in silico g''* KO and H3$^{g''}$, originally curved, displays different levels of straightening up in the three replicates of *in silico g'* KO.

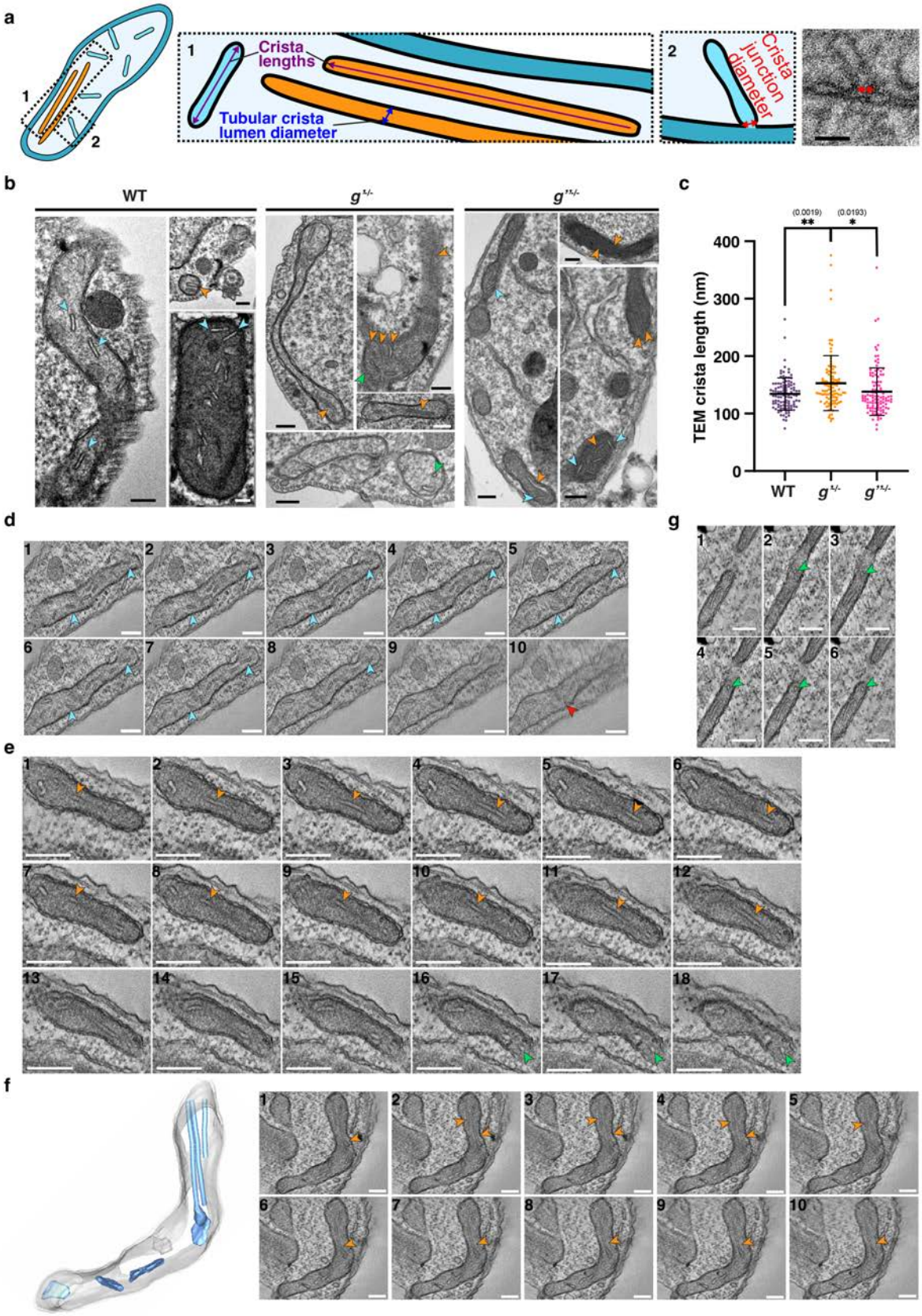

Extended Data Fig. 9 | Mitochondrial cristae morphology is altered in *g'* and *g''* KO cell lines. a, Schematic illustration of a mitochondrion, with boxed areas (dashed rectangles) enlarged in the insets to the right. They illustrate the measured lengths (purple double arrows) of discoidal (cyan) and tubular cristae (orange), the lumen diameters (blue double arrows) of

tubular cristae and crista junction diameter (red double arrows). The rightmost panel is an image from an electron tomogram in which crista junction diameter was measured. **b,** Exemplar TEM images of thin sections from strains indicated at top. **c,** Quantification of cristae length in WT and *g'*$^{-/-}$/*g''*$^{-/-}$ cells. Bar and whiskers show mean and standard deviation, respectively. **d,e,** The subsets of tilt sections from the 3D reconstructions of the WT cell from Fig. 3d (**d**) and the *g'*$^{-/-}$ cell from Fig. 3e (**e**). **f,g,** Two additional subsets of tilt sections from the *g'*$^{-/-}$ cells. 3D electron tomogram is reconstructed for one of them (**f**). (**g**) demonstrates a series of transverse planes of a tubular crista (green arrowheads). Scale bars, 200 nm (except **f**, 50 nm). Blue arrowheads, WT cristae; orange arrowheads, frontal plane of tubular cristae; green arrowheads, transverse plane of tubular crista; red arrowhead, crista junction. Tilt series are shown every 5 (**f**), 10 (**d**, **e**) or 20 (**g**) sections.

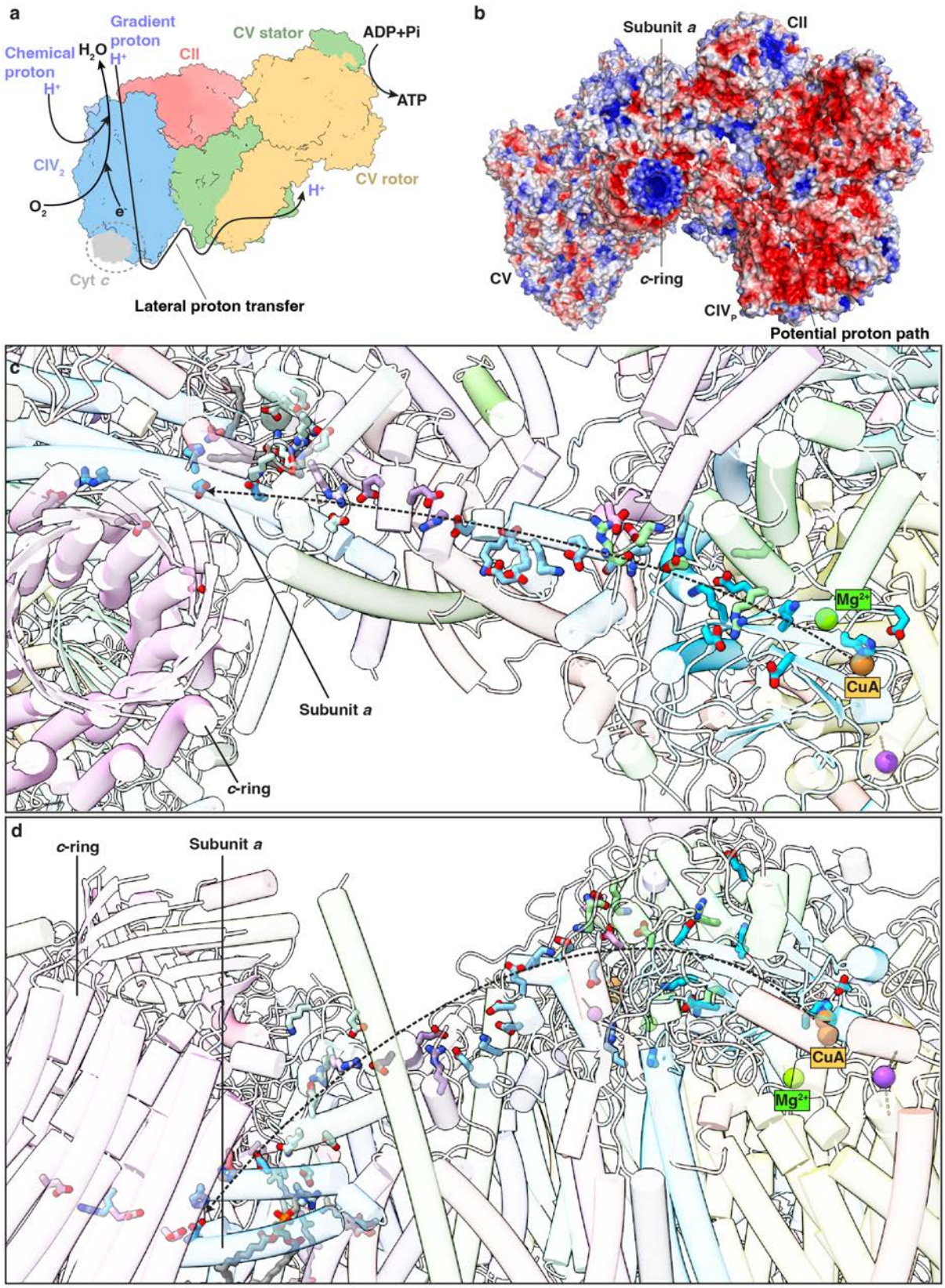

Extended Data Fig. 10 | Lateral proton transfer and the proposed surface proton path on CIICIV$_2$CV. a, A schematic of lateral proton transfer. The gradient protons, pumped from the matrix to the IMS side by CIV$_P$, travel along the protein surface as depicted in (**b**) and return to the matrix side by powering the ATP synthesis of CV. The approximate binding position of cytochrome *c* (grey) is inferred based on the structure PDB: 5IY5. **b,** Surface

electrostatic potential of the CIICIV$_2$CV supercomplex, viewed from the IMS side. Positions of individual complexes, CV subunit *a* and the *c*-ring are labeled. Note that a continuous path (dashed arrow) formed by negatively charged surface can be identified, leading from the IMS opening of CIV's proton exit route to the IMS half-channel of CV. **c,d,** Zoom-in views, from the matrix (**c**) or parallel to the membrane (**d**), showing the residues capable of proton transfer lining the proposed surface proton path in (**b**). Key co-factors, such as the Cu_A, and subunits, such as subunit *a* and *c*-ring, defining the start and end of such path are labeled.

Title: A Supercomplex Incorporating Both Electron Transport Chain and ATP Synthase

Authors: Yiqi Hu[1]†, Jonathan Wong[2,3]†, Erik Endres[4]†, Benz Corinna[2]†, Cristina Pecorilla[4]†, Kun Huang[5,6]†, Tomáš Bílý[2,3], Hongtao Tian[1], Menglu Teng[7], Fangzhu Han[1], Mengchen Wu[1], Naiwen Zhang[8,9], Qijun Chen[8,9], Jiancang Zhou[10], Dehua Lai[7], Alena Zíková[2,3], Martijn A. Huynen[11]*, Hassan Hashimi[2,3]*, Vivek Sharma[4,12]*, Ondřej Gahura[2]*, Alexey Amunts[5,6]*, Long Zhou[1]*

Affiliations:

[1]Department of Biophysics and Department of Critical Care Medicine of Sir Run Run Shaw Hospital, Zhejiang University School of Medicine, Hangzhou 310058, China
[2]Institute of Parasitology, Biology Centre, Czech Academy of Sciences, 37005 České Budějovice, Czech Republic
[3]Faculty of Science, University of South Bohemia, České Budějovice, Czech Republic
[4]Department of Physics, University of Helsinki, Helsinki 00014, Finland
[5]University of Münster, Schlossplatz 8, 48143, Münster, Germany
[6]Institute of Bio-Architecture and Bio-Interactions, Shenzhen Medical Academy of Research and Translation, Shenzhen, Guangdong 518107, China
[7]MOE Key Laboratory of Gene Function and Regulation, State Key Laboratory of Biocontrol and Guangdong Provincial Key Laboratory of Aquatic Economic Animals, School of Life Sciences, Sun Yat-Sen University, Guangzhou 510275, P. R. China
[8]Key Laboratory of Livestock Infectious Diseases, Ministry of Education, Key Laboratory of Zoonosis, College of Animal Science and Veterinary Medicine, Shenyang Agricultural University, Shenyang, China
[9]The Research Unit for Pathogenic Mechanisms of Zoonotic Parasites, Chinese Academy of Medical Sciences, Shenyang, China
[10]Department of Critical Care Medicine of Sir Run Run Shaw Hospital, Zhejiang University School of Medicine, Hangzhou, Zhejiang 310058, China
[11]Department of Medical BioSciences, Radboud University Medical Center, Nijmegen, The Netherlands
[12]HiLIFE Institute of Biotechnology, University of Helsinki, Helsinki 00014, Finland

*Corresponding author. Email: Martijn.Huijnen@radboudumc.nl, hassan@paru.cas.cz, vivek.sharma@helsinki.fi, gahura@paru.cas.cz, alexey.amunts@gmail.com, longzhou@zju.edu.cn
†These authors contributed equally to this work

Supplementary Information contents:

Supplementary Discussion

T. brucei ETC structures confirm kinetoplastids' mitochondrial transcript editing features

Our $CIII_2$, CIV_2 and CV structures confirm known gene fragmentation and transcript editing/splicing features of the *T. brucei* mitochondrial genomes[70]. For example, maxicircle encoded COXIII and subunit *a* (ATP6) transcripts are pan-edited throughout their sequences by uridine insertion/deletion[71–73], while COXII and COB transcripts are only edited at specific positions to create either a downstream frameshift or an upstream start codon[74–76]. The obtained cryo-EM density maps agree with the translations of these edited transcripts (Extended Data Fig. 4e,f).

Specifically, the 20-residue N-terminal helix of COB, introduced by a new start codon originated from uridine additions, has clear density in our $CIII_2$ structure (Extended Data Fig. 5d). They form part of the quinone headgroup binding cavity of the *T. brucei* Q_N site, where clear ubiquinone/coenzyme Q_{10} (CoQ_{10}) density can be observed (Extended Data Fig. 5a). Superposition of COB structures demonstrates that *T. brucei* $CIII_2$ adopts a canonical conformation in this region as most other species (Extended Data Fig. 5b). Only that in *E. gracilis* this NT helix has rotated away from the Q_N site, effectively weakening CoQ_{10} binding here as reflected by lack of ligand in its $CIII_2$ structure of comparable resolution[6] (Extended Data Fig. 5b). Sequence alignment of COB reveals the existence of an *E. gracilis*-specific double tyrosine motif here (Tyr19/22), which if not rotated, would produce a Q_N environment too narrow for quinone headgroup to enter (Extended Data Fig. 5b,c). Therefore, euglenids and kinetoplastids have evolved different strategies to deal with structural variations at the COB NT. The early-branching euglenids could not edit transcript and had to tolerate the appearance of double tyrosine motif by structural rearrangement[77]. On the other hand, parasitic kinetoplastids accumulate mutations more efficiently in their maxicircle encoded subunits due to selective pressure relaxation in the anaerobic phase of life cycle and have gained uridine insertion/deletion capabilities as remedies[70]. Canonical Q_N site structure can thus be maintained, thanks to the combinatory effects of both genetic drift in the

bloodstream stage (such as for Tb_Leu19^{COB}) and natural selection of the transcript editing in the procyclic stage (such as for Tb_Leu16^{COB})[76].

Structural details of T. brucei's divergent CII, apart from its linkage domain

The structure of *T. brucei* CII reveals the splitting of its core subunits SDHB and SDHD (Extended Data Fig. 6d,e). Splitting of core OXPHOS subunits, mostly the hydrophobic ones of CI, CIV and CV, has been repeatedly reported for a range of eukaryotic clades[3–6,18,73], so that genes encoding the split, less hydrophobic fragments can be relocated to the nuclear genome to keep the mitochondrial genome streamlined[78]. Splitting of CII subunits, however, has not been structurally visualized until the current study. It is noteworthy that such trans-membrane subunit splitting makes sequence-based structure prediction of the resultant fragments less reliable. Therefore, the possibility cannot be ruled out that the aforementioned dissimilarity between the Alphafold predicted structures of *T. brucei* mitochondrial transcripts CR3/CR4 and structures of canonical ND4L/ND6 is because the former are the mitochondrial remnants after splitting of the latter (Supplementary Fig. 2g-i).

A total of eight lineage-specific accessory subunits (prefixed by 'SDHTB') are identified in *T. brucei* CII (Extended Data Fig. 6a). In a broader perspective, the membrane-embedded regions of known eukaryotic CII structures from mammals[17,79], *T. thermophila*[5,18], *Perkinsus. marinus*[80] and the currently studied *T. brucei* display high diversity in terms of the numbers and positions of their TMHs. The classic, mammalian CII contains two hydrophobic core subunits, SDHC and SDHD (Extended Data Fig. 6i). Each with three TMHs (TMH1-3), they display a pseudo-2-fold symmetry and embrace a b-type heme in the middle. The heme iron is axially coordinated by two histidine residues, each on the TMH2 of subunit SDHC or SDHD. In this way, a tetra-TMH hydrophobic core with heme *b* surrounded in the center, is formed by the N-terminal TMH1 and TMH2 of subunits SDHC and SDHD, while the two C-terminal TMH3 run more or less parallel to respective heme-iron coordinating TMH2. Such structural motif however, is not always conserved among CIIs across different eukaryotic

clades. Importantly, the matrix ends of TMH1^{SDHC} and TMH2^{SDHD} form CII's CoQ_{10} redox site where CoQ_{10} receives electrons from the terminal Fe_3S_4 cluster, thereby representing the evolutionarily most conserved part of the tetra-TMH core (Extended Data Fig. 6i). In our *T. brucei* CII structure, clear CoQ_{10} densities can be observed, not only at this canonical site, but also at a non-canonical site in-between CII's TMH2^{SDHD2} (corresponds to canonical TMH3^{SDHD}) and TMH2^{SDHTB8}, likely representing a local energy minimum along the route of CoQ_{10} entering and exiting CII (Extended Data Fig. 6b,c). Similar CoQ binding sites *en route* to the redox reaction centers are also known in CI and $CIII_2$[5,81].

In accordance with the above, *T. thermophila* CII has lost TMH2^{SDHC}, TMH3^{SDHC} and TMH1^{SDHD}, reserving only TMH1^{SDHC}, TMH3^{SDHD} and the matrix half of TMH2^{SDHD} (Extended Data Fig. 6j). Since both heme iron-coordinating histidines are lost in the process, no membrane-embedded heme is found with the original space occupied by lipids, indicating that this heme is not absolutely required for electron transport in CII[79]. Similar pattern is observed for the SDHC and SDHD of *P. marinus*, also belonging to the clade Alveolata, only that a full TMH2^{SDHD}, interrupted by a kink in the middle, is present (Extended Data Fig. 6k). The single TMH of the accessory subunit SDHJ spatially overlaps with *T. thermophila* TMH3^{SDHD}, which is however quite displaced compared to the TMH3^{SDHD} in the classic, mammalian SDHD structure. Like *T. thermophila*, *P. marinus* has also lost the CII heme, suggesting that this is common trait of alveolates. On the other hand, unlike alveolates, *T. brucei* CII has more or less retained the tetra-TMH core in its hydrophobic region, only that the SDHD1 TMH is severely displaced so that the C2 symmetry is broken (Extended Data Fig. 6l). But *T. brucei* CII still loses the CII heme due to His-to-Gln mutations in both TMH2^{SDHC} and TMH2^{SDHD}. It is worth mentioning that this double His^{TMH2} motif is conserved in CII of the closely related *Leishmania tarentolae* implicating the presence of membrane-embedded heme *b* (Extended Data Fig. 6p,q). In general, since the hydrophobic subunits of CII are encoded by the nuclear genome, reduction of their TMHs cannot be attributed to the evolutionary pressure of mitochondrial genome streamlining. The above

observed phenomenon thereby is more likely linked to the evolutionary process of CII's heme *b* which remains elusive.

Moreover, despite the reduction of core subunit TMHs, a number of new TMHs from lineage-specific accessory subunits have emerged in these non-mammalian eukaryotic species, but without much of apparent structural homology regarding their positions relative to SDHC and SDHD (Extended Data Fig. 6m-o). For example, different organizations of accessory TMHs are developed to support the horizontal subunit SDHTT3/SDHE/SDHTB7, which is the only accessory subunit with clear structural homology across clades. For *T. thermophila*, subunits SDHTT2, SDHTT7 and the horizontal helices of SDHTT6 form a frame to support SDHTT3, while a separate TMH group of SDHTT9 and SDHTT6 support the second hydrophilic head, also linked to the conserved SDHTT3 (Extended Data Fig. 6m). For *P. marinus* and *T. brucei*, such role of supporting SDHTT3 orthologues, SDHE and SDHTB7, is fulfilled by TMHs from SDHF, SDHG, SDHH, SDHJ and SDHTB3, SDHTB8, SDHTB9, respectively (Extended Data Fig. 6n,o). It is noteworthy that SDHTT2, SDHF and SDHTB8 are all double TMH subunits occupying roughly similar positions in respective CIIs. However, sequence-based homology search failed to identify them as orthologues (Extended Data Fig. 6h). A second function of the accessory TMHs is to support the N-terminal α/β domain of hydrophilic core subunit SDHB, which overhang unsupported by the hydrophobic subunits SDHC and SDHD in mammalian CII[17,79]. SDHTT10 of *T. thermophila* and SDHTB10 and SDHTB11 of *T. brucei* serve such function, likely to increase the stabilities of augmented CIIs, especially after the split of SDHB in *T. brucei* (Extended Data Fig. 6d,e,m,o). Taken together, although very limited sequence and structural homology is observed among accessory, trans-membrane subunits of CII apart from the SDHTT3/SDHE/SDHTB7 mentioned in the Main Text (Extended Data Fig. 6f), they likely represent different ways developed by different eukaryotic clades to stabilize the specialized structural elements of their CIIs, such as the SDHTT3/SDHE/SDHTB7 subunits, the split of

SDHB and the second hydrophilic head, so that their CIIs can better assemble into respective CII-containing supercomplexes.

Structural variations among the three g subunits help to serve different assembly purposes

A closer look at the alignment of *g*/*g'*/*g''* sequences from a range of kinetoplastids reveals several key residues that are conserved among sequences belonging to a specific *g*, *g'* or *g''* subunit, but are substituted by residues with reversed charge or polarity across different *g* subunits (Extended Data Fig. 3c). For example, in subunit *g* the conserved salt bridge network Ser57^{g}-Arg60^{g}-Glu64^{g} maintains dimerization in the (*e*/*g*)$_2$ module in CV$_2$ by locking the two IMM-parallel helices^{g} next to each other (Fig. 2b and Extended Data Fig. 3c). However, in subunit *g''*, negative-to-neutral substitution of Glu64^{g} by Leu51$^{g''}$ allows adjacent positive-to-negative charge reversal of Arg60^{g} by Glu49$^{g'}$/Asp47$^{g''}$, which further dictates the removal of another nearby negative charge by Glu64^{g}-to-Tyr53$^{g'}$ substitution (Fig. 2b and Extended Data Fig. 3c). Although such 'dominos style' mutations disrupt the salt bridge network Ser57^{g}-Arg60^{g}-Glu64^{g} and abolish *g'*/*g''* subunits' abilities to self-dimerize or hetero-dimerize with subunit *g*, they introduce a new framework for *g'* and *g''* to hetero-dimerize with each other and form the interlocked *e*/*g'*/*e*/*g''* structure in *T. brucei* CIICIV$_2$CV. For example, Glu49$^{g'}$, substituting Arg60^{g}, contributes to *g'*-*g''* hetero-dimerization by interacting with the *g''*-specific N-terminal loop, which is kept in a favorable position by Asp47$^{g''}$, again a substitution of Arg60^{g} on *g''*. Similarly, Tyr53$^{g'}$ substituting Glu64^{g} forms π-π stacking with Phe26$^{g''}$ and stabilizes the *e*/*g'*/*e*/*g''* apparatus from the end of the lipid-filled central gap (Fig. 2b).

The reasons that kinetoplastids have to evolve two additional *g* subunits with substantial alterations to get the ETC-CV supercomplex assembled are multifaceted. First of all, while homodimeric (*e*/*g*)$_2$ can be used to assemble CV$_2$, different structures and sequences are needed to respectively bind CIV$_P$ and CV (Fig. 2a). Subunit *g'* simultaneously interacts with CII, CIV$_2$ and CV via electrostatic/polar contacts, a function that cannot be fulfilled by

202 subunit *g* or *g''*, while subunit *g''* interacts with CIV_2 through hydrophobic interactions
203 maintained via bridging lipid molecules (Fig. 2c). More importantly, the newly established
204 *g'*-*g''* heterodimeric interface introduces a shallower membrane bending compared to *g*-*g*
205 homodimer (36° vs 48°), which agrees with $CIICIV_2CV$'s cristae position with less
206 membrane curvature than that introduced by CV_2 (Extended Data Fig. 3d).
207

Supplementary Figures

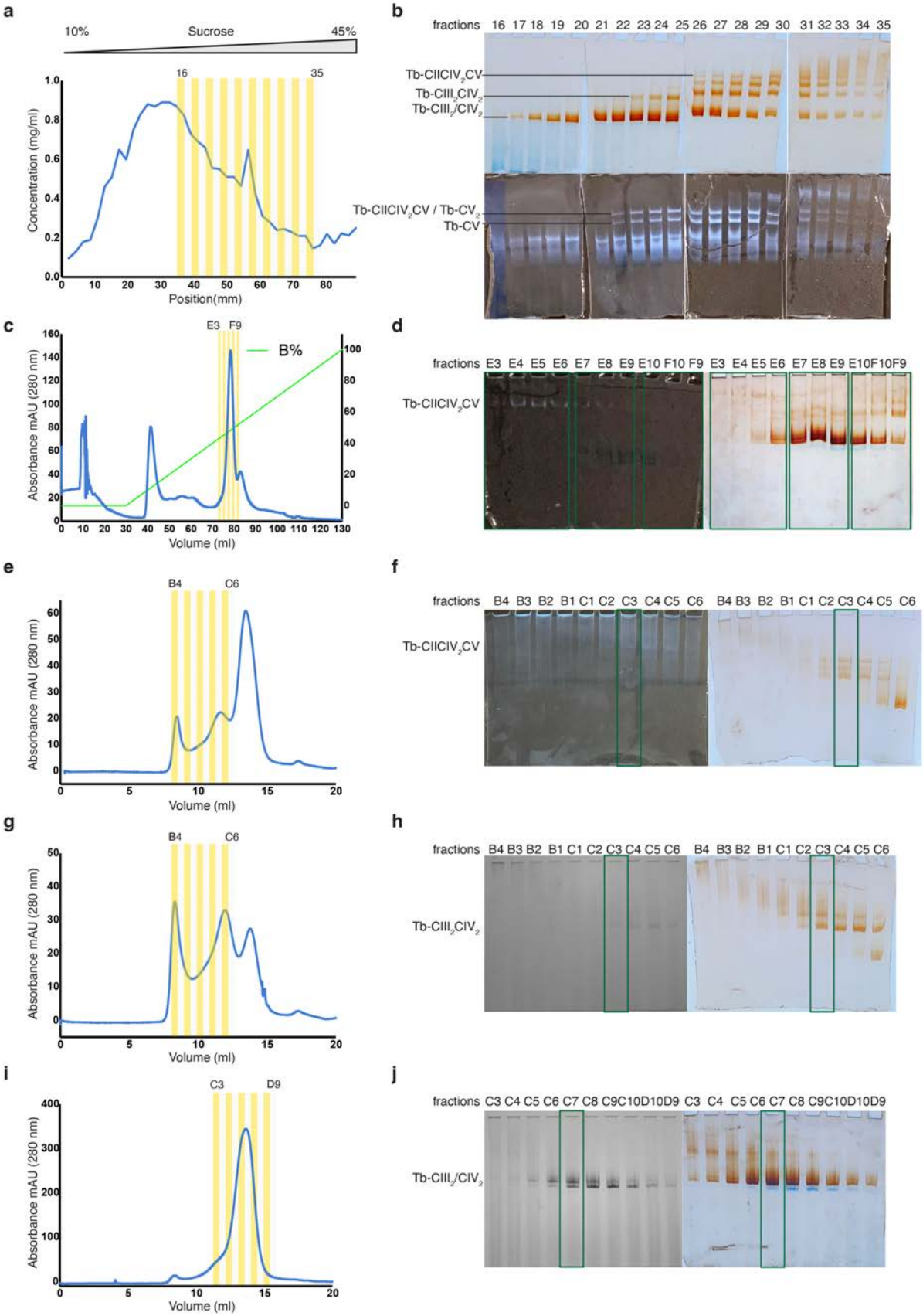

Supplementary Fig. 1 | Purification of ETC complexes, supercomplex and ETC-CV supercomplex from procyclic *T. brucei*. **a**,**b,** Sucrose gradient ultracentrifugation profile of

280 nm absorbance (**a**) and the corresponding BN-PAGE (**b**) of digitonin-extracted *T. brucei* mitochondrial complexes and supercomplexes. All the shown fractions are pooled and used for subsequent anion-exchange chromatography. **c,d,** Q-Sepharose HP anion-exchange chromatogram (**c**) and the corresponding BN-PAGE (**d**). The three groups of fractions separately pooled, concentrated and used for subsequent SEC chromatography are indicated by green boxes. **e,f,** Superose 6 Increase 10/300 GL size-exclusion chromatogram (**e**) and the corresponding BN-PAGE (**f**), using the CIICIV$_2$CV-containing fractions E3-E6 from (**d**). The fraction directly used for cryo-EM grid preparations is indicated by green box. **g,h,** The same as in (**e**) and (**f**) but using the fractions E10-F9 from (**d**) containing higher MW CIV species. **i,j,** The same as in (**e**) and (**f**) but using the fractions E7-E9 from (**d**) containing lower MW CIV species. BN-PAGE gels in panels (**b**), (**d**) and (**f**) are stained by CV (white bands) and CIV (dark orange bands) activities. BN-PAGE gels in panels (**h**) and (**j**) are stained by coomassie blue (grey scale) and CIV activity (dark orange bands).

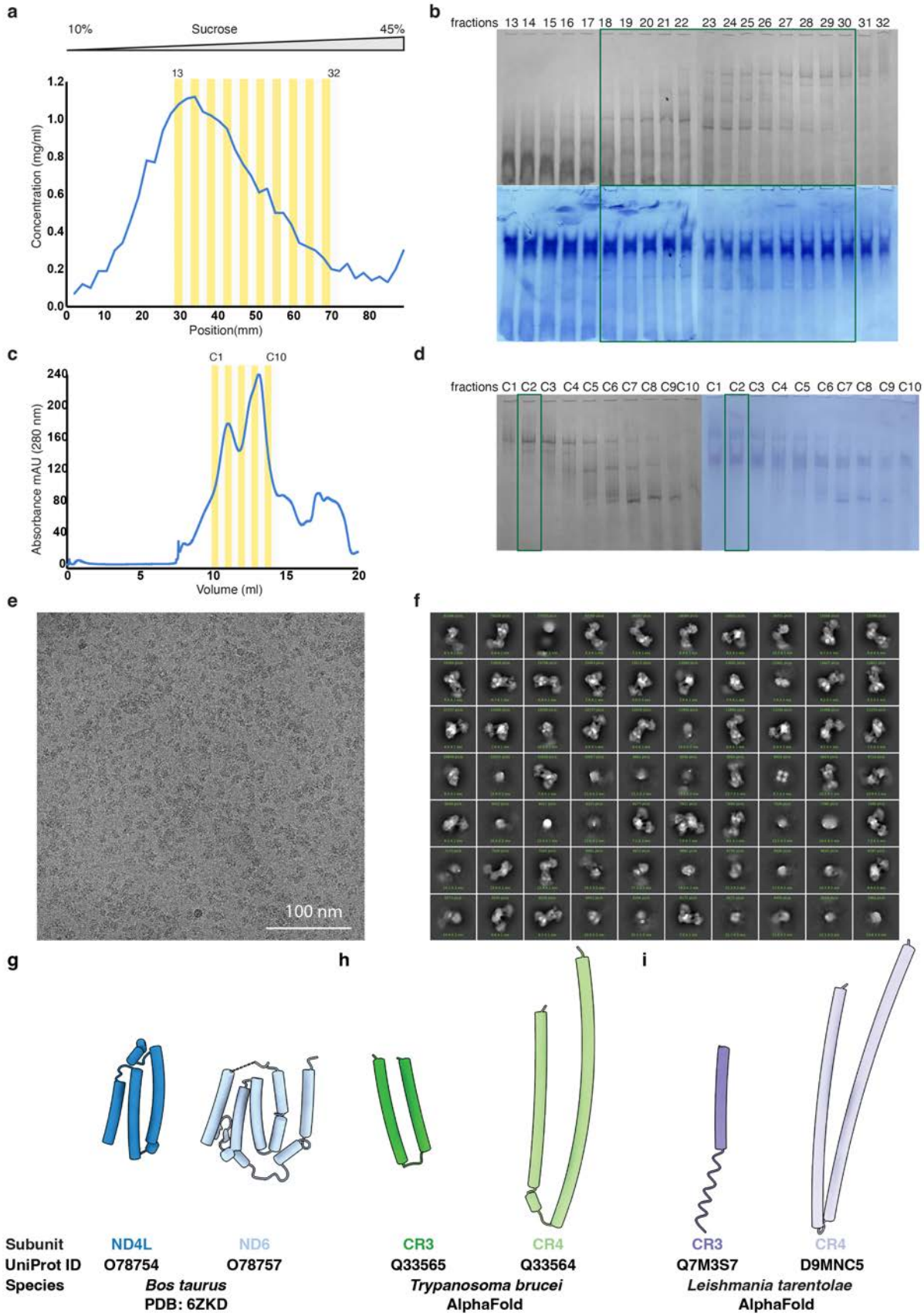

Supplementary Fig. 2 | Biochemical and structural evidences of the absence of canonical CI in procyclic *T. brucei* mitochondria. a,b, Sucrose gradient ultracentrifugation profile of 280 nm absorbance (**a**) and the corresponding BN-PAGE (**b**) of digitonin-extracted *T. brucei* mitochondrial complexes and supercomplexes. The fractions pooled for subsequent SEC

chromatography are designated by green boxes. **c,d,** Superose 6 Increase 10/300 GL size-exclusion chromatogram (**c**) and the corresponding BN-PAGE (**d**). The fraction directly used for cryo-EM grid preparation is marked by a green box. All BN-PAGE gels were stained by coomassie blue (grey scale; **b**: top panel, **d**: left panel) and CI/NADH dehydrogenase activity (blue-purple bands; **b**: bottom panel, **d**: right panel). **e**, Representative cryo-EM micrograph from a dataset of 5,750 movies collected on a 300 kV Titan Krios microscope equipped with a Falcon IVi camera, using fraction C2 in (**d**) with prominent NADH dehydrogenase activity. **f**, Reference-free 2D classification of 1,998,743 initially picked particles. All sensible 2D class averages show characteristic features of CV_2 or $CIICIV_2CV$, but not the shape of canonical CI. **g-i,** Structural comparisons of mammalian CI core subunits ND4L and ND6 (**g**, dark and light blue, PDB: 6ZKD) with AlphaFold predictions of *T. brucei* CR3 and CR4 (**h**, dark and light green) and *L. tarentolae* CR3 and CR4 (**i**, dark and light purple). UniProt identifiers of each of the subunits involved are labeled.

Supplementary Tables

Supplementary Table 1 | Cryo-EM data collection, image processing and model validation of CIICIV$_2$CV

	CIICIV$_2$CV$_{mem}$ (EMDB-67255) (PDB 9XTY)		CIICIV$_2$CV$_{state1}$ (EMDB-67252) (PDB 9XTV)		CIICIV$_2$CV$_{state2}$ (EMDB-67253) (PDB 9XTW)		CIICIV$_2$CV$_{state3}$ (EMDB-67254) (PDB 9XTX)	
Magnification	105,000							
Voltage (kV)	300							
Electron exposure (e$^-$/Å^2)	52.00							
Defocus range (μm)	-0.8 to -2.0							
Pixel size (Å)	1.20							
Symmetry imposed	C1							
Micrographs No.	13,347							
Initial particle No.	5,950,660							
Final particle No.	579,050		33,147		43,117		47,450	
Map resolutions (Å)	CII	2.83	CII	3.04	CII	3.01	CII	3.01
FSC threshold 0.143	CIV$_2$	2.71	CIV$_2$	2.93	CIV$_2$	2.88	CIV$_2$	2.86
	CV_F$_o$_stator	2.80	CV_F$_o$_stator	3.01	CV_F$_o$_stator	2.99	CV_F$_o$_stator	2.90
			CV_α$_3$β$_3$γ$_{top}$	3.51	CV_α$_3$β$_3$γ$_{top}$	3.41	CV_α$_3$β$_3$γ$_{top}$	3.40
			CV_*c*-ring+γ$_{bottom}$	3.61	CV_*c*-ring+γ$_{bottom}$	3.73	CV_*c*-ring+γ$_{bottom}$	3.43
			CV_PS	3.94	CV_PS	3.92	CV_PS	3.69
Initial models used	8APA		8APA		8APF		8APK	
Model resolution (Å)	2.9		3.3		3.4		3.3	
FSC threshold 0.5								
Map sharpening *B* factor (Å^2)	CII	119.5	CII	44.8	CII	48.2	CII	49.3
	CIV$_2$	116.1	CIV$_2$	42.6	CIV$_2$	44.7	CIV$_2$	47.0
	CV_F$_o$_stator	116.7	CV_F$_o$_stator	41.6	CV_F$_o$_stator	44.7	CV_F$_o$_stator	46.4
			CV_α$_3$β$_3$γ$_{top}$	34.9	CV_α$_3$β$_3$γ$_{top}$	40.7	CV_α$_3$β$_3$γ$_{top}$	41.3
			CV_*c*-ring+γ$_{bottom}$	47.3	CV_*c*-ring+γ$_{bottom}$	54.3	CV_*c*-ring+γ$_{bottom}$	48.1
			CV_PS	65.1	CV_PS	61.9	CV_PS	52.9
Model composition								
Non-hydrogen atoms	98004		140614		140738		140881	
Protein residues	11377		16943		16962		16980	
Ligands	89		89		89		89	
B factors (Å^2)								
Protein	62.53		96.51		104.58		93.90	
Ligand	42.68		42.68		42.19		42.68	
R.m.s. deviations								
Bond lengths (Å)	0.010		0.009		0.009		0.008	
Bond angles (°)	0.709		0.653		0.666		0.626	
Validation								
MolProbity score	1.28		1.58		1.62		1.49	
Clashscore	4.93		7.00		7.52		6.85	
Poor rotamers (%)	0.65		0.61		0.79		0.52	
Ramachandran plot								
Favored (%)	97.90		96.86		96.67		97.44	
Allowed (%)	2.10		3.14		3.33		2.56	
Disallowed (%)	0.00		0.00		0.00		0.00	

Supplementary Table 2 | Cryo-EM data collection, image processing and model validation of $CIII_2CIV_2$, $CIII_2$ and CIV_2

	$CIII_2CIV_2$ (EMDB-67256) (PDB 9XTZ)		$CIII_2$ (EMDB-67189) (PDB 9XT1)	CIV_2 (EMDB-67192) (PDB 9XT9)
Magnification			105,000	
Voltage (kV)			300	
Electron exposure (e–/Å^2)			52.00	
Defocus range (μm)			-0.8 to -2.0	
Pixel size (Å)			1.20	
Symmetry imposed			C1	
Micrographs No.		12,510		1,511
Initial particle No.		6,343,816		762,590
Final particle No.		21,346	293,996	82,850
Map resolutions (Å)	$CIII_2$	3.14	2.65	3.01
FSC threshold 0.143	CIV_2	3.23		
Initial models used			8IUF	8IUF
Model resolution (Å)	3.5		2.8	3.2
FSC threshold 0.5				
Map sharpening *B* factor (Å^2)	$CIII_2$	23.5	115.0	106.9
	CIV_2	27.6		
Model composition				
Non-hydrogen atoms	99696		43782	55914
Protein residues	11562		5100	6462
Ligands	130		73	57
B factors (Å^2)				
Protein	166.83		36.88	47.83
Ligand	132.29		42.58	29.74
R.m.s. deviations				
Bond lengths (Å)	0.007		0.009	0.005
Bond angles (°)	0.629		0.603	0.704
Validation				
MolProbity score	1.58		1.45	1.44
Clashscore	7.89		5.90	6.60
Poor rotamers (%)	0.65		0.59	0.81
Ramachandran plot				
Favored (%)	97.19		97.32	97.67
Allowed (%)	2.81		2.68	2.33
Disallowed (%)	0.00		0.00	0.00

Supplementary Table 3 | Model summary of *T. brucei* supercomplex CIICIV$_2$CV (using the CV state 3 model as an example)

Subunit Name	UniProt /Gene ID	Annotation	Chain ID	Total residues	Residues built	% built	TMH	Ligands	Lipids
CII									
SDHA	Q57TV5	Succinate dehydrogenase [ubiquinone] flavoprotein subunit, mitochondrial, SDH1	SA	609	12-609	98.19%	0	1 × FAD	
SDHB1	Q57YX5	succinate dehydrogenase iron-sulfur subunit, SDH2N	B1	242	25-169/182-237	83.06%	0	1 × Fe_2S_2	
SDHB2	Q38EW9	succinate dehydrogenase iron-sulfur subunit, putative，SDH2C	B2	188	2-179	94.68%	0	1 × Fe_3S_4 1 × Fe4S4	
SDHC	Q57WH4	Uncharacterized protein	SC	151	27-149	81.46%	3	1 × CoQ_{10}	1 × PC
SDHD1	Q57TS4	Succinate dehydrogenase subunit 11, SDH11	D1	88	21-88	77.27%	1		
SDHD2	Q389G4	succinate dehydrogenase cytochrome B subunit, SDH4	D2	129	42-129	68.22%	2		1 × PC 2 × PE
SDHTB3	Q586B1	succinate dehydrogenase subunit 3, SDH3	SE	104	2-104	99.04%	1		
SDHTB5	Q57XJ6	succinate dehydrogenase subunit 5, SDH5	SF	483	14-192/202-337/348-478	92.34%	0		
SDHTB6	Q57X18	succinate dehydrogenase subunit 6, SDH6	SG	333	35-102/115-333	86.19%	0		
SDHTB7	Q584Q7	succinate dehydrogenase subunit 7, SDH7	SH	240	27-240	89.17%	0		
SDHTB8	Q586R6	Succinate dehydrogenase subunit 8, SDH8	SI	151	1-139	92.05%	2	1 × CoQ_{10}	
SDHTB9	Q38BU1	Succinate dehydrogenase subunit 9, SDH9	SJ	135	12-135	91.85%	1		
SDHTB10	Q57VW2	Succinate dehydrogenase subunit 10, SDH10	SK	127	30-46/55-126	70.08%	1		1 × PC 1 × CDL
SDHTB11	Tb927.9.8815	hypothetical protein	SL	86	10-86	89.53%	1		
CIV$_2$									
COX1	P04371	Cytochrome c oxidase subunit 1	C1, c1	549	1-549	100%	12	1 × heme *a* 1 × heme a_3 1 × Cu_B 1 × Mg^{2+} 1 × Na^+	1 × PC 1 × CDL

COX2	P04372	Cytochrome c oxidase subunit 2	C2, c2	210	1-210	100%	2	2 × Cu_A	
COX3	Q35993	Cytochrome c oxidase subunit 3	C3, c3	288	1-288	100%	7		4 × PC 2 × PE
COX4	Q57XX4	Cytochrome c oxidase VII, putative	C4, c4	165	2-165	99.39%	1		2 × PE
COX5B	Q38BB3	Cytochrome-c oxidase	5B, 5b	224	23-224	90.18%	0	1 ×Fe_2S_2	
COX5C	Q38EH2	Uncharacterized protein	5C, 5c	198	1-198	100%	1		1 × PE
COX6A	Q382X7	Uncharacterized protein	6A, 6a	159	54-159	66.67%	1		1 × PC
COX6B	Q38CL0	Cytochrome C oxidase subunit VI, putative	6B, 6b	158	2-157	99.36%	0		
COX7A	Q583E7	Cytochrome c oxidase VIII (COX VIII), putative	7A, 7a	157	29-157	82.17%	1		1 × CDL 1 × PE
COX7C	Q57XS9	Uncharacterized protein	7C, 7c	152	28-151	81.58%	1		1 × CDL 1 × PE
NDUFA4	Q4FKG8	P27 protein	A4, a4	241	1-238	98.76%	1		1 × PC 1 × CDL
COXEG7	Q4GYG7	Cytochrome C oxidase subunit IV	4G, 4g	353	45-353	87.54%	0		2 × PC
COXEG8	Q38FK9	Cytochrome c oxidase subunit V, putative	4H, 4h	196	18-196	91.33%	0		
COXTB1	Q382M2	Cytochrome c oxidase subunit 10, putative	4A, 4a	116	21-116	82.76%	0		
COXTB2	Q386L8	Uncharacterized protein	4B, 4b	121	22-114	76.86%	1		
COXTB3	Q38AY6	Uncharacterized protein	4C, 4c	104	24-104	77.88%	1		1 × PC
COXTB4	Q38AD2	Cytochrome c oxidase subunit IX	4D, 4d	124	13-121	87.90%	1		
CV									
α	Q57TX9	ATP synthase alpha chain, mitochondrial	VA	584	45-151/161-438/446-584	89.73%	0		
	Q57TX9	ATP synthase alpha chain, mitochondrial	VB	584	46-150/162-440/447-584	89.38%	0		
	Q57TX9	ATP synthase alpha chain, mitochondrial	VC	584	45-150/161-584	90.75%	0		
β	Q57XX1	ATP synthase subunit beta	VD	519	27-513	93.83%	0		
	Q57XX1	ATP synthase subunit beta	VE	519	28-507	92.49%	0		
	Q57XX1	ATP synthase subunit beta	VF	519	28-304/314-339/352-513	89.60%	0		

p18	Q57ZP0	Ribonucleoprotein p18, mitochondrial, putative	VJ	188	24-188	87.77%	0		
	Q57ZP0	Ribonucleoprotein p18, mitochondrial, putative	VK	188	23-188	88.30%	0		
	Q57ZP0	Ribonucleoprotein p18, mitochondrial, putative	VN	188	24-188	87.77%	0		
γ	Q38CM0	ATP synthase subunit gamma, mitochondrial	VG	305	2-57/62-301	97.05%	0		
δ/ε	Q586H1	ATP synthase, epsilon chain, putative	VH	182	22-182	88.46%	0		
ε	Q38B96	mitochondrial ATP synthase epsilon chain	VI	75	11-75	86.67%	0		
OSCP/δ	Q38AG1	ATP synthase delta chain, mitochondrial	V1	255	18-203/210-255	90.98%	0		
d	Q57ZW9	mitochondrial ATP synthase subunit d	Vd	370	17-325/333-350	88.38%	0		
b	Q580A0	mitochondrial ATP synthase subunit b	Vp	105	26-105	76.19%	1		1 × PC 1 × CDL
a	P24499	ATP synthase subunit a	Va	231	1-231	100%	0		1 × PC 1 × CDL
c/sub 9	Q57WQ3	ATPase subunit 9, putative	VO	117	40-117	66.67%	2		
	Q57WQ3	ATPase subunit 9, putative	VP	117	40-117	66.67%	2		
	Q57WQ3	ATPase subunit 9, putative	VQ	117	40-117	66.67%	2		
	Q57WQ3	ATPase subunit 9, putative	VR	117	40-117	66.67%	2		
	Q57WQ3	ATPase subunit 9, putative	VS	117	40-117	66.67%	2		
	Q57WQ3	ATPase subunit 9, putative	VT	117	40-117	66.67%	2		
	Q57WQ3	ATPase subunit 9, putative	VU	117	40-117	66.67%	2		
	Q57WQ3	ATPase subunit 9, putative	VV	117	40-117	66.67%	2		
	Q57WQ3	ATPase subunit 9, putative	VW	117	40-117	66.67%	2		
	Q57WQ3	ATPase subunit 9, putative	VX	117	40-117	66.67%	2		
8/A6L	Q585K5	mitochondrial ATP synthase subunit 8	Vc	114	29-114	75.44%	1		
f	Q57ZE2	mitochondrial ATP synthase subunit f	Vf	145	2-136	93.10%	1		1 × CDL
i/j/6.8pl	Q57ZM4	mitochondrial ATP synthase subunit i/j	Vi	104	2-104	99.04%	1		1 × PC
k/DAPIT	Q57VT0	mitochondrial ATP synthase subunit k	Vk	124	20-124	84.68%	1		1 × CDL

e	Q387J1	mitochondrial ATP synthase subunit e	Vl	106	18-64	44.34%	1		1 × CDL
	Q387J1	mitochondrial ATP synthase subunit e	VL	106	18-75	54.72%	1		1 × PC 1 × CDL
g’	Q57TY1	Uncharacterized protein	Vm	139	6-139	96.40%	1		1 × PC
g’’	Q383S5	Uncharacterized protein	VM	122	10-113	85.25%	1		
ATPEG3	Q583U4	mitochondrial ATP synthase subunit ATPEG3	Vq	98	15-98	85.71%	0		1 × CDL
ATPEG4	Tb927.11.2245	mitochondrial ATP synthase subunit ATPEG4	Vr	62	1-62	100%	1		1 × PC
ATPTB1	Q38CI8	mitochondrial ATP synthase subunit ATPTB1	Ve	396	1-383	96.72%	0		4 × CDL
ATPTB3	Q385E4	mitochondrial ATP synthase subunit ATPTB3	Vg	269	2-268	99.26%	0		
ATPTB4	Q389Z3	mitochondrial ATP synthase subunit ATPTB4	Vh	157	21-157	87.26%	0		
ATPTB6	Q387C5	mitochondrial ATP synthase subunit ATPTB6	Vj	169	2-169	99.41%	2		1 × PC 1 × CDL
ATPTB11	Q582T1	mitochondrial ATP synthase subunit ATPTB11	Vn	156	18-156	89.10%	1		
ATPTB12	Q57Z84	mitochondrial ATP synthase subunit ATPTB12	Vo	101	5-100	95.05%	0		

Supplementary Table 4 | Model summary of *T. brucei* supercomplex $CIII_2CIV_2$

Subunit Name	UniProt /Gene ID	Annotation	Chain ID	Total residues	Residues built	% built	TMH	Ligands	Lipids
$CIII_2$									
MPP-alpha	Q386B6	Mitochondrial processing peptidase alpha subunit, putative	QB,Qb	518	20-37/54-154/166-291/297-517	89.96%	0		
MPP-beta	Q57W51	Mitochondrial processing peptidase, beta subunit, putative	QA,Qa	489	2-489	99.80%	0	1 × Cu^{2+}	2 × PC 1 × CDL
COB	Q33573 P00164	Cytochrome b	QC,Qc	368	1-368	100%	8	1 × heme b_L 1 × heme b_H 3 × CoQ_{10}	2 × PC 2 × CDL 1 × PE
CYC1	D6XKS6	Cytochrome c1, heme protein, mitochondrial	QD,Qd	258	4-258	98.84%	1	1 × heme *c*	1 × PE
UQCRFS1	Q38D40	Reiske iron-sulfur protein, mitochondrial	QE,Qe	297	18-297	94.28%	1	1 × Fe_2S_2	2 × PC 1 × PE
UQCRH	Q584K6	Ubiquinol-cytochrome C reductase, putative	QF,Qf	71	5-71	94.37%	0		
UQCRB	Q38BH2	Ubiquinol-cytochrome c reductase complex 14 kDa protein	QG,Qg	201	9-201	0.9602	0		
UQCRQ	Q38BH6	Uncharacterized protein	QH,Qh	120	14-120	89.17%	1		2 × PC
UQCR9	Q582B1	Uncharacterized protein	QI,Qi	73	5-68	87.67%	1		1 × PE
UQCR10	Q381D5	Uncharacterized protein	QJ,Qj	146	2-146	99.32%	1		2 × PC 1 × CDL 1 × PE
UQCREG1	Q57WV3	Uncharacterized protein	QK,Qk	85	10-85	89.41%	1		
UQCRTB1	Tb927.6.5095	hypothetical protein	QL,Ql	72	31-68	52.78%	1		1 × PC
UQCRTB2	*(Poly-UNK)*	-	QM,Qm	-	-	-	0		
CIV_2									

COX1	P04371	Cytochrome c oxidase subunit 1	C1, c1	549	1-549	100%	12	1 × heme *a* 1 × heme a_3 1 × Cu_B 1 × Mg^{2+} 1 × Na^+	1 × PC 1 × CDL
COX2	P04372	Cytochrome c oxidase subunit 2	C2, c2	210	1-210	100%	2	2 × Cu_A	
COX3	Q35993	Cytochrome c oxidase subunit 3	C3, c3	288	1-288	100%	7		4 × PC 2 × PE
COX4	Q57XX4	Cytochrome c oxidase VII, putative	C4, c4	165	2-165	99.39%	1		2 × PE
COX5B	Q38BB3	Cytochrome-c oxidase	5B, 5b	224	23-224	90.18%	0	1 × Fe_2S_2	
COX5C	Q38EH2	Uncharacterized protein	5C, 5c	198	1-198	100%	1		1 × PE
COX6A	Q382X7	Uncharacterized protein	6A, 6a	159	54-159	66.67%	1		1 × PC
COX6B	Q38CL0	Cytochrome C oxidase subunit VI, putative	6B, 6b	158	2-157	99.36%	0		
COX7A	Q583E7	Cytochrome c oxidase VIII (COX VIII), putative	7A, 7a	157	29-157	82.17%	1		1 × CDL 1 × PE
COX7C	Q57XS9	Uncharacterized protein	7C, 7c	152	28-151	81.58%	1		1 × CDL 1 × PE
NDUFA4	Q4FKG8	P27 protein	A4, a4	241	1-238	98.76%	1		1 × PC 1 × CDL
COXEG7	Q4GYG7	Cytochrome c oxidase subunit IV	4G, 4g	353	45-353	87.54%	0		2 × PC
COXEG8	Q38FK9	Cytochrome c oxidase subunit V, putative	4H, 4h	196	18-196	91.33%	0		
COXTB1	Q382M2	Cytochrome c oxidase subunit 10, putative	4A, 4a	116	21-116	82.76%	0		
COXTB2	Q386L8	Uncharacterized protein	4B, 4b	121	22-114	76.86%	1		
COXTB3	Q38AY6	Uncharacterized protein	4C, 4c	104	24-104	77.88%	1		1 × PC
COXTB4	Q38AD2	Cytochrome c oxidase subunit IX	4D, 4d	124	13-121	87.90%	1		

Supplementary Table 5 | Compilation of accession numbers and sequence identifiers for homology detection of OXPHOS complex subunits

	Subunit Name	*Paracoccus denitrificans*	*Homo sapiens*	*Saccharomyces cerevisiae*	*Tetrahymena thermophila*	*Andalucia godoyi*	*Naegleria fowleri*	*Euglena gracilis*	*Diplonema papillatum*	*Perkinsela sp.*	*Bodo saltans*	*Phytomonas sp.* HART1	*Angomonas deanei*	*Leishmania major*	*Trypanosoma brucei*
Complex I	**NDUFV1**	A1B491	P49821		Q23KE4	KAF0853034.1	XP_044565516.1	comp62912_c0_seq. 6	KAJ9456521.1		CUG04023.1	CCW69117	EPY26903.1	XP_001687575.1	XP_844719.1
	NDUFV2	A1B494	P19404		I7MEP0	KAF0852880.1	XP_044558906.1	EG_transcript_19472 sga_contig_466476 sga_contig_302717	KAJ9451711.1		CUI13279.1	CCW69698	EPY34415.1	XP_001682281.1	XP_011775131.1
	NDUFS1	A1B489	P28331		Q23KA9	YP_007890479.1	YP_007890029.1 (complete)	comp61469_c0_seq1_c	KAJ9441941.1 (N-Termini)		CUG91825.1(N-Termini)	CCW69582.1	EPY36509.1	XP_001682557.1	XP_011778675.1
								EG_transcript_7035	APQ44793.1						
	NDUFS2	A1B495	O75306		Q951B1	YP_007890532.1	YP_007890059.1	EG_transcript_13592	QHQ98665.1		MH614645	W6LFE0_9TRYP	AIL54360.1	QNL34152.1	P21301.2
	NDUFS7	A1B497	O75251		Q951B4	YP_007890530.1	XP_044566503.1	EG_transcript_32395	KAJ9454377.1		CUG94143.1	CCW71109.1	EPY15021.1	XP_003392646	XP_011779287.1

	NDUFS8	A1B486	O00217		I7MDW5	YP_007890505.1	YP_007890031.1	comp54309_c0_seq4_c	APQ44789.1		P30826.1		KJ778684.1	ADI75232.1	P30826.1
	NDUFS3	A1B496	O75489		Q950Z4	YP_007890531.1	YP_007890064.1	comp62960_c0_seq11	A0A1L6C400_9EUGL					ADI75234.1	AAA03749.1
	ND1	A1B487	P03886		Q950Y3 NP_149380	YP_007890480.1	YP_007890019.1	sga_contig_684056	A0A1L6C3Y0_9EUGL		O63544_BODSA	CCW72303.1	A0A077EVP0_9TRYP	AAL59664	Q8LU83_TRYCR
	ND2	A1B479	P03891		Q951A3 Q951B2	YP_007890520.1	YP_007890054.1	sga_contig_881214 sga_contig_1967065	A0A1L6C404 (8 TM)		MH614645.1 (complete)	W6LE64_9TRYP (short)_	AIL54356.1 (15TM)	ADI75236 (15TM)	QHI42076.1 (short, incomplete)
	ND3	A1B498	P03897		Q950Z7	YP_007890529.1	YP_007890056.1	sga_contig_1876491(5'3' Frame 2 172-292)	A0A1L6C3Z9_9EUGL					ADK12974.1	Q33578_9TRYP
	ND4	A1B480	P03905		Q950X9	M4QCU1	M4H5J8	sga_contig_171091	A0A6G5ZTZ8		MH614645.1	Q9MD52_9TRYP	A0A077EVQ1_9TRYP	B7TYN8	Q33575_9TRYP
	ND4L	A1B482	P03901		Q950Z5	M4Q9C3	M4H736	EG_transcript_32304	A0A2D2AJX8_9EUGL					[a]	[b]
	ND5	A1B481	P03915		Q950Z0	M4Q9H5	M4H5I5								

					Q951C2			sga_contig_1876491(5'3' Frame 3)	A0A1L6C3Z3		AAC38975.1	AAF26928.1 (partial)	A0A077EVN6_9TRYP	ACJ47215.1	NU5M_TRYBB
	ND6	P29922	P03923		Q950Y2	YP_007890506.1	YP_007890036.1	sga_contig_1876491(5'3' Frame 2 18-171)	A0A6G5ZU20_9EUGL					[c]	[d]
Complex II	**SDHA**	Q59661	P31040	Q00711	8B6G_CA / Q23DI3	KAF0852145	XP_044561902.1	CAAHFI010479403.1	KAJ9463228.1	KNH09743.1	CUI15254.1	CCW71935	EPY29940	XP_003722511	Q57TV5
	SDHB	Q59662	P21912	P21801	8B6G_CB / I7M403	YP_007890524.1	YP_007890028.1	CAAHFI010824066.1	KAJ9444546	KNH04881	CUF34101	CCW67510	EPY40454	XP_001683488.1	Q57YX5
								CAAHFI010774043.1	KAJ9466554	KNH05404.1	CUG90652.1	CCW67790	EPY28105.1	GET87289	Q38EW9
	SDHC	Q59659	Q99643	P33421	8B6G_CC / Q23RH8	YP_007890526.1	XP_044564462.1		KAJ9460132.1	KNH03764.1	CUG92389.1	CCW67851.1	EPY41047.1	XP_001687740.1	Q57WH4
	SDHD	Q59660	O14521	P37298	8B6G_CD / AF396436.1 (mt-genome sequence)	YP_007890525.1	XP_044562692.1		KAJ9473657.1	–	CUG83411.1	CCW65969.1	EPY40432.1	XP_067178424.1	Q57TS4
									KAJ9472158.1	XU18scaffold_249201 to 49398	CUG87138.1	CCW66211.1	EPY20442.1	XP_067175562.1	Q389G4

	SDHTB3								KAJ9473657.1	–	CUG83411.1	CCW65969.1	EPY40432.1	XP_067178424.1	Q586B1
	SDHTB5								KAJ9459767.1	KNH06751.1	CUG06240.1	CCW67409.1	EPY35921.1	XP_001466612.1	Q57XJ6
	SDHTB6								KAJ9450339.1	KNH05595.1	CUG75584.1	CCW71706.1	EPY30801.1	XP_001682130.1	Q57X18
	SDHTB7				I7MEX7				KAJ9470139	KNH08026	CUG06687.1	CCW68013.1	EPY29700.1	XP_001466954	Q584Q7
	SDHTB8								KAJ9472475.1	KNH07853.1	CUE75993.1	CCW70476.1	EPY42109.1	XP_003876787.1	Q586R6
	SDHTB9								KAJ9469225.1	KNH09637.1	CUG87904.1	CCW70504.1	EPY41794.1	XP_003863420	Q38BU1
	SDHTB10								KAJ9461077.1	KNH06224.1	CUE91138.1	CCW69113.1	EPY40002.1	XP_067181342	Q57VW2
	SDHTB11										CUG93869.1	CCW67514.1		XP_067712371.1	Tb927.9.8815
Complex IV	**COX1**	P98002	P00395	P00401	Q950Y4	YP_007890504.1	YP_007890026.1	sga_contig_1208836	APQ44782.1	ALR73783.1	AAC38978.1		AIL54352.1	QNL34160.1	P04371
	COX2	P08306	P00403	P00410	Q950Y9	YP_007890507.1	WND64468.1	gnl|Egra|5053115	ADP88934.1	ALR87302.1	AAC38976.1		AIL54354.1	QNL34158.1	P04372
	COX3	P06030	P00414	P00420	Q950Y6	YP_007890030.1	YP_007890030.1	comp54737_c0_seq2	ADP88935.1	ALR87303.1	MH614645.1 (M)		AIL54359.1	QNL34153.1	Q35993
					Q950Y7			sga_contig_1132792							

	COX4		P13073	P00424		KAF0852574.1	f	comp53543_c0_seq2	e	KNH05038.1	CUF14406.1		EPY39362.1	XP_001683868.1	Q57XX4
	COX5B		P10606	P04037	Q23FF5	KAF0852361.1	XP_044566338.1	comp54722_c0_seq3_cut	KAJ9443665.1	KNH05523.1	CUG91209.1		EPY43418.1	XP_001686618.1	Q38BB3
	COX6C /COX5C		P09669	P07255	Q23DS4			gnl|Egra|Contig1435		KNH05341.1	CUE73799.1		EPY34994.1	XP_888554.1	Q38EH2
	COX6A		P12074	P32799	W7XCY5	KAF0852336.1	XP_044559870.1	EG_transcript_36110	KAJ9457934.1	KNH09236	CUG87617.1		EPY38604.1	XP_001681164.1	Q382X7
	COX6B		P14854	Q01519	Q24I72	KAF0852864.1	XP_044560469.1	comp54364_c0_seq4	KAJ9447346.1	KNH03611.1	CUG08514.1		EPY42157.1	XP_001683136.1	Q38CL0
	NDUFA4		O00483		W7WZP1	KAF0852576.1	g	gnl|Egra|Contig2618		KNH07042.1	CUF11912.1		EPY36836.1	XP_001684379.1	Q4FKG8
	COXEG7							comp55436_c0_seq3_cut	KAJ9472334.1	KNH08374.1	CUG88382.1		EPY26081.1	XP_001681672.1	Q4GYG7
	COXEG8							gi|109781798_cut	KAJ9467144.1	KNH07639.1	CUE67237.1		EPY39767.1	XP_001470514.1	Q38FK9
	COX7C				W7X287			comp55710_c0_seq1_cut		KNH04193.1			EPY38378.1	XP_001687555.1	Q57XS9

	COX7A				I7MGF9	A0A8K0AI33		comp47102_c0_seq2_cut		KNH03637.1	CUF42197.1		EPY39902.1	XP_001685143.1	Q583E7
	COXTB1									KNH03933.1	CUG88046.1		EPY41260.1	XP_001683361.1	Q382M2
	COXTB2									KNH04004.1	CUG86253.1		EPY42577.1	XP_001685967.1	Q386L8
	COXTB3									KNH09279.1	–		EPY39054.1	XP_001686751.1	Q38AY6
	COXTB4									KNH03626.1	CUI15325.1		EPY24356.1	XP_001687296.1	Q38AD2
	COX5A		P20674	P00427											
Complex V	**α**	A1B8N8	P25705	P07251	XP_001008384.2	YP_007890470.1	UAT970600.1	comp27580_c0_seq1	KAJ9467574.1	KNH06957.1	CUG92608.1	CCW61345.1	EPY31520.1	XP_001684527.1	Q57TX9
	β	A1B8P0	P06576	P00830	XP_001032631.2	KAF0852911.1	CAG4714653.1	comp30487_c1_seq1	KAJ9462080.1	KNH08319.1	CUF14326.1	CCW70924.1	EPY14968.1	XP_001683872.1	Q57XX1
	γ	A1B8N9	P36542	P38077	XP_001010761.1	YP_007890471.1	YP_007890034.1	EG_transcript_19235	KAJ9470261.1	KNH06998.1	CUG08615.1	CCW70396.1	EPY40850.1	XP_001683142.1	B0Z0F6
	δ/ε	A1B8P1	P30049	Q12165	XP_001010921.2	KAF0852905.1	XP_044569753.1	comp8147_c0_seq1	KAJ9443837.1	KNH07409.1	CUG91066.1	CCW68203.1	EPY28369.1	XP_001684970.1	Q586H1
	ε		P56381	P21306	XP_001027329.2	KAF0852181.1	XP_044560194.1	comp36626_c0_seq1	KAJ9451454.1	XU18scaffold_1:266201-266374	CYKH01001976	CCW67077.1	EPY38224.1	CAG9583580.1	Q38B96

										[Sequence]					
	p18						XP_044558360.1	comp36594_c0_seq1	KAJ9463001.1	KNH07463.1	CUG92211.1	CCW72037.1	EPY41275.1	XP_001681946.1	Q57ZP0
	e		P56385	NP_010609.1			XP_044561800.1	EG_transcript_33701	KAJ9440524.1		CUF14502.1	CCW70876.1	CAD2217185.1	CAG9575068.1	Q387J1
	g'										CUG89822.1	W6L785	S9WW64	Q4Q180	Q383S5
	g''										CYKH01002228.1, whole genome shotgun equence scaffold	CCW69062.1	CAD2222471.1	XP_001687526.1	Q57TY1
	g		O75964	NP_015345.1	i		XP_044566339.1	comp12813_c0_seq1	KAJ9452804.1	KNH06072, KNH08985	CUG92605.1	CCW69339.1	EPY39046.1	XP_001686043.1	XP_011771764.1
	OSCP/δ	A1B8N7	P48047	P09457	XP_001008856.2	KAF0852331.1	XP_044565181.1	comp36635_c0_seq1	KAJ9447567.1	KNH07340.1	CUG93555.1	CCW70092.1	EPY34471.1	XP_001687269.1	Q38AG1
	c/sub 9	A1B618	P05496	P61829	NP_149381.1	YP_007890500.1	YP_007890063.1	EG_transcript_45706	KAJ9434812.1	KNH01796.1	CUG89672.1	CCW72188.1	EPY34832.1	XP_001683009.1	Q57WQ3

	a	A1B619	P00846	P00854	NP_149365.1	YP_007890509.1	YP_007890055.1	sga_contig_684056 (5'3' Frame 3 1-274)	A0A1L6C3Z2	A0A0U2UX58_9EUGL	MH614645.1	CCW72305.1	AIL54357.1	QNL341551	P24499
	8/A6L		P03928	P00856	Q950Y8	YP_007890466.1	YP_007890038.1	sga_contig_684056 (5'3' Frame 3 275-331)		KNH01792.1	CUG90365.1	CCW67592.1	EPY33006.1	XP_001686184.1	Q585K5
	d		O75947	P30902	XP_001032833.1	A0A8K0F458	XP_044566963.1	comp20520_c0_seq1	EPY32056.1	XU18scaffold_3:42004-42447 [Sequence]	CUE96156.1	CCW68480.1	EPY26816.1	XP_001681139.1	Q57ZW9
	ATPTB1							EG_transcript_7573	KAJ9458980.1	KNH07637.1	CUG75676.1	CCW70376.1	EPY32283.1	XP_001683111.1	Q38CI8
	f		P56134	Q06405	XP_001027673.2	KAF0852856.1		VDSF_6_rev_Run01_Cp357_MD1/G11.esd	KAJ9453328.1		CUE68996.1	CCW70962.1	EPY42335.1	XP_001683919.1	Q57ZE2
	ATPTB3							EG_transcript_14428	KAJ9471222.1	KNH08071.1	CUE94114.1	CCW68363.1	EPY24193.1	XP_001681572.1	Q385E4

	ATPTB4							comp8167_c0_seq1	KAJ9451387.1	KNH07415.1	CUG72673.1	CCW69876.1	CAD2213009.1	XP_001687030.1	Q389Z3
	i/j/6.8pl		P56378	P81450	XP_001032687.2	VRVR01000020.1	A0A6A5BI56	comp12674_c0_seq1	KAJ9447998.1	KNH04879.1	CUF66934.1	CCW68843.1	EPY25220.1	XP_001462824.1	Q57ZM4
	ATPTB6							EG_transcript_28774	KAJ9458588.1	KNH01797.1	CUG94128.1	CCW71114.1	EPY35394.1	XP_003721871.1	Q387C5
	k/DAPIT		Q96IX5	P81451	XP_001031468.1	[h]		EG_transcript_55785		KNH09601.1	CUG93082.1	CCW70160.1	EPY38730.1	XP_001684114.1	Q57VT0
	ATPTB11								KAJ9462348.1	KNH07606.1	CUG91955.1	CCW71003.1	EPY32809.1	XP_001683968.1	Q582T1
	ATPTB12							GDJR01005257.1	KAJ9459969.1	KNH04797.1	CUE97976.1	CCW68466.1	EPY29077.1	XP_001681153.1	Q57Z84
	b	5DN6_V, W	P24539	P05626	XP_001016306.2	YP_007890467.1	YP_007890035.1	comp8208_c0_seq1	KAJ9471685.1	KNH08057.1	CUI15588.1	CCW67167.1	EPY37786.1	XP_001686508.1	Q580A0
	F6/h		NP_001003696.1	Q12349		KAF0852839.1									
	ATPEG3							GDJR01012366.1	KAJ9464142.1	KNH08670.1	CUG86310.1	CCW66351.1	EPY41344.1	XP_001683315.1	Q583U4
	ATPEG4							GEFR01049309.1				CCW71041.1			Tb927.11.2245

[a-d] For *Trypanosoma brucei* and *Leishmania tarentolae*, transcripts CR3 (Q33565 and Q7M3S7) and CR4 (Q33564 and D9MNC5) are not included here based on the analyses in the Main Text.

[e-h] *Diplonema papillatum* subunit COX4 (KAJ9445835.1), *Naegleria fowleri* subunits COX4 (XP_044557135.1) and NDUFA4 (XP_044556366) and *Andalucia godoyi* subunit *k* (ANDGO_05913.mRNA.1) are not included here since we cannot confirm their sequence homology with known subunit sequences.

[i] *Tetrahymena thermophila* subunit *g* (XP_001032300.2) is not included here due to lack of structural homology with known subunit *g* structures.

Supplementary Table 6 | The protocol for equilibration of protein-lipid-solvent system

Step	Time	Restraints						
		Protein	Lipids					Redox cofactors
	[ns]		CIV_2-aligned mem-brane patch	CV_2-aligned mem-brane patch	Third Mem-brane patch	Structural	Modelled	
NVT	0.1	Heavy atoms	Tail atoms[a]	Tail atoms	Tail atoms	Tail atoms	Tail atoms	All
NPT1	1	Heavy atoms	None	Tail atoms	Tail atoms	Tail atoms	Tail atoms	All
NPT2	10	Heavy atoms	None	Tail atoms	None	Tail atoms	None	All
NPT3	10	Backbone	None	None	None	None	None	None
NPT4	10	None	None	None	None	None	None	None

[a] The last carbon atoms of the lipid tails.

Supplementary Table 7 | The oligonucleotides used for knockout strain generation

Primers for sgRNA generation	
Universal reverse primer for sgRNA amplification (G00)	AAAAGCACCGACTCGGTGCCACTTTTTCAAGTTGATAACGGACTAGCCTTATTTTAACTTGCTATTTCTAGCTCTAAAAC
Forward primer for 5' sgRNA for *g''* KO	gaaattaatacgactcactataggTGGCCCAACCTTCCTTTCTTgttttagagctagaaatagc
Forward primer for 3' sgRNA for *g''* KO	gaaattaatacgactcactataggCAACACCTACGCACTTGACTgttttagagctagaaatagc
Forward primer for 5' sgRNA for *g'* KO	gaaattaatacgactcactataggGATGTCGCGAGTGCGGTAAGgttttagagctagaaatagc
Forward primer for 3' sgRNA for *g'* KO	gaaattaatacgactcactataggATGCGTGTTCCCGTAATGTTgttttagagctagaaatagc
Forward primer for 5' sgRNA for NDUFA4 KO	gaaattaatacgactcactataggATTTATATCATATTCAGGTAgttttagagctagaaatagc
Forward primer for 3' sgRNA for NDUFA4 KO	gaaattaatacgactcactataggGGTTACTACAGTAAGCGATGgttttagagctagaaatagc
Forward primer for 5' sgRNA for COXTB2 KO	gaaattaatacgactcactataggCAAAAAAAAAAACAATAACAgttttagagctagaaatagc
Forward primer for 3' sgRNA for COXTB2 KO	gaaattaatacgactcactataggAGTTAGGCATGGAATAGGGTgttttagagctagaaatagc
Forward primer for 5' sgRNA for COXTB3 KO	gaaattaatacgactcactataggATATAGTGAAGTAATCGAATgttttagagctagaaatagc
Forward primer for 3' sgRNA for COXTB3 KO	gaaattaatacgactcactataggTGTTGCGTATTCCACAGCGAgttttagagctagaaatagc
Primers for repair template generation	
Forward primer for Hygromycin repair template (pPOTv5) for *g''* KO	ATATATATATATATATTTCACTTAATTCATAGGCTAGGGCACAGCAAGGT
Reverse primer for Hygromycin repair template (pPOTv5) for *g''* KO	CGTTCACTTGGCAACGCCCGCCCGCTCCCAGGGGCTCGAATCCCCCCATT
Forward primer for Hygromycin repair template (pPOTv5) for *g'* KO	ATAATGTCACGAAAAGCTCTTACAAGACCAAGGCTAGGGCACAGCAAGGT
Reverse primer for Hygromycin repair template (pPOTv5) for *g'* KO	CAGGGCAGCAGTCACCACAAACGCTAAGAAGGGGCTCGAATCCCCCCATT
Forward primer for Hygromycin repair template (pPOTv5) for NDUFA4 KO	TGTTTTTTTTTTGTGCTCAACGATGTATCCAAGGCTAGGGCACAGCAAGGT
Reverse primer for Hygromycin repair template (pPOTv5) for NDUFA4 KO	ACAGTGACAATAGTAATGAGCGATGGCGAAGGGGCTCGAATCCCCCCATT
Forward primer for Hygromycin repair template (pPOTv5) for COXTB2 KO	TTACTAACAGTGTACAGACATCAGCTTCATAGGCTAGGGCACAGCAAGGT
Reverse primer for Hygromycin repair template (pPOTv5) for COXTB2 KO	CTCCACATGTACAGTTCGAGCGAGCTTCCCGGGGCTCGAATCCCCCCATT
Forward primer for Hygromycin repair template (pPOTv5) for COXTB3 KO	ATATATACATTATATATATACATTATATATAGGCTAGGGCACAGCAAGGT
Reverse primer for Hygromycin repair template (pPOTv5) for COXTB3 KO	CAAAGGAGACTAAAATGCGTACCTGTGCCTGGGGCTCGAATCCCCCCATT
Forward primer for Neomycin repair template (pHD2164) for *g''* KO	ATATATATATATATATTTCACTTAATTCATGCACAGCAAGGTCTTCTGAAATTC
Reverse primer for Neomycin repair template (pHD2164) for *g''* KO	CGTTCACTTGGCAACGCCCGCCCGCTCCCAATCCCCCCATTTTCTTCTTTTACA
Forward primer for Neomycin repair template (pHD2164) for *g'* KO	ATAATGTCACGAAAAGCTCTTACAAGACCAGCACAGCAAGGTCTTCTGAAATTC

Reverse primer for Neomycin repair template (pHD2164) for *g'* KO	CAGGGCAGCAGTCACCACAAACGCTAAGAAATCCCCCCATTTTCTTCTTTTACA
Forward primer for Neomycin repair template (pHD2164) for NDUFA4 KO	TGTTTTTTTTTGTGCTCAACGATGTATCCAGCACAGCAAGGTCTTCTGAAATTC
Reverse primer for Neomycin repair template (pHD2164) for NDUFA4 KO	ACAGTGACAATAGTAATGAGCGATGGCGAAATCCCCCCATTTTCTTCTTTTACA
Forward primer for Neomycin repair template (pHD2164) for COXTB2 KO	TTACTAACAGTGTACAGACATCAGCTTCATGCACAGCAAGGTCTTCTGAAATTC
Reverse primer for Neomycin repair template (pHD2164) for COXTB2 KO	CTCCACATGTACAGTTCGAGCGAGCTTCCCATCCCCCCATTTTCTTCTTTTACA
Forward primer for Neomycin repair template (pHD2164) for COXTB3 KO	ATATATACATTATATATATACATTATATATGCACAGCAAGGTCTTCTGAAATTC
Reverse primer for Neomycin repair template (pHD2164) for COXTB3 KO	CAAAGGAGACTAAAATGCGTACCTGTGCCTATCCCCCCATTTTCTTCTTTTACA
Primers for GOI:pLEW79 construct generation	
Forward primer for cloning COXTB2 into pLEW79 (with HindIII site)	CTAAGCTTATGCTCCGCCGTTG
Reverse primer for cloning COXTB2 into pLEW79 (with BamHI site)	ATGGATCCCTAAGCGAGGTCGGTATC
Forward primer for cloning COXTB3 into pLEW79 (with HindIII site)	CTAAGCTTATGCTCCGACGCGT
Reverse primer for cloning COXTB3 into pLEW79 (with BamHI site)	ATGGATCCTTACACTGCCCTGTCAG
Primers for diagnostic PCR	
Forward primer (A) on *g''* CDS for diagnostic PCR	CGAGTAGCTTAACCTCTGAC
Reverse primer (B) on *g''* UTR for diagnostic PCR	CTCCAAAACAACCAAAGCACA
Forward primer (A) on *g'* CDS for diagnostic PCR	AAGCGTCATGTTGAAGAGC
Reverse primer (B) on *g'* UTR for diagnostic PCR	AACTTTTACCCCCACCACA
Forward primer (A) on NDUFA4 CDS for diagnostic PCR	CTTCCTACACCCGGATATTAC
Reverse primer (B) on NDUFA4 UTR for diagnostic PCR	GCATGTTAGTGAATGAAGAAGAG
Forward primer (A) on COXTB2 CDS for diagnostic PCR	CTAATCCTGGTGAAACGGG
Reverse primer (B) on COXTB2 UTR for diagnostic PCR	CCTTGCATCTCATGTCACC
Forward primer (A) on COXTB3 CDS for diagnostic PCR	GACGGTATACAAACTACGACC
Reverse primer (B) on COXTB3 UTR for diagnostic PCR	TAACAAAGGAGACTAAAATGCGT
Forward primer (C) for Hygromycin CDS for diagnostic PCR	GAGGGCGAAGAATCTCGTGCT
Forward primer (D) for Neomycin CDS for diagnostic PCR	CTTGCCGAATATCATGGTGG

Supplementary Videos

Supplementary Video 1 Cryo-EM maps and models of CIICIV$_2$CV morphing through the three rotational states and CIII$_2$CIV$_2$.

Supplementary Video 2 MD simulation of WT CIICIV$_2$CV supercomplex shows that the membrane curvature is sustained. Complex IV dimer is colored in blue and purple, Complex II in red, Complex V stator in green and Complex V rotor in beige. The lipid bilayer phosphorus atoms are shown as orange spheres.

Supplementary Video 3 MD simulation of CIICIV$_2$ subcomplex shows the loss of membrane curvature (see also Supplementary Video 2).

Supplementary Video 4 MD simulation of pure (protein-free) lipid bilayer does not show any noticeable membrane curvature (see also Supplementary Video 2).

Supplementary Video 5 MD simulation of WT supercomplex CIICIV$_2$CV. The *g'/g''* subunits are highlighted in dark red and show overall conformational stability (see also Supplementary Video 2).

Supplementary Video 6 MD simulation of supercomplex CIICIV$_2$CV without subunit g'. KO simulation shows that helix 3 of *g''*, here highlighted in dark blue, shows significant distortion along the simulation (see also Supplementary Video 5).

Supplementary Video 7 MD simulation of supercomplex CIICIV$_2$CV without subunit *g''*. KO simulation shows that helix 1 and 3 of *g'*, here colored in dark green, undergo distortion from the original arrangement (see also Supplementary Video 5).

Supplementary Video 8 3D reconstruction of electron tomogram corresponding to WT mitochondria in Fig. 3d. Selected tilt sections shown in Extended Data Fig. 9d.

Supplementary Video 9 3D reconstruction of electron tomogram corresponding to *g'*$^{-/-}$ mitochondria in Fig. 3e. Selected tilt sections shown in Extended Data Fig. 9e.

Supplementary References

1. Niemann, M. & Schneider, A. A Scalable Purification Method for Mitochondria from Trypanosoma brucei. *Methods in molecular biology (Clifton, N.J.)* **2116**, 611–626 (2020).
2. Schneider, A., Charrière, F., Pusnik, M. & Horn, E. K. Isolation of mitochondria from procyclic Trypanosoma brucei. *Methods in molecular biology (Clifton, N.J.)* **372**, 67–80 (2007).
3. Gahura, O., Mühleip, A., Hierro-Yap, C., Panicucci, B., Jain, M., Hollaus, D., Slapničková, M., Zíková, A. & Amunts, A. An ancestral interaction module promotes oligomerization in divergent mitochondrial ATP synthases. *Nature communications* **13**, 5989 (2022).
4. Zhou, L., Maldonado, M., Padavannil, A., Guo, F. & Letts, J. A. Structures of Tetrahymena's respiratory chain reveal the diversity of eukaryotic core metabolism. *Science (New York, N.Y.)* **376**, 831–839 (2022).
5. Han, F., Hu, Y., Wu, M., He, Z., Tian, H. & Zhou, L. Structures of Tetrahymena thermophila respiratory megacomplexes on the tubular mitochondrial cristae. *Nature communications* **14**, 2542 (2023).
6. He, Z., Wu, M., Tian, H., Wang, L., Hu, Y., Han, F., Zhou, J., Wang, Y. & Zhou, L. Euglena's atypical respiratory chain adapts to the discoidal cristae and flexible metabolism. *Nature communications* **15**, 1628 (2024).
7. Gahura, O., Šubrtová, K., Váchová, H., Panicucci, B., Fearnley, I. M., Harbour, M. E., Walker, J. E. & Zíková, A. The F1 -ATPase from Trypanosoma brucei is elaborated by three copies of an additional p18-subunit. *The FEBS journal* **285**, 614–628 (2018).
8. Punjani, A., Rubinstein, J. L., Fleet, D. J. & Brubaker, M. A. cryoSPARC: algorithms for rapid unsupervised cryo-EM structure determination. *Nature methods* **14**, 290–296 (2017).
9. Punjani, A., Zhang, H. & Fleet, D. J. Non-uniform refinement: adaptive regularization improves single-particle cryo-EM reconstruction. *Nature methods* **17**, 1214–1221 (2020).

10. Zivanov, J., Nakane, T. & Scheres, S. H. W. Estimation of high-order aberrations and anisotropic magnification from cryo-EM data sets in RELION-3.1. *IUCrJ* **7**, 253–267 (2020).

11. Liebschner, D. *et al.* Macromolecular structure determination using X-rays, neutrons and electrons: recent developments in Phenix. *Acta crystallographica. Section D, Structural biology* **75**, 861–877 (2019).

12. Kimanius, D., Dong, L., Sharov, G., Nakane, T. & Scheres, S. H. W. New tools for automated cryo-EM single-particle analysis in RELION-4.0. *The Biochemical journal* **478**, 4169–4185 (2021).

13. Emsley, P., Lohkamp, B., Scott, W. G. & Cowtan, K. Features and development of Coot. *Acta crystallographica. Section D, Biological crystallography* **66**, 486–501 (2010).

14. Pettersen, E. F., Goddard, T. D., Huang, C. C., Meng, E. C., Couch, G. S., Croll, T. I., Morris, J. H. & Ferrin, T. E. UCSF ChimeraX: Structure visualization for researchers, educators, and developers. *Protein science : a publication of the Protein Society* **30**, 70–82 (2021).

15. Goddard, T. D., Huang, C. C., Meng, E. C., Pettersen, E. F., Couch, G. S., Morris, J. H. & Ferrin, T. E. UCSF ChimeraX: Meeting modern challenges in visualization and analysis. *Protein science : a publication of the Protein Society* **27**, 14–25 (2018).

16. Meng, E. C., Goddard, T. D., Pettersen, E. F., Couch, G. S., Pearson, Z. J., Morris, J. H. & Ferrin, T. E. UCSF ChimeraX: Tools for structure building and analysis. *Protein science : a publication of the Protein Society* **32**, e4792 (2023).

17. Sun, F., Huo, X., Zhai, Y., Wang, A., Xu, J., Su, D., Bartlam, M. & Rao, Z. Crystal structure of mitochondrial respiratory membrane protein complex II. *Cell* **121**, 1043–57 (2005).

18. Mühleip, A., Flygaard, R. K., Baradaran, R., Haapanen, O., Gruhl, T., Tobiasson, V., Maréchal, A., Sharma, V. & Amunts, A. Structural basis of mitochondrial membrane bending by the I-II-III2-IV2 supercomplex. *Nature* **615**, 934–938 (2023).

19. Ho, C.-M., Li, X., Lai, M., Terwilliger, T. C., Beck, J. R., Wohlschlegel, J., Goldberg, D. E., Fitzpatrick, A. W. P. & Zhou, Z. H. Bottom-up structural proteomics: cryoEM of protein complexes enriched from the cellular milieu. *Nature methods* **17**, 79–85 (2020).

20. Hall, N. *et al.* The DNA sequence of chromosome I of an African trypanosome: gene content, chromosome organisation, recombination and polymorphism. *Nucleic acids research* **31**, 4864–73 (2003).

21. Berriman, M. *et al.* The genome of the African trypanosome Trypanosoma brucei. *Science (New York, N.Y.)* **309**, 416–22 (2005).

22. Shanmugasundram, A., Starns, D., Böhme, U., Amos, B., Wilkinson, P. A., Harb, O. S., Warrenfeltz, S., Kissinger, J. C., McDowell, M. A., Roos, D. S., Crouch, K. & Jones, A. R. TriTrypDB: An integrated functional genomics resource for kinetoplastida. *PLoS neglected tropical diseases* **17**, e0011058 (2023).

23. Aslett, M. *et al.* TriTrypDB: a functional genomic resource for the Trypanosomatidae. *Nucleic acids research* **38**, D457-62 (2010).

24. Afonine, P. V., Grosse-Kunstleve, R. W., Echols, N., Headd, J. J., Moriarty, N. W., Mustyakimov, M., Terwilliger, T. C., Urzhumtsev, A., Zwart, P. H. & Adams, P. D. Towards automated crystallographic structure refinement with phenix.refine. *Acta crystallographica. Section D, Biological crystallography* **68**, 352–67 (2012).

25. Afonine, P. V., Poon, B. K., Read, R. J., Sobolev, O. V., Terwilliger, T. C., Urzhumtsev, A. & Adams, P. D. Real-space refinement in PHENIX for cryo-EM and crystallography. *Acta crystallographica. Section D, Structural biology* **74**, 531–544 (2018).

26. Abramson, J. *et al.* Accurate structure prediction of biomolecular interactions with AlphaFold 3. *Nature* **630**, 493–500 (2024).

27. Williams, C. J., Headd, J. J., Moriarty, N. W., Prisant, M. G., Videau, L. L., Deis, L. N., Verma, V., Keedy, D. A., Hintze, B. J., Chen, V. B., Jain, S., Lewis, S. M., Arendall, W. B., Snoeyink, J., Adams, P. D., Lovell, S. C., Richardson, J. S. & Richardson, D. C. MolProbity: More and better reference data for improved all-atom structure validation. *Protein science : a publication of the Protein Society* **27**, 293–315 (2018).

28. Altschul, S. F., Madden, T. L., Schäffer, A. A., Zhang, J., Zhang, Z., Miller, W. & Lipman, D. J. Gapped BLAST and PSI-BLAST: a new generation of protein database search programs. *Nucleic acids research* **25**, 3389–402 (1997).

29. Zimmermann, L., Stephens, A., Nam, S.-Z., Rau, D., Kübler, J., Lozajic, M., Gabler, F., Söding, J., Lupas, A. N. & Alva, V. A Completely Reimplemented MPI Bioinformatics Toolkit with a New HHpred Server at its Core. *Journal of molecular biology* **430**, 2237–2243 (2018).

30. Sinha, S. D. & Wideman, J. G. The persistent homology of mitochondrial ATP synthases. *iScience* **26**, 106700 (2023).

31. Flygaard, R. K., Mühleip, A., Tobiasson, V. & Amunts, A. Type III ATP synthase is a symmetry-deviated dimer that induces membrane curvature through tetramerization. *Nature communications* **11**, 5342 (2020).

32. Ronquist, F., Teslenko, M., van der Mark, P., Ayres, D. L., Darling, A., Höhna, S., Larget, B., Liu, L., Suchard, M. A. & Huelsenbeck, J. P. MrBayes 3.2: efficient Bayesian phylogenetic inference and model choice across a large model space. *Systematic biology* **61**, 539–42 (2012).

33. Larkin, M. A., Blackshields, G., Brown, N. P., Chenna, R., McGettigan, P. A., McWilliam, H., Valentin, F., Wallace, I. M., Wilm, A., Lopez, R., Thompson, J. D., Gibson, T. J. & Higgins, D. G. Clustal W and Clustal X version 2.0. *Bioinformatics (Oxford, England)* **23**, 2947–8 (2007).

34. Letunic, I. & Bork, P. Interactive Tree Of Life (iTOL): an online tool for phylogenetic tree display and annotation. *Bioinformatics (Oxford, England)* **23**, 127–8 (2007).

35. Letunic, I. & Bork, P. Interactive Tree Of Life (iTOL) v5: an online tool for phylogenetic tree display and annotation. *Nucleic acids research* **49**, W293–W296 (2021).

36. Letunic, I. & Bork, P. Interactive Tree of Life (iTOL) v6: recent updates to the phylogenetic tree display and annotation tool. *Nucleic acids research* **52**, W78–W82 (2024).

37. Sali, A. & Blundell, T. L. Comparative protein modelling by satisfaction of spatial restraints. *Journal of molecular biology* **234**, 779–815 (1993).

38. Søndergaard, C. R., Olsson, M. H. M., Rostkowski, M. & Jensen, J. H. Improved Treatment of Ligands and Coupling Effects in Empirical Calculation and Rationalization of pKa Values. *Journal of chemical theory and computation* **7**, 2284–95 (2011).

39. Chang, C. H. & Kim, K. Density Functional Theory Calculation of Bonding and Charge Parameters for Molecular Dynamics Studies on [FeFe] Hydrogenases. *Journal of chemical theory and computation* **5**, 1137–45 (2009).

40. Johansson, M. P., Kaila, V. R. I. & Laakkonen, L. Charge parameterization of the metal centers in cytochrome c oxidase. *Journal of computational chemistry* **29**, 753–67 (2008).

41. Jo, S., Kim, T., Iyer, V. G. & Im, W. CHARMM-GUI: a web-based graphical user interface for CHARMM. *Journal of computational chemistry* **29**, 1859–65 (2008).

42. Smith, D. M. A., Xiong, Y., Straatsma, T. P., Rosso, K. M. & Squier, T. C. Force-Field Development and Molecular Dynamics of [NiFe] Hydrogenase. *Journal of chemical theory and computation* **8**, 2103–14 (2012).

43. Teixeira, V. H., Baptista, A. M. & Soares, C. M. Pathways of H2 toward the active site of [NiFe]-hydrogenase. *Biophysical journal* **91**, 2035–45 (2006).

44. Huang, J. & MacKerell, A. D. CHARMM36 all-atom additive protein force field: validation based on comparison to NMR data. *Journal of computational chemistry* **34**, 2135–45 (2013).

45. Lomize, M. A., Pogozheva, I. D., Joo, H., Mosberg, H. I. & Lomize, A. L. OPM database and PPM web server: Resources for positioning of proteins in membranes. *Nucleic Acids Research* **40**, 370–376 (2012).

46. Tsukihara, T., Shimokata, K., Katayama, Y., Shimada, H., Muramoto, K., Aoyama, H., Mochizuki, M., Shinzawa-Itoh, K., Yamashita, E., Yao, M., Ishimura, Y. & Yoshikawa, S. The low-spin heme of cytochrome c oxidase as the driving element of the proton-pumping process. *Proceedings of the National Academy of Sciences of the United States of America* **100**, 15304–9 (2003).

47. Guo, H., Bueler, S. A. & Rubinstein, J. L. Atomic model for the dimeric FO region of mitochondrial ATP synthase. *Science* **358**, 936–940 (2017).

48. Bussi, G., Donadio, D. & Parrinello, M. Canonical sampling through velocity rescaling. *The Journal of chemical physics* **126**, 014101 (2007).

49. Berendsen, H. J. C., Postma, J. P. M., van Gunsteren, W. F., DiNola, A. & Haak, J. R. Molecular dynamics with coupling to an external bath. *The Journal of Chemical Physics* **81**, 3684–3690 (1984).

50. Evans, D. J. & Holian, B. L. The Nose–Hoover thermostat. *The Journal of Chemical Physics* **83**, 4069–4074 (1985).

51. Parrinello, M. & Rahman, A. Polymorphic transitions in single crystals: A new molecular dynamics method. *Journal of Applied Physics* **52**, 7182–7190 (1981).

52. Darden, T., York, D. & Pedersen, L. Particle mesh Ewald: An N ·log(N) method for Ewald sums in large systems. *The Journal of Chemical Physics* **98**, 10089–10092 (1993).

53. Hess, B., Bekker, H., Berendsen, H. J. C. & Fraaije, J. G. E. M. LINCS: A linear constraint solver for molecular simulations. *Journal of Computational Chemistry* **18**, 1463–1472 (1997).

54. Abraham, M. J., Murtola, T., Schulz, R., Páll, S., Smith, J. C., Hess, B. & Lindahl, E. GROMACS: High performance molecular simulations through multi-level parallelism from laptops to supercomputers. *SoftwareX* **1**–**2**, 19–25 (2015).

55. Humphrey, W., Dalke, A. & Schulten, K. VMD: visual molecular dynamics. *Journal of molecular graphics* **14**, 33–8, 27–8 (1996).

56. Michaud-Agrawal, N., Denning, E. J., Woolf, T. B. & Beckstein, O. MDAnalysis: a toolkit for the analysis of molecular dynamics simulations. *Journal of computational chemistry* **32**, 2319–27 (2011).

57. Gowers, R., Linke, M., Barnoud, J., Reddy, T., Melo, M., Seyler, S., Domański, J., Dotson, D., Buchoux, S., Kenney, I. & Beckstein, O. MDAnalysis: A Python Package for the Rapid Analysis of Molecular Dynamics Simulations. in *Proceedings of the 15th Python in Science Conference* 98–105 (2016). doi:10.25080/Majora-629e541a-00e.

58. Dahl, A. C. E., Chavent, M. & Sansom, M. S. P. Bendix: intuitive helix geometry analysis and abstraction. *Bioinformatics (Oxford, England)* **28**, 2193–4 (2012).

59. Eisenhaber, F., Lijnzaad, P., Argos, P., Sander, C. & Scharf, M. The double cubic lattice method: Efficient approaches to numerical integration of surface area and volume and to dot surface contouring of molecular assemblies. *Journal of Computational Chemistry* **16**, 273–284 (1995).

60. Tomar, S. Converting video formats with FFmpeg. *Linux Journal* **2006**, (2006).

61. Alves, A. A., Gabriel, H. B., Bezerra, M. J. R., de Souza, W., Vaughan, S., Cunha-E-Silva, N. L. & Sunter, J. D. Control of assembly of extra-axonemal structures: the paraflagellar rod of trypanosomes. *Journal of cell science* **133**, (2020).

62. Beneke, T. & Gluenz, E. LeishGEdit: A Method for Rapid Gene Knockout and Tagging Using CRISPR-Cas9. *Methods in molecular biology (Clifton, N.J.)* **1971**, 189–210 (2019).

63. Schneider, A., Bouzaidi-Tiali, N., Chanez, A.-L. & Bulliard, L. ATP production in isolated mitochondria of procyclic Trypanosoma brucei. *Methods in molecular biology (Clifton, N.J.)* **372**, 379–87 (2007).

64. Doleželová, E., Kunzová, M., Dejung, M., Levin, M., Panicucci, B., Regnault, C., Janzen, C. J., Barrett, M. P., Butter, F. & Zíková, A. Cell-based and multi-omics profiling reveals dynamic metabolic repurposing of mitochondria to drive developmental progression of Trypanosoma brucei. *PLoS biology* **18**, e3000741 (2020).

65. Knott, G., Rosset, S. & Cantoni, M. Focussed ion beam milling and scanning electron microscopy of brain tissue. *Journal of visualized experiments : JoVE* e2588 (2011) doi:10.3791/2588.

66. Kaurov, I., Vancová, M., Schimanski, B., Cadena, L. R., Heller, J., Bílý, T., Potěšil, D., Eichenberger, C., Bruce, H., Oeljeklaus, S., Warscheid, B., Zdráhal, Z., Schneider, A., Lukeš, J. & Hashimi, H. The Diverged Trypanosome MICOS Complex as a Hub for Mitochondrial Cristae Shaping and Protein Import. *Current biology : CB* **28**, 3393-3407.e5 (2018).

67. Mastronarde, D. N. Automated electron microscope tomography using robust prediction of specimen movements. *Journal of structural biology* **152**, 36–51 (2005).

68. Mastronarde, D. N. & Held, S. R. Automated tilt series alignment and tomographic reconstruction in IMOD. *Journal of structural biology* **197**, 102–113 (2017).

69. Schindelin, J., Arganda-Carreras, I., Frise, E., Kaynig, V., Longair, M., Pietzsch, T., Preibisch, S., Rueden, C., Saalfeld, S., Schmid, B., Tinevez, J.-Y., White, D. J., Hartenstein, V., Eliceiri, K., Tomancak, P. & Cardona, A. Fiji: an open-source platform for biological-image analysis. *Nature methods* **9**, 676–82 (2012).

70. Flegontov, P., Gray, M. W., Burger, G. & Lukeš, J. Gene fragmentation: a key to mitochondrial genome evolution in Euglenozoa? *Current genetics* **57**, 225–32 (2011).

71. Feagin, J. E., Abraham, J. M. & Stuart, K. Extensive editing of the cytochrome c oxidase III transcript in Trypanosoma brucei. *Cell* **53**, 413–22 (1988).

72. Bhat, G. J., Koslowsky, D. J., Feagin, J. E., Smiley, B. L. & Stuart, K. An extensively edited mitochondrial transcript in kinetoplastids encodes a protein homologous to ATPase subunit 6. *Cell* **61**, 885–94 (1990).

73. Wong, J. E., Zíková, A. & Gahura, O. The Ancestral Shape of the Access Proton Path of Mitochondrial ATP Synthases Revealed by a Split Subunit-a. *Molecular biology and evolution* **40**, 1–9 (2023).

74. Benne, R., Van den Burg, J., Brakenhoff, J. P. J., Sloof, P., Van Boom, J. H. & Tromp, M. C. Major transcript of the frameshifted coxII gene from trypanosome mitochondria contains four nucleotides that are not encoded in the DNA. *Cell* **46**, 819–26 (1986).

75. Feagin, J. E., Shaw, J. M., Simpson, L. & Stuart, K. Creation of AUG initiation codons by addition of uridines within cytochrome b transcripts of kinetoplastids. *Proceedings of the National Academy of Sciences of the United States of America* **85**, 539–43 (1988).

76. Feagin, J. E., Jasmer, D. P. & Stuart, K. Developmentally regulated addition of nucleotides within apocytochrome b transcripts in Trypanosoma brucei. *Cell* **49**, 337–45 (1987).

77. Dobáková, E., Flegontov, P., Skalický, T. & Lukeš, J. Unexpectedly Streamlined Mitochondrial Genome of the Euglenozoan Euglena gracilis. *Genome biology and evolution* **7**, 3358–67 (2015).

78. Huynen, M. A., Duarte, I. & Szklarczyk, R. Loss, replacement and gain of proteins at the origin of the mitochondria. *Biochimica et biophysica acta* **1827**, 224–31 (2013).

79. Du, Z. *et al.* Structure of the human respiratory complex II. *Proceedings of the National Academy of Sciences of the United States of America* **120**, e2216713120 (2023).

80. Wú, F., Mühleip, A., Gruhl, T., Sheiner, L., Maréchal, A. & Amunts, A. Structure of the II2-III2-IV2 mitochondrial supercomplex from the parasite Perkinsus marinus. at https://doi.org/10.1101/2024.05.25.595893 (2024).

81. Haapanen, O., Djurabekova, A. & Sharma, V. Role of Second Quinone Binding Site in Proton Pumping by Respiratory Complex I. *Frontiers in chemistry* **7**, 221 (2019).